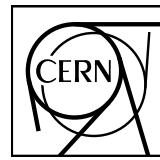


EUROPEAN ORGANIZATION FOR NUCLEAR RESEARCH



ALICE

CERN-EP-2020-059
15 April 2020

Production of light-flavor hadrons in pp collisions at $\sqrt{s} = 7$ and $\sqrt{s} = 13$ TeV

ALICE Collaboration*

Abstract

The production of π^\pm , K^\pm , K_S^0 , $K^*(892)^0$, p , \bar{p} , $\phi(1020)$, Λ , $\bar{\Lambda}$, Ξ^- , Ξ^+ , Ω^- , and $\bar{\Omega}^+$ was measured in inelastic proton–proton (pp) collisions at a center-of-mass energy of $\sqrt{s} = 13$ TeV at midrapidity ($|y| < 0.5$) as a function of transverse momentum (p_T) using the ALICE detector at the CERN LHC. Furthermore, the single-particle p_T distributions of K_S^0 , Λ , and $\bar{\Lambda}$ in inelastic pp collisions at $\sqrt{s} = 7$ TeV are reported here for the first time. The p_T distributions are studied at midrapidity within the transverse momentum range $0 \leq p_T \leq 20$ GeV/ c , depending on the particle species. The p_T spectra, integrated yields, and particle yield ratios are discussed as a function of collision energy and compared with measurements at lower \sqrt{s} and with results from various general-purpose QCD-inspired Monte Carlo models. A hardening of the spectra at high p_T with increasing collision energy is observed, which is similar for all particle species under study. The measured p_T spectra of mesons for $p_T < 2$ GeV/ c significantly deviate from the empirical transverse mass scaling relation based on the measured charged pion spectrum. The empirical $x_T \equiv 2p_T/\sqrt{s}$ scaling for π^\pm , K^\pm , K^{*0} and $p(\bar{p})$ is well satisfied in the hard scattering region of particle production. As the collision energy increases from $\sqrt{s} = 7$ TeV to 13 TeV, the yields of non- and single-strange hadrons normalized to the pion yields remain approximately constant as a function of \sqrt{s} , while ratios for multi-strange hadrons indicate enhancements. The p_T -differential cross sections of π^\pm , K^\pm , and $p(\bar{p})$ are compared with next-to-leading order perturbative QCD calculations, which are found to overestimate the cross sections for π^\pm and $p(\bar{p})$ at high p_T .

© 2020 CERN for the benefit of the ALICE Collaboration.

Reproduction of this article or parts of it is allowed as specified in the CC-BY-4.0 license.

*See Appendix A for the list of collaboration members

1 Introduction

Identified particle spectra and yields, which are among the most fundamental physical observables in high-energy hadronic collisions, have been intensively studied in hadron-collider and cosmic-ray physics for many decades [1]. Hadron production at collider energies originates from soft and hard scattering processes at the partonic level. Hard scatterings, where two partons interact with a large momentum transfer, are responsible for the production of particles with high transverse momenta ($p_T \gg 2 \text{ GeV}/c$). This process is theoretically described by perturbative Quantum Chromodynamics (pQCD) calculations based on the factorization theorem [2]. In this approach, the cross section is a convolution of the parton distribution function (PDF), the partonic QCD matrix elements, and the fragmentation function (FF). The PDFs describe the probability densities of finding a parton with a specific flavor carrying fraction x of the proton momentum, whereas the FFs encode the probability densities that the parton with a specific flavor fragments into a hadron carrying a fraction of the parton's longitudinal momentum; both considered at a given energy scale. At the LHC, with increasing center-of-mass collision energy (\sqrt{s}), the lower x regime is probed and contributions from hard-scattering processes increase. In the kinematic region probed by these measurements, high- p_T particles dominantly originate from the fragmentation of gluons [3, 4]. Parameterizations of both the PDFs and FFs are derived from global analyses [5, 6] based on fits to experimental data at various \sqrt{s} with next-to-leading order (NLO) accuracy. These include single-inclusive hadron production in semi-inclusive electron-positron annihilation data, semi-inclusive deep-inelastic scattering, and single inclusive hadron spectra at high p_T , notably including results at LHC energies. Results presented in this paper can be used as further input for these studies. In particular, identified particle spectra provide new constraints on the gluon-to-pion and, especially, gluon-to-kaon fragmentation functions [7, 8, 9, 10]. While particle production at high p_T is expected to be calculable with pQCD, the LHC results are in general not well reproduced by pQCD calculations, see Ref. [6] and references therein. Charged particle production at high p_T is known to scale with $x_T \equiv 2p_T/\sqrt{s}$, as observed in a wide energy range up to $\sqrt{s} = 7 \text{ TeV}$. This has been observed by the CDF Collaboration in pp collisions at the Tevatron [11, 12], by the UA1 Collaboration at the CERN SPS [13], by the STAR Collaboration in pp collisions at RHIC [14], and by the CMS Collaboration [15] at the CERN LHC. Above $x_T \simeq 10^{-2}$, significant deviations from the leading-twist NLO pQCD predictions have been reported in Ref. [16] and are investigated in this paper.

The bulk of particles produced at low transverse momenta ($p_T < 2 \text{ GeV}/c$) originate from soft scattering processes involving small momentum transfers. In this regime, particle production cannot be calculated from first principles. Instead, calculations rely on QCD inspired phenomenological models, which are tuned to reproduce previous measurements. Hence, measurements at low p_T provide further important constraints on such models. The universal transverse mass, $m_T \equiv \sqrt{m^2 + p_T^2}$, scaling originally proposed by R. Hagedorn [17] was first seen to hold approximately at ISR energies [18]. It was then observed by the PHENIX and STAR collaborations to hold only separately for mesons and baryons at RHIC energies, by applying the approximate m_T scaling relation respectively for pions and protons [19]. At $\sqrt{s} = 900 \text{ GeV}$ a disagreement was observed for charged kaons and $\phi(1020)$ mesons, which indicated a breaking of the generalized scaling behavior [20]. Moreover, recent studies, based on identified particle spectra measured in pp collisions at $\sqrt{s} = 7 \text{ TeV}$ by ALICE, indicate that m_T scaling also breaks in the low- p_T region [21]. These observations motivate studies of the applicability of m_T scaling of particle production through the precise measurement of identified hadrons at $\sqrt{s} = 13 \text{ TeV}$.

The results reported in this paper are the measurements of the production of π^\pm , K^\pm , K_S^0 , $K^*(892)^0$, $\bar{K}^*(892)^0$, p , \bar{p} , $\phi(1020)$, Λ , $\bar{\Lambda}$, Ξ^- , Ξ^+ , Ω^- and $\bar{\Omega}^+$ at the highest collision energies, and therefore extend the studies of the energy dependence of the production of light-flavor hadrons into new territory. The study of the production of the $K^*(892)^0$ and $\phi(1020)$ resonances, containing respectively one and two strange valence quarks, contributes to a better understanding of strange particle production mechanisms. Because of their short lifetimes ($\sim 4 \text{ fm}/c$ for $K^*(892)^0$ and $\sim 46 \text{ fm}/c$ for $\phi(1020)$), their decay daughters

may undergo re-scattering and/or regeneration processes that affect their yields and the shapes of their p_T distributions. In addition, multi-strange baryons, Ω^- ($\bar{\Omega}^+$) and Ξ^- ($\bar{\Xi}^+$), are of crucial importance due to their dominant strange (s) quark content. Furthermore, the production of K_S^0 , Λ , and $\bar{\Lambda}$ in pp collisions at $\sqrt{s} = 7$ TeV is reported here for the first time, completing the set of reference measurements at that energy [22, 23, 24, 25].

The present measurements serve as important baselines for studies of particle production as a function of the charged-particle multiplicity [26] or event shape (e.g. spherocity) [27] and also provide input to tune the modeling of several contributions in Monte Carlo (MC) event generators such as PYTHIA [28, 29] and EPOS-LHC [30]. In addition, measurements in minimum bias pp collisions reported in this paper serve as reference data to study nuclear effects in proton-lead (p–Pb) and lead-lead (Pb–Pb) collisions.

The paper is organized as follows. In Section 2 the ALICE experimental apparatus and the analyzed data samples are described, focusing on the detectors which are relevant for the presented measurements. In Section 3 the details of the event and track selection criteria and of the Particle IDentification (PID) techniques are discussed. The results are given in Section 4, in which the p_T spectra and the extraction procedures for the p_T -integrated yield and average p_T are presented. Section 5 discusses the results, followed by a summary in Section 6. For the remainder of this paper, the masses will be omitted from the symbols of the strongly decaying particles, which will be denoted as K^{*0} , \bar{K}^{*0} , and ϕ .

2 Experimental setup

A detailed description of the ALICE detector and its performance can be found in Refs. [31, 32]. The main subsystems of the ALICE detector used in this analysis are the V0 detector, the Inner Tracking System (ITS), the Time Projection Chamber (TPC), the Time of Flight (TOF) detector, and the High-Momentum Particle Identification Detector (HMPID).

The V0 detector [33] is used for triggering and beam background suppression. It is made up of two scintillator arrays placed along the beam axis on each side of the interaction point (IP) at $z = 340$ cm and $z = -90$ cm, covering the pseudorapidity regions $2.8 < \eta < 5.1$ (V0A) and $-3.7 < \eta < -1.7$ (V0C), respectively.

In the measurements of light-flavor hadrons, primary charged particles are considered. Primary particles are defined as particles with a mean proper lifetime τ that is larger than $1\text{ cm}/c$, which are either produced directly in the interaction or from decays of particles produced at the interaction vertex with τ shorter than $1\text{ cm}/c$. This excludes particles produced in interactions with the detector material [34]. Primary charged-hadron tracks are reconstructed by the ITS and TPC detectors, which have full azimuthal acceptance within $|\eta| < 0.8$ for full-length tracks. They are located inside a solenoidal magnet providing a magnetic field of $B = 0.5$ T.

The ITS [31, 35] is a silicon tracking detector made up of six concentric cylindrically-shaped layers, measuring high-resolution space points near the collision vertex. The two innermost layers consist of Silicon Pixel Detectors (SPD) used to reconstruct the primary vertex of the collision and short track segments called “tracklets”. The four outer layers are equipped with silicon drift (SDD) and strip (SSD) detectors and allow measurement of the specific energy loss (dE/dx) with a relative resolution of about 10%. The ITS is also used as a stand-alone tracking detector to reconstruct charged particles with momenta below 200 MeV/c that are deflected or decay before reaching the TPC.

The TPC [36] is the main tracking detector of ALICE. It is a large volume cylindrical drift detector spanning the approximate radial and longitudinal ranges $85 < r < 250$ cm and $-250 < z < 250$ cm, respectively. The endcaps of the TPC are equipped with multiwire proportional chambers (MWPCs) segmented radially into pad rows. Together with the measurement of the drift time, the TPC provides three dimensional space point information, with up to 159 tracking points. Charged tracks originating

from the primary vertex can be reconstructed down to $p \sim 100$ MeV/ c [32], albeit with a lower tracking efficiency for identified charged hadrons with $p_T < 200$ MeV/ c . Combining information from the ITS and TPC allows the momenta of charged particles to be measured for momenta from 0.05 to 100 GeV/ c with a resolution of 1–10%, depending on p_T . The TPC provides charged-hadron identification via measurement of the specific energy loss dE/dx in the fill gas, with a resolution of $\sim 5\%$ [36].

The Time of Flight detector (TOF) [37, 38, 39] is a cylindrical array of multi-gap resistive plate chambers which sits outside the TPC. It covers the pseudorapidity range $|\eta| < 0.9$ with (almost) full azimuthal acceptance. The total time-of-flight resolution, including the resolution on the collision time, is about 90 ps in pp collisions.

The HMPID consists of seven proximity focusing Ring Imaging Cherenkov (RICH) counters. Primary charged particles penetrate the radiator volume, filled with liquid C₆F₁₄, and generate Cherenkov photons that are converted into photoelectrons in thin CsI-coated photocathodes. Photo-electron clusters, together with pad clusters (also called “MIP” clusters) associated with the primary ionization of a particle, form Cherenkov rings. The amplified signal is read out by MWPCs, filled with CH₄. The detector covers $|\eta| < 0.5$ and $1.2^\circ < \phi < 58.5^\circ$, which corresponds to $\sim 5\%$ of the TPC geometrical acceptance.

3 Event and track selection

3.1 Event selection

The measurements at $\sqrt{s} = 13$ TeV are obtained from a minimum bias data sample of pp collisions collected in June 2015 during a period of low pileup in LHC Run 2. The minimum bias trigger required at least one hit in both of the V0 scintillator arrays in coincidence with the arrival of proton bunches from both directions along the beam axis. The mean number of proton-proton interactions per single bunch crossing ranges between 2% and 14%. A requirement of a coincidence of signals in both V0A and V0C detectors removes contamination from single-diffractive and electromagnetic events. Contamination arising from beam-induced background events, produced outside the interaction region, is removed offline by using timing information from the V0 detector, which has a time resolution better than 1 ns. Background events are further rejected by exploiting the correlation between the number of clusters and the multiplicity of tracklets in the SPD. From the triggered events, only events with a reconstructed primary vertex are considered for the analyses. Additionally, the position of the primary vertex along the beam axis is required to be within ± 10 cm with respect to the nominal interaction point (center of the ALICE barrel). This requirement ensures that the vast majority of reconstructed tracks are within the central barrel acceptance ($|\eta| < 0.8$) and it reduces background events by removing unwanted collisions from satellite bunches. Contamination from pileup events, which have more than one pp collision per bunch crossing, were rejected offline by excluding events with multiple primary vertices reconstructed in the SPD [32]. The pileup-rejected events are less than 1% of the total sample of events. The size of the analyzed sample after selections ranges between 40 and 60 million events (corresponding to an integrated luminosity $0.74 - 1.1 \text{ nb}^{-1}$), depending on the requirements of the analyses of the different particle species.

The measurements of K_S⁰, Λ , and $\bar{\Lambda}$ at $\sqrt{s} = 7$ TeV are obtained by analyzing a sample of about 150 million events (corresponding to an integrated luminosity 2.41 nb^{-1}) collected in 2010 during the LHC Run 1 data taking period. The corresponding trigger and event selection criteria applied were very similar to those used for the measurements at $\sqrt{s} = 13$ TeV; see Refs. [22, 40] for details on the triggering and event selection for these periods.

All corrections are calculated using Monte Carlo events from PYTHIA 6 and PYTHIA 8. The PYTHIA 6.425 (Perugia 2011 tune) and PYTHIA 8.210 (Monash 2013 tune) event generators were used for $\sqrt{s} = 13$ TeV. The PYTHIA 6.421 (Perugia 0 tune) was used for K_S⁰ and Λ at $\sqrt{s} = 7$ TeV because that pro-

duction was used for correcting the other $\sqrt{s} = 7$ TeV analyses. The particles produced using these event generators were propagated through a simulation of the ALICE detector using GEANT3 [41].

3.2 Track selection

Tracks from charged particles are reconstructed in the TPC and ITS detectors and then propagated to the outer detectors and matched with reconstructed points in the TOF and HMPID. Additionally, in the analysis of π^\pm , K^\pm and $p(\bar{p})$, a dedicated tracking algorithm based only on ITS information (ITS stand-alone, ITS-sa) was used to reconstruct low momentum tracks. In the measurements, global tracks, which are reconstructed using the combined ITS and TPC information, are distinguished from ITS-sa tracks.

For analyses using global tracks, track selection criteria are applied to limit the contamination due to secondary particles, to maximize tracking efficiency and improve the dE/dx and momentum resolution for primary charged particles, and to guarantee an optimal PID quality. The number of crossed pad rows in the TPC is required to be at least 70 (out of a maximum possible of 159); the ratio of the number of crossed pad rows to the number of findable clusters (that is the number of geometrically possible clusters which can be assigned to a track) is restricted to be greater than 0.8, see Ref. [32] for the details. The goodness-of-fit values χ^2 per cluster ($\chi^2/N_{\text{clusters}}$) of the track fit in the TPC must be less than 4. Tracks must be associated with at least one cluster in the SPD and the χ^2 values per cluster in the ITS are restricted in order to select high-quality tracks. The distance of closest approach (DCA) to the primary vertex in the plane perpendicular to the beam axis (DCA_{xy}) is required to be less than 7 times the resolution of this quantity; this selection is p_T dependent, i.e. $DCA_{xy} < 7 \times (0.0015 + 0.05 \times (p_T/(GeV/c))^{-1.01})$ cm. A loose selection criterion is also applied on the DCA in the beam direction (DCA_z), by rejecting tracks with DCA_z larger than 2 cm, to remove tracks from possible residual pileup events. The transverse momentum of each track must be greater than 150 MeV/c and the pseudorapidity is restricted to the range $|\eta| < 0.8$ to avoid edge effects in the TPC acceptance. Additionally, tracks produced by the reconstructed weak decays of pions and kaons (the “kink” decay topology) are rejected.

For the topological reconstruction of weakly decaying particles, the selected global tracks are combined using specific algorithms, as described in Sec. 4.3. Track selection criteria are the same applied for global tracks with a few exceptions: tracks that do not have ITS information available are included in the reconstruction of K_S^0 , Λ , $\bar{\Lambda}$, Ξ^- , Ξ^+ , Ω^- , and $\bar{\Omega}^+$. The kink topology tracks are used to reconstruct the weak decays of K^\pm and the tracks that do not have ITS information. For the latter, removal of contributions from pileup collisions outside the trigger proton bunch (“out-of-bunch pileup”) is achieved by requiring that at least one charged decay track matches a hit in a “fast” detector (either the ITS or the TOF detector).

ITS stand-alone tracking uses similar selection criteria to those mentioned above. Tracks are required to have at least four ITS clusters, with at least one in the SPD, three in the SSD and SDD and $\chi^2/N_{\text{clusters}} < 2.5$. This further reduces contamination from secondary tracks and provides high resolution for the track impact parameter and optimal resolution for dE/dx . Similar to global tracks, a p_T -dependent parameterization of the DCA_{xy} selection is used, but with different parameters to account for the different resolution. For the p_T ranges used in this analysis, the selected ITS-sa tracks have the same p_T resolution as those measured in pp collisions at $\sqrt{s} = 7$ TeV: 6% for pions, 8% for kaons, and 10% for protons [22].

4 Data analysis techniques

Table 1 lists the basic characteristics of the particles studied in this paper. This section describes the techniques used to measure the yields of the various hadron species. In Sec. 4.1, aspects common to all analyses are described, including the correction and normalization procedure and the common sources of systematic uncertainties. Next, the analysis of each hadron species is described in detail. The measurements of charged pions, charged kaons, and (anti)protons, which are performed using several different

Table 1: Main characteristics of the reconstructed particles: valence quark content, mass, proper decay length ($c\tau$), the decay channel studied in this paper, and the corresponding branching ratio (B.R.) [42].

Particle	Valence Quark Content	Mass (MeV/ c^2)	$c\tau$	Decay	B.R. (%)
π^+	u \bar{d}	139.57	7.8 m	—	—
K $^+$	u \bar{s}	493.68	3.7 m	K $^+$ $\rightarrow \mu^+ \nu_\mu$	63.56 \pm 0.11
K $_S^0$	$\frac{1}{\sqrt{2}}(\bar{d}\bar{s} - \bar{d}\bar{s})$	497.61	2.68 cm	K $_S^0 \rightarrow \pi^+ + \pi^-$	69.20 \pm 0.05
K *0	d \bar{s}	895.55	4.16 fm	K $^{*0} \rightarrow \pi^- + K^+$	\sim 66.6
ϕ	s \bar{s}	1019.46	46.2 fm	$\phi \rightarrow K^+ + K^-$	49.2 \pm 0.5
Mesons	p	938.27	—	—	—
	Λ	1115.68	7.89 cm	$\Lambda \rightarrow p + \pi^-$	63.9 \pm 0.5
	Ξ^-	1321.71	4.91 cm	$\Xi^- \rightarrow \Lambda + \pi^-$	99.887 \pm 0.035
	Ω^-	1672.45	2.46 cm	$\Omega^- \rightarrow \Lambda + K^-$	67.8 \pm 0.7
Baryons					

PID techniques, are described in Sec. 4.2. It is worth noting that charged kaons are also identified using the kink topology of their two-body decays. The measurements of weakly decaying strange hadrons (K $_S^0$, Λ , Ξ^- , Ω^- and their antiparticles) are reported in Sec. 4.3, followed by the strongly decaying resonances (K *0 , \bar{K}^{*0} , and ϕ) in Sec. 4.4.

4.1 Common aspects of all analyses

In several of the analyses presented below, the measured PID signal is compared to the expected value based on various particle mass hypotheses. The difference between the measured and expected values is expressed in terms of σ , the standard deviation of the corresponding measured signal distribution. The size of this difference, in multiples of σ , is denoted n_σ . In the following, the σ values accounting for the resolution of the PID signals measured in the TPC and TOF detectors are denoted as σ_{TPC} and σ_{TOF} , respectively.

The corrected yield of each hadron species as a function of p_T is

$$Y_{\text{corr}} = \frac{Y_{\text{raw}}}{\Delta p_T \Delta y} \times \frac{f_{\text{SL}}}{A \times \epsilon} \times (1 - f_{\text{cont}}) \times f_{\text{cross.sec.}} . \quad (1)$$

Y_{corr} is obtained by following the procedure described in previous publications. Here, Y_{raw} is the number of particles measured in each p_T bin and $A \times \epsilon$ is the product of the acceptance and the efficiency (including PID efficiency, matching efficiency, detector acceptance, reconstruction, and selection efficiencies). Monte Carlo simulations are used to evaluate $A \times \epsilon$, which takes on similar values to those found in our previous analyses. The factor f_{SL} , also known as the “signal-loss” correction, accounts for reductions in the measured particle yields due to event triggering and primary vertex reconstruction. Such losses are more important at low p_T , since events that fail the trigger conditions or fail to have a reconstructible primary vertex tend to have softer particle p_T spectra than the average inelastic collision. For $\sqrt{s} = 13$ TeV, f_{SL} deviates from unity by a few percent at low p_T to less than one percent for $p_T \gtrsim 2$ GeV/ c . The trigger configuration used for $\sqrt{s} = 7$ TeV resulted in negligible signal loss, thus f_{SL} is set to unity for this energy. The factor $(1 - f_{\text{cont}})$ is used to correct for contamination from secondary and misidentified particles; f_{cont} is non-zero only for the measurements of π^\pm , K $^\pm$, p(\bar{p}), Λ , and $\bar{\Lambda}$, and it is more important at low p_T . The computation of f_{cont} for those species is described further in the relevant sections below. The factor $f_{\text{cross.sec.}}$ corrects for inaccuracies in the hadronic production cross sections in GEANT3, which is used in the calculation of $A \times \epsilon$ to describe the interactions of hadrons with the detector material of ALICE. GEANT4 and FLUKA [43], which have more accurate descriptions of the hadronic cross sections, are used to calculate the correction factor, which can be different from

unity by up to a few percent. The correction $f_{\text{cross.sec.}}$ is applied only for the analyses of K^- , \bar{p} , $\bar{\Lambda}$, $\bar{\Xi}^+$, and $\bar{\Omega}^+$.

After correction, the yields are normalized to the number of inelastic pp collisions using the ratio of the ALICE visible cross section to the total inelastic cross section. This ratio is $0.852^{+0.062}_{-0.030}$ for $\sqrt{s} = 7$ TeV [44] and 0.7448 ± 0.0190 for $\sqrt{s} = 13$ TeV [45, 46].

The procedures for the estimation of systematic uncertainties strictly follow those applied in our measurements from LHC Run 1. All described uncertainties are assumed to be strongly correlated among adjacent p_T bins. For the evaluation of the total systematic uncertainty in every analysis, all contributions originating from different sources are considered to be uncorrelated and summed in quadrature. Components of uncertainties related to the ITS-TPC matching efficiency correction and to the event selection are considered correlated among different measurements. The systematic uncertainty due to the normalization to the number of inelastic collisions is $\pm 2.6\%$ for $\sqrt{s} = 13$ TeV and $^{+7.3\%}_{-3.5\%}$ for $\sqrt{s} = 7$ TeV independent of p_T . This uncertainty is common to all measured p_T spectra and dN/dy values (see Sec. 5.1) at a given energy. The systematic uncertainty associated to possible residual contamination from pileup events was estimated varying pileup rejection criteria and was found to be of 1%. The singal loss correction has a small dependence on the Monte Carlo event generator used to calculate it. These variations result in p_T -dependent uncertainties that are largest at low p_T , where they have values of 0.2% for Ω , $\sim 1\%$ for π^\pm , K^\pm , $p(\bar{p})$, and Ξ , and $\sim 2\%$ for K_S^0 , $\bar{\Lambda}$, K^{*0} , and ϕ .

The systematic uncertainty accounting for the limited knowledge of the material budget is estimated by varying the amount of detector material in the MC simulations within its expected uncertainties [32]. For the analysis of π^\pm , K^\pm , $p(\bar{p})$, K^{*0} , and ϕ , the values are taken from the studies reported in Refs. [47] and [48]. This uncertainty is estimated to be around 3.3% for K^\pm , 1.1% for π^\pm , 1.8% for $p(\bar{p})$, 3% for K^{*0} , and 2% for ϕ ; it is largest at low momenta and tends to be negligible towards higher momenta. For the measurement of K_S^0 and Λ at $\sqrt{s} = 7$ TeV, the material budget uncertainty is estimated to be 4%, independent of p_T . For the measurements of K_S^0 , Λ , Ξ and Ω at $\sqrt{s} = 13$ TeV, the material budget uncertainty is p_T dependent for low p_T ($\lesssim 2$ GeV/c) and constant at higher p_T . For low p_T , the uncertainty reaches maximum values of about 4.7% for K_S^0 , 6.7% for Λ , 6% for Ξ , and 3.5% for Ω ; at high p_T , the uncertainty is less than 1% for K_S^0 , Λ , and Ξ , and about 1.5% for Ω .

The systematic uncertainty due to the limited description of the hadronic interaction cross sections in the transport code is evaluated using GEANT4 and FLUKA. This leads to uncertainties of up to 2.8% for π^\pm , 2.5% for K^\pm , 0.8% for p , and 5% for \bar{p} [47]. It is at most 3% for K^{*0} , 2% for ϕ and 1–2% for the strange baryons. It is negligible for K_S^0 at both reported collision energies. In the following sections, details are given on the contributions (specific to each analysis) related to track or topological selections and signal extraction methods, as well as those related to feed-down.

4.2 Identification of primary charged pions, charged kaons, and (anti)protons

To measure the production of primary charged pions, kaons, and (anti)protons over a wide range of p_T , five analyses using distinct PID techniques were carried out. The individual analyses follow the techniques adopted in previous measurements based on data collected at lower center-of-mass energies and for different collision systems during LHC Run 1 [49, 50, 22, 23, 51]. The p_T -spectra have been measured from $p_T = 0.1$ GeV/c for pions, $p_T = 0.2$ GeV/c for kaons, and $p_T = 0.3$ GeV/c for protons, up to 20 GeV/c for all three species. The individual analyses with their respective p_T reaches are summarized in Tab. 2. All the analysis techniques are extensively described in Refs. [49, 47, 22, 7]. Each procedure is discussed separately in Secs. 4.2.1–4.2.5, with special emphasis on those aspects that are relevant for the current measurements. The results for the different analyses are then combined as described in Sec. 4.2.6.

Table 2: Summary of the kinematic ranges (p_T (GeV/c) and η or y) covered by the individual analyses for the measurement of π^\pm , K^\pm and $(\bar{p})p$ in pp collisions at $\sqrt{s} = 13$ TeV.

Analysis technique	p_T range (GeV/c)			η or y range
	$\pi^+ + \pi^-$	$K^+ + K^-$	$p + \bar{p}$	
ITS-sa	0.1 – 0.7	0.2 – 0.6	0.3 – 0.65	$ y < 0.5$
TPC-TOF fits	0.3 – 3.0	0.3 – 3.0	0.4 – 3.0	$ y < 0.5$ $ \eta < 0.4$
HMPID	1.5 – 4	1.5 – 4	1.5 – 6	$ y < 0.5$
Kinks	–	0.2 – 7	–	$ y < 0.5$
TPC rel. rise	2 – 20	3 – 20	3 – 20	$ \eta < 0.8$

The calculation of f_{cont} in Eq. 1 at low p_T is performed by subtracting the secondary π^\pm , K^\pm , and $p(\bar{p})$ from the primary particle sample. This method is data-driven and it is based on the measured distance of closest approach to the primary vertex in the plane transverse to the beam direction (DCA_{xy}), following the same procedure adopted in Ref. [22]. The DCA_{xy} distribution of the selected tracks was fitted in every p_T bin with Monte Carlo templates composed of three ingredients: primary particles, secondaries from material and secondaries from weak decays, each accounting for the expected shapes of the distribution. Because of the different track and PID selection criteria, the contributions are different for each analysis. The resulting corrections are significant at low p_T and decrease towards higher p_T due to decay kinematics. Up to $p_T = 2$ GeV/c, the contamination is 2 – 10% for pions, up to 20% for kaons (in the narrow momentum range where the dE/dx response for kaons and secondary electrons overlap), and 15 – 20% for protons.

The main sources of systematic uncertainties for each analysis are summarized in Tab. 3, including contributions common to all analyses. The systematic uncertainty due to the subtraction of secondary particles is estimated by changing the fit range of the DCA_{xy} distribution, resulting in uncertainties of up to 4% for protons and 1% for pions, with negligible uncertainties for kaons. The uncertainty due to the matching of TPC tracks with ITS hits is estimated to be in the range $\sim 1 – 5\%$ for $p_T \lesssim 3$ GeV/c depending on p_T , while it takes values around 6% at higher p_T . This uncertainty together with that resulting from the variation of the track quality selection criteria lead to the systematic uncertainty of the global tracking efficiency that varies from 2.2 to 7.3% from low to high p_T , independent of particle species.

4.2.1 ITS stand-alone

In the “ITS stand-alone” analysis, both tracking and PID are performed based on information from the ITS detector only. For the present data sample, the contribution of tracks with wrongly assigned clusters in the ITS is negligible due to the low pseudorapidity density of charged particles, $\langle dN_{\text{ch}}/d\eta \rangle_{|\eta| < 0.5} = 5.31 \pm 0.18$, measured in the pseudorapidity region $|\eta| < 0.5$ [52]. The average dE/dx signal in the four outer ITS layers used for PID is estimated by means of the truncated mean method [49]. The measured dE/dx for the sample of ITS-sa tracks is shown in the top left panel of Fig. 1, along with the Bethe–Bloch parametrization of the most probable values, which is the same as the one used for the LHC Run 1 analyses [22]. Two identification strategies were used. In the main analysis, a unique identity is assigned to the ITS-sa track according to the mass hypothesis for which the expected specific energy-loss value is the closest to the measured dE/dx for a track with momentum p . The second analysis strategy uses the Bayesian PID approach [53], based on likelihood parametrization with a set of iterative prior probabilities. The identification is based on the maximal probability method in which the species with the highest probability is assigned to a track. For $p_T < 160$ MeV/c, where the e/π separation power in the ITS allows high-purity identification of electrons, four mass hypotheses ($e/\pi/K/p$) are considered.

Table 3: Summary of the main sources and values of the relative systematic uncertainties (expressed in %) for the $\pi^+ + \pi^-$, $K^+ + K^-$, and $p + \bar{p}$ p_T -differential yields. A single value between two or three columns indicates that no p_T dependence is observed. Values are reported for low, intermediate (wherever they are available) and high p_T .

Hadron species	π^\pm			K^\pm			$p (\bar{p})$		
Source of uncertainty common to all analyses (%)									
p_T (GeV/c)	0.3	2.5	20	0.25 2.5 20			0.45	2.5	20
Feed-down correction ¹	1.0	1.0	0.3	negl.			4.0	1.3	
Hadronic interaction	2.8	2.4		2.5	1.8		0.8 (5.0)	4.6	
Material budget	0.5	1.1	0.2	3.3	1.0	0.3	1.7	1.8	0.1
Signal-loss correction	1.0	0.3	0.2	0.9	0.3	0.2	1.0	0.2	0.2
Global tracking efficiency ²	2.2	5.3	7.3	2.0	5.3	7.3	2.0	5.3	7.3
Source of uncertainty specific to an analysis (%)									
p_T (GeV/c)	0.3	1.6	2.8	0.3	1.6	2.8	0.4	1.6	2.8
TPC-TOF fits PID	0.8	4.0	8.0	2.0	6.5	14.0	1.0	2.2	7.0
TOF matching efficiency	3.0			6.0			4.0		
p_T (GeV/c)	1.5	2.5	4.0	1.5	2.5	4.0	1.5	4.0	6.0
HMPID PID	3.0	3.5	12.0	3.0	3.5	12.0	3.0	9.0	11.0
Distance cut correction	3.0	3.0	2.0	3.0	2.0	2.0	4.0	4.0	2.0
p_T (GeV/c)	2.0	10	20	3.0	10	20	3.0	10	20
TPC relativistic rise PID	1.4	2.2	2.3	15.0	7.2	6.5	17.0	13.0	13.0
p_T (GeV/c)	—			0.25	2.0	7.0	—		
Kink PID	—			2.5	2.2	2.2	—		
Reconstruction efficiency	—			3.0			—		
Contamination	—			negl.	5.0	3.0	—		
p_T (GeV/c)	0.1	0.7		0.2	0.6		0.3	0.65	
ITS-sa PID	3.1	5.2		1.3	4.6		4.5	0.6	
$\mathbf{E} \times \mathbf{B}$ effect	2.1			2.1			2.1		
ITS-sa tracking efficiency	4.1	4.3		5.3	4.3		9.8	3.7	
p_T (GeV/c)	0.1	2.5	20	0.2	2.5	20	0.3	2.5	20
Total	8.0	6.5	8.1	7.0	6.3	10.8	8.4	7.3	15.8

¹ Note that in TPC relativistic rise analysis the systematic uncertainty is estimated as half of the applied correction, which is not based on DCA template fits.

² This source of uncertainty includes components related to the matching of TPC tracks with ITS hits and the track quality selection criteria. These two components were taken from the analysis of inclusive charged hadrons [52], and are excluded in ITS-sa analysis.

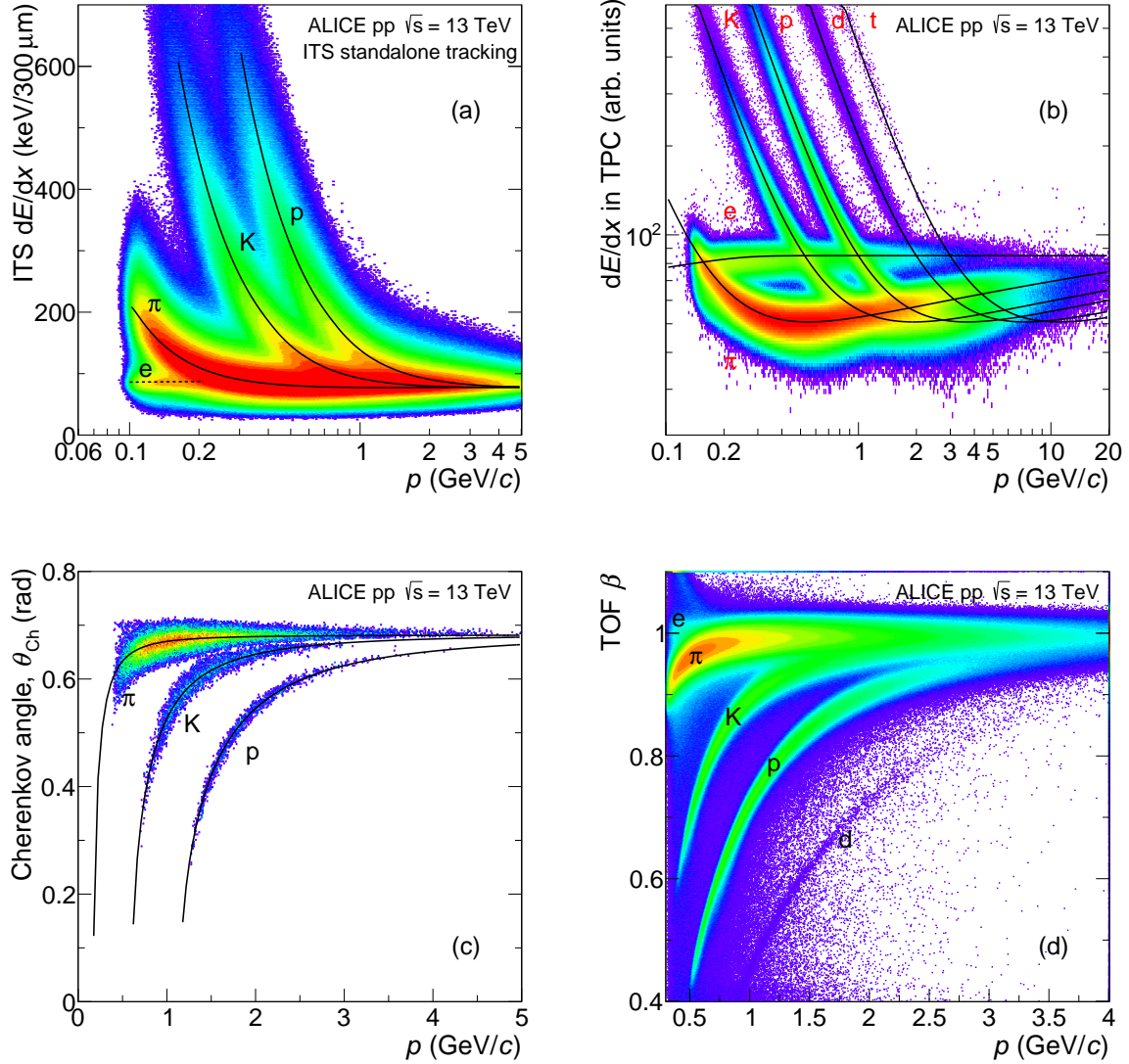


Figure 1: The performance during the LHC Run 2 period of the ALICE central barrel detectors used for the measurements described in this paper. Panels a), b), c), and d) indicate the characteristic signal distributions of identified charged particles measured by the ITS, TPC, TOF, and HMPID detector, respectively.

For $p_T > 160 \text{ MeV}/c$, electrons and pions cannot be separated using their dE/dx in the ITS detector, and the Bayesian approach is based on the $\pi/\text{K}/\text{p}$ mass hypotheses only.

For the ITS-sa analysis, the systematic uncertainties related to the PID procedure originate from the different techniques that are used (the truncated mean method and the Bayesian PID approach). These range from about 1 to 5% depending on particle species and p_T . The Lorentz force causes the migration of the cluster position in the ITS by driving the charge in opposite directions depending on the polarity of the magnetic field of the experiment ($\mathbf{E} \times \mathbf{B}$ effect). The uncertainty related to this effect is estimated by analyzing data samples with opposite magnetic field polarities, for which a difference at the level of $\sim 2\%$ is observed.

4.2.2 TPC-TOF fits

In the so-called “TPC-TOF fits” analysis, the distributions of the specific energy loss dE/dx measured in the TPC and the velocity β measured in the TOF detector are fitted with functions that describe the PID signals for different track momentum (p) intervals. The TPC provides a $3\sigma_{\text{TPC}}$ separation between pions and kaons up to $p_T \sim 600 \text{ MeV}/c$ and between kaons and protons up to $p_T \sim 800 \text{ MeV}/c$.

Particle identification using this technique is possible in the p_T ranges $0.3 < p_T < 0.5 \text{ GeV}/c$, $0.3 < p_T < 0.6 \text{ GeV}/c$, and $0.4 < p_T < 0.8 \text{ GeV}/c$ for π^\pm , K^\pm , and $\text{p}(\bar{\text{p}})$, respectively. The extraction of the raw yield for a given species is done by integrating the $d^2N/dp_T dn_\sigma$ distribution in these p_T intervals. In addition, in transverse momentum ranges $p_T < 0.4 \text{ GeV}/c$ for π^\pm , $p_T > 0.45 \text{ GeV}/c$ for K^\pm , and $p_T > 0.6 \text{ GeV}/c$ for $\text{p}(\bar{\text{p}})$, a Gaussian fit is used to remove the background contribution (e^\pm for pions, π^\pm for kaons, and $\text{K}^\pm + e^\pm$ for (anti)protons). The background contribution is small (< 1%) in all cases, except for K^\pm at $p_T > 0.55 \text{ GeV}/c$, where it reaches $\sim 13\%$. The TOF analysis uses the sub-sample of global tracks for which the information from the time-of-flight measurement is available. The procedure is performed in narrow regions of pseudorapidity, $|\eta| < 0.2$ and $0.2 < |\eta| < 0.4$, in order to achieve a sufficient level of separation and to strengthen the correlation between the total momentum and the transverse momentum. The TOF matching efficiency for the presented data sample in the pseudorapidity region $|\eta| < 0.2$ ($0.2 < |\eta| < 0.4$) increases rapidly with p_T up to around 50% (60%) for pions at $p_T \sim 700 \text{ MeV}/c$, 45% (55%) for kaons at $p_T \sim 1 \text{ GeV}/c$, and 50% (65%) for protons at $p_T \sim 800 \text{ MeV}/c$; it saturates at higher momenta. The PID performance of the TOF detector is shown in the bottom right panel of Fig. 1, where the velocity β of the particles is reported as a function of momentum p . The raw particle yields are then obtained by fitting the measured β distributions with a TOF response function, where the contribution for a given species is centered around $\beta = p/E$. An additional template is added to account for wrongly associated (mismatched) hits in the TOF detector.

The TPC-TOF fits analysis includes uncertainties related to the PID procedure from several sources. For TPC part, uncertainties are estimated by integrating the $d^2N/dp_T dn_\sigma$ distribution for each particle species in $|n_\sigma| < 2.5$ and $|n_\sigma| < 3.5$, and compared to the integral of the underlying distribution performed within $|n_\sigma| < 3$; the larger resulting uncertainty is used. Similarly, for TOF fits for $p_T < 1.5 \text{ GeV}/c$, the uncertainty related to PID is estimated by integrating the $d^2N/dp_T dn_\sigma$ in the range of $|n_\sigma| < 3$. This results in uncertainties of up to 1% for π^\pm , 5% for K^\pm , and 2% for (anti)protons. At higher p_T , where the separation between particle species becomes small, a better estimate of the uncertainty of the method can be achieved by varying simultaneously the resolution σ_{TOF} and the tail parameter [22, 54] of the fit function used to describe the PID signal around their nominal values. An additional uncertainty is included to account for the TOF miscalibration, which becomes significant for $p_T > 1.5 \text{ GeV}/c$. This results in uncertainties of up to 8% for π^\pm , 14% for K^\pm , and 7% for (anti)protons. An uncertainty related to the matching of tracks to TOF hits arises from differences in the TPC-TOF matching efficiency in real data and simulations. This uncertainty is 3% for π^\pm , 6% for K^\pm , and 4% for (anti)protons, independent of p_T .

4.2.3 HMPID

The HMPID analysis extends charged hadron identification into the intermediate- p_T region ($2 \text{ GeV}/c \lesssim p_T \lesssim 10 \text{ GeV}/c$), combining the measurement of the emission angle of the Cherenkov photons θ_{Ch} and the momentum information of the particle under study. The Cherenkov photons are selected using the Hough Transform Method [55]. The measurement of the single photon θ_{Ch} angle in the HMPID requires the determination of the track parameters, which are calculated for tracks propagated from the central tracking detectors to the radiator volume where the Cherenkov photons are emitted. Each track is extrapolated to the HMPID cathode plane and matched to the closest primary ionization (MIP) cluster. The distance within the cathode plane between the extrapolated track and the matched cluster (denoted $d_{\text{MIP-track}}$) is restricted to be less than 5 cm to reduce false matches. A mean Cherenkov angle $\langle \theta_{\text{Ch}} \rangle$, computed as the weighted average of single photon angles, is associated to each particle track. The PID performance is shown in the bottom left panel of Fig. 1, where the correlation between the reconstructed Cherenkov angle and the track momentum is shown, indicating good agreement with the theoretically expected values. For yield extraction, a statistical unfolding technique is applied by fitting the reconstructed Cherenkov angle distribution in a given momentum interval, which requires a precise knowledge of the detector response function. Yields are evaluated from the integral of each of the three Gaussian functions, corresponding to the signals from pions, kaons, and protons. The HMPID allows pion and kaon identification in the momentum range $1.5 < p < 4 \text{ GeV}/c$, while (anti)protons can be distinguished from pions and kaons up to $p = 6 \text{ GeV}/c$, with separation powers larger than 2σ .

Additionally, in the HMPID analysis, a data-driven correction for the selection criterion on the distance $d_{\text{MIP-track}}$ has been evaluated by taking the ratio between the number of tracks that pass the selection criterion on $d_{\text{MIP-track}}$ and all the tracks in the detector acceptance. This correction is p_T dependent and it is about 20 – 40%; it is lower for particles with velocity $\beta \sim 1$. Negatively charged particle tracks have a distance correction $\sim 3\%$ lower than positive ones due to a radial residual misalignment of the HMPID chambers and an imperfect estimation of the energy loss in the material traversed by the track.

In the HMPID analysis, the systematic uncertainty has contributions from tracking, PID, and track association [22, 50]. The PID uncertainties are estimated by varying the parameters of the fit function used to extract the raw particle yield. This uncertainty is p_T -dependent and increases with p_T to a maximum value of 12% for π^\pm and K^\pm , and 11% for (anti)protons. Furthermore, the uncertainty of the association of the global track to the charged particle signal in the HMPID is obtained by varying the default value of the $d_{\text{MIP-track}}$ distance criterion required for the matching. The resulting uncertainty is p_T -dependent with a maximum value of about 4% for (anti)protons at $p_T = 1.5 \text{ GeV}/c$.

4.2.4 TPC relativistic rise

In the TPC dE/dx relativistic rise analysis charged pions, charged kaons, and (anti)protons can be identified up to $p_T = 20 \text{ GeV}/c$. The identification is achieved by measuring the specific energy loss dE/dx in the TPC in the relativistic rise regime of the Bethe–Bloch curve. The dE/dx as a function of momentum p is shown in the top right panel of Fig. 1, indicating the $\langle dE/dx \rangle$ response for charge-summed π^\pm , K^\pm , $p(\bar{p})$, and e^\pm . The separation power between particle species is about $4.5\sigma_{\text{TPC}}$ ($1.5\sigma_{\text{TPC}}$) for $\pi - p$ ($K - p$) at $p_T = 10 \text{ GeV}/c$, and it is nearly constant at similar values for larger momenta. The results presented in this paper were obtained using the method detailed in Ref. [50]. As discussed in Refs. [7, 50, 22, 23], dE/dx is calibrated taking into account chamber gain variations, track curvature and diffusion to obtain the best possible overall performance, which results in a response that essentially only depends on $\beta\gamma (= p/m)$. The resolution is better at larger rapidities for the same $\langle dE/dx \rangle$ because of the longer integrated track-lengths. Hence, to analyze homogeneous samples, the analysis is performed in four equal-width intervals within $|\eta| < 0.8$ ($|\eta| < 0.2$, $0.2 < |\eta| < 0.4$, $0.4 < |\eta| < 0.6$ and $0.6 < |\eta| < 0.8$). Samples of topologically identified pions from K_S^0 decays, protons from Λ decays, and electrons from photon conversions were used to parameterize the Bethe–Bloch response $\langle dE/dx \rangle$ as a

function of $\beta\gamma$ and the relative resolution $\sigma_{\text{TPC}}/\langle dE/dx \rangle$ as a function of $\langle dE/dx \rangle$. The relative yields of pions, kaons, protons, and electrons are obtained as the $\pi^+ + \pi^-$, $K^+ + K^-$, $p + \bar{p}$, and $e^+ + e^-$ yields normalized to that for inclusive charged particles. They are obtained using four-Gaussian fits to dE/dx distributions differentially in p and $|\eta|$ intervals. The parameters (mean and width) of the fits are fixed using the parameterized Bethe–Bloch and resolution curves. The relative yields as a function of p_T are found to be independent of η and therefore averaged. Particle yields are constructed using the corrected relative yields and the corrected charged particle yields [52]. A Jacobian correction is applied to account for the pseudorapidity-to-rapidity conversion.

In the TPC dE/dx relativistic rise analysis, the pion and (anti)proton yields are corrected for secondary particles from weak decays using MC simulations for the relative fraction of secondaries. The obtained fraction of secondary pions and (anti)protons are scaled to those extracted from DCA_{xy} template fits to data. For $p_T \gtrsim 3 \text{ GeV}/c$, the correction is negligible for pions. It is $\sim 2\%$ for (anti)protons at $p_T = 3 \text{ GeV}/c$, decreases to $\sim 1\%$ at $p_T = 10 \text{ GeV}/c$, and stays constant from that p_T onward. Moreover, at high p_T , there is a small contamination of primary muons in the pion yields. Due to the similar muon and pion masses, the electron (fractional) yield is subtracted from the pion yield to correct for the muon contamination. This procedure gives a $< 1\%$ correction to the pion yield in the entire p_T range considered in the analysis. Furthermore, above $p_T = 3 \text{ GeV}/c$, both the contamination of kaons and the contamination of (anti)deuterons in the (anti)proton sample are negligible.

The tracking efficiency component is calculated as a relative correction factor. It is the ratio of the inclusive to identified charged particle efficiencies, and applied on the relative yields. At high p_T this correction is nearly constant, of the order of $3 - 6\%$, depending on the particle species.

In the TPC dE/dx relativistic rise analysis, the systematic uncertainties mainly originate from event and track selection and the PID procedure. The first component is based on the study of inclusive charged particles [52], and it was recalculated to meet the event selection condition for inelastic events. Its value is estimated to be 7.3% at high p_T (at which the respective value is largest). It is the main contribution for pions. The second component was measured following the procedure explained in Ref. [50]. Here, the largest contribution is due to the uncertainties in the parameterization of the dE/dx response, resulting in uncertainties of $6.5 - 15\%$ for K^\pm and $13 - 17\%$ for (anti)protons, depending on p_T .

4.2.5 Topological reconstruction of K^\pm kink decays

Charged kaons are also measured by reconstructing the vertex of their weak decay in the TPC. The procedure extends the p_T reach of the identification of charged kaons on a track-by-track basis from $4 \text{ GeV}/c$ (available with the HMPID) up to $7 \text{ GeV}/c$. This method exploits the characteristic kink topology defined by the decay of a charged mother particle to a daughter with the same charge and neutral daughter [22]. Thanks to the two-body kinematics of the kink topology, it is possible to separate kaon decays from the background mainly caused by pion decays. For this purpose, a topological selection is applied by imposing a selection criterion on the daughter track's momentum with respect to that of the mother track, and on the decay angle, defined as the angle between the momenta of the mother and the charged daughter track. Furthermore, mother tracks are selected inside a $3.5\sigma_{\text{TPC}}$ band of the expected dE/dx for kaons to enhance the purity of the sample. With the assumption that the charged daughter track is a muon and the undetected neutral daughter particle is a neutrino, the reconstructed invariant mass $M_{\mu\nu}$ is calculated and is shown in Fig. 2. The raw yield of the topologically selected kaons in a given p_T bin are obtained from the integral of the invariant mass distribution after the topological selection criteria. The contamination due to fake kinks increases with p_T and saturates at $p_T \sim 1 \text{ GeV}/c$, reaching a maximum value of about 5%.

For the topological identification of charged kaons, the size of the correction related to contamination (arising from background or misidentification) was assigned as a p_T -dependent uncertainty on the purity. The kink identification uncertainty is p_T dependent and it ranges from 2.5% at low p_T to 2.2% at high

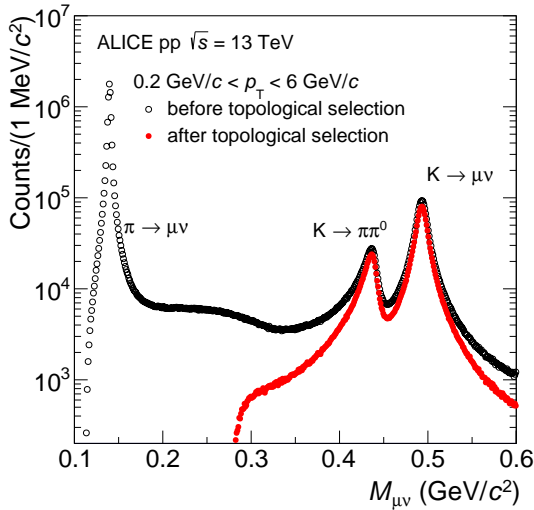


Figure 2: Kink invariant mass distribution for charge summed particles in the mother particle transverse momentum interval $0.2 \text{ GeV}/c < p_T < 6 \text{ GeV}/c$, before (open circle) and after (full circle) topological selections.

p_T . The systematic uncertainty on the efficiency for findable kink vertices was estimated to be 3%, independent of p_T . The uncertainty due to contamination from fake kinks was estimated to be at most about 5% around $p_T = 2 \text{ GeV}/c$, decreasing towards higher p_T .

4.2.6 Combination of π^\pm , K^\pm , and $p(\bar{p})$ spectra from different analyses

The charged pion, charged kaon and (anti)proton transverse momentum spectra were measured via several independent analyses as described in the preceding sections. To ensure the maximal p_T coverage, the final p_T spectra were calculated as the average of all analyses weighted by the systematic uncertainties that are not shared between analyses, i.e. uncorrelated. The uncertainties related to the ITS-TPC matching efficiency and the global tracking efficiency are largely correlated and were summed in quadrature with the uncorrelated part of the systematic uncertainties obtained after the averaging. Only the TPC relativistic rise analysis is used above $p_T = 4, 7$, and $6 \text{ GeV}/c$ respectively for pions, kaons, and protons. To verify the validity of the procedure, the spectra obtained from the individual analyses were compared to the final combined ones. The left panel of Fig. 3 shows the π^\pm , K^\pm , and $p(\bar{p})$ spectra obtained from the five analyses discussed above, which are normalized to the number of inelastic collisions (N_{INEL}). The right panel of Fig. 3 shows the ratios of the individual spectra to the combined spectra, which illustrates an excellent agreement in the overlapping p_T regions for every particle species within the uncorrelated part of the systematic uncertainties.

4.3 Topological identification of weakly-decaying strange hadrons

Primary strange hadrons K_S^0 , Λ , $\bar{\Lambda}$, Ξ^- , Ξ^+ , Ω^- , and $\bar{\Omega}^+$ are reconstructed at midrapidity ($|y| < 0.5$) via their characteristic weak decay topologies in the channels presented in Tab. 1. Single-strange hadrons K_S^0 , Λ and $\bar{\Lambda}$ decay into two oppositely charged daughter particles (V^0 decay). Multi-strange hadrons (Ξ and Ω) decay into a charged meson (bachelor) plus a V^0 decaying particle, giving the two-step process known as a cascade. The identification methods for the V^0 (K_S^0 and Λ) and cascade-like (Ξ and Ω) candidates strictly follow those presented in earlier works [56, 25]. An additional selection criterion on (anti)proton momentum ($p > 0.31 \text{ GeV}/c$) measured at the inner wall of TPC was introduced because of the observed instability of track reconstruction for the lowest p_T bin of Λ and $\bar{\Lambda}$ spectra. Several track, PID, and topological selection criteria are applied in order to find V^0 and cascade decay candidates. Charged tracks are selected using the standard criteria described in Sec. 3.2. The identity of these daughter tracks is established with the requirement that the specific energy loss dE/dx measured in the TPC is compatible with the expected mass hypothesis within $5\sigma_{\text{TPC}}$ ($4\sigma_{\text{TPC}}$) for the analysis of K_S^0 and Λ (Ξ and Ω).

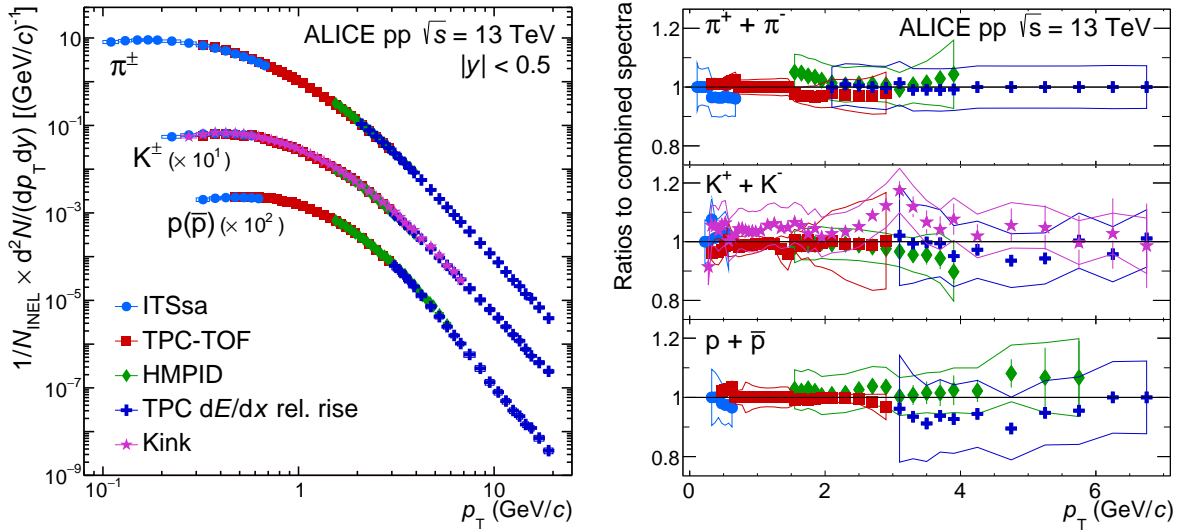


Figure 3: Left panel: p_T spectra of π^\pm , K^\pm , and $p(\bar{p})$ measured at midrapidity ($|y| < 0.5$) in pp collisions at $\sqrt{s} = 13$ TeV using different PID techniques. The spectra are normalized to the number of inelastic collisions. Right panel: The ratios of individual spectra to the combined spectra as a function of p_T for π^\pm (top), K^\pm (middle), and $p(\bar{p})$ (bottom). Only the p_T -range where the analyses overlap is shown. The vertical bars indicate statistical uncertainties while the bands show the uncorrelated systematic uncertainties.

Ω). These identified tracks are then combined to form invariant mass distributions, and fake combinations are reduced by applying selection criteria on topological variables.

Values for these selection criteria are summarized in Tab. 4 and a detailed description can be found in Ref. [56]. K_S^0 (Λ) candidates compatible with the alternative V^0 hypothesis, obtained by changing the mass assumption for the daughter tracks accordingly, are rejected if they lie within a fiducial window around the nominal Λ (K_S^0) mass. A similar selection is applied for the Ω analysis where candidates are rejected if the corresponding invariant mass, obtained by assuming the pion mass hypothesis for the bachelor track, is compatible within ± 8 MeV/ c^2 with the nominal Ξ mass. A selection is also made on the proper lifetime $c\tau = mL/p$, where m is the particle mass and L is the distance from the primary vertex to the decay vertex; $c\tau$ is required to be less than 20 cm/ c . A further selection is applied on the pointing angle Θ , the angle between the strange hadron's momentum vector and the position vector of its decay point with respect to the primary collision vertex. With requirements of $\cos\Theta > 0.97$ for K_S^0 and $\cos\Theta > 0.995$ for Λ and $\bar{\Lambda}$, about 1% of secondary Λ and $\bar{\Lambda}$ generated in the detector material is removed.

The particle yields are obtained as a function of p_T by extracting the signals from the relevant invariant mass distributions. Examples of the invariant mass peaks at $\sqrt{s} = 13$ TeV are shown in Fig. 4; the distributions of K_S^0 and Λ are very similar to those at $\sqrt{s} = 7$ TeV. The mean (μ) and the width (σ) values of the distributions are found by fitting the distribution with a Gaussian for the signal plus a linear function describing the background. The extracted μ values of the distributions both for V^0 's and cascades are in good agreement with the accepted values [42] and are well reproduced by MC simulations at $\sqrt{s} = 7$ and $\sqrt{s} = 13$ TeV in all measured p_T bins. The widths of the distributions evolve with p_T at $\sqrt{s} = 13$ (7) TeV by about 7 (14) MeV/ c^2 for K_S^0 and 2 (4) MeV/ c^2 for Λ and $\bar{\Lambda}$, which agrees with MC simulations within 15 – 20% at both reported energies. For the V^0 's (cascades) a region containing all the signal (signal region) is defined around the mean within $\pm 6\sigma$ (3σ), while a region to estimate the background (background region) is defined as side-bands from -12σ to -6σ (-12σ to -6σ) and from 6σ to 12σ (6σ to 19σ). Given the flatness of the invariant mass distribution in the background region, the estimate of the background in the signal region is obtained rescaling, by the ratio of the widths in

Table 4: Selection criteria for secondary and bachelor tracks as well as for V^0 and cascade candidates applied in the presented work.

Hadron species	K_S^0	Λ	Ξ	Ω
Secondary track selections				
Pseudorapidity range $ \eta $	< 0.8	< 0.8	< 0.8	< 0.8
DCA _{xy} of V^0 daughter track to primary vertex (cm)	> 0.06	> 0.06	> 0.04	> 0.03
DCA _{xy} of bachelor track to primary vertex (cm)	—	—	> 0.05	> 0.05
TPC dE/dx PID selection (n_σ)	< 5	< 5	< 4	< 4
V^0 selections				
Rapidity range $ y $	< 0.5	< 0.5	—	—
Transverse decay radius (cm)	> 0.5	> 0.5	> 1.4	> 1.4
DCA _{xy} of V^0 to primary vertex (cm)	—	—	> 0.07	> 0.07
DCA between V^0 daughter tracks (n_σ)	< 1	< 1	< 1.5	< 1.5
Cosine of Pointing Angle (for Ξ, Ω)	> 0.97	> 0.995	> 0.97	> 0.97
$ \Delta m $ around nominal Λ mass (MeV/ c^2)	—	—	< 6	< 6
Cascade selections				
Rapidity range $ y $	—	—	< 0.5	< 0.5
Transverse decay radius (cm)	—	—	> 0.8	> 0.6
DCA between V^0 and bachelor track (cm)	—	—	< 1.6	< 1
Cosine of Pointing Angle	—	—	> 0.97	> 0.97
$ \Delta m $ around nominal Ξ mass (MeV/ c^2)	—	—	< 8	> 8

the two regions, the sum of the entries of all the bins in the background region. An alternative method, used to estimate a possible systematic uncertainty, foresees the fit of the invariant mass distribution in the background region and the integral of the extrapolated fit function in the peak region. In both cases, the signal is obtained subtracting the estimated background in the peak region from the integrated counts in the peak region.

The yields for Λ ($\bar{\Lambda}$) are significantly affected by secondary particles coming from the decays of Ξ^- (Ξ^+) and Ξ^0 ($\bar{\Xi}^0$). The feed-down fraction is computed for each p_T bin as the detection efficiency of Λ ($\bar{\Lambda}$) from Ξ decays multiplied by the measured Ξ^+ (Ξ^-) spectra, thereby assuming that the production rates of charged and neutral Ξ are equal. The ratio of secondary Λ to the measured primary yield is about 6–22%, depending on p_T .

For the V^0 and cascade analyses, the main sources of uncertainties are listed in Tab. 5 and Tab. 6, respectively. The values of the selection criteria on the topological variables were varied around their nominal values and the observed deviations for each component were summed in quadrature. Uncertainties related to signal extraction were estimated by varying the values of the width of the signal and background sampling regions with respect to the default one, and adopting an alternative method to estimate the background in the peak region. The procedure resulted in a p_T -dependent uncertainty which ranges from 0.2% to 6.8% for V^0 s and from 0.9% to 2.4% for the cascades.

For the measurement of K_S^0 , Λ and $\bar{\Lambda}$ at $\sqrt{s} = 13$ TeV, contributions from out-of-bunch pileup are removed as stated in Sec. 3.2. The applied correction reaches a maximum value of about 2% for K_S^0 and

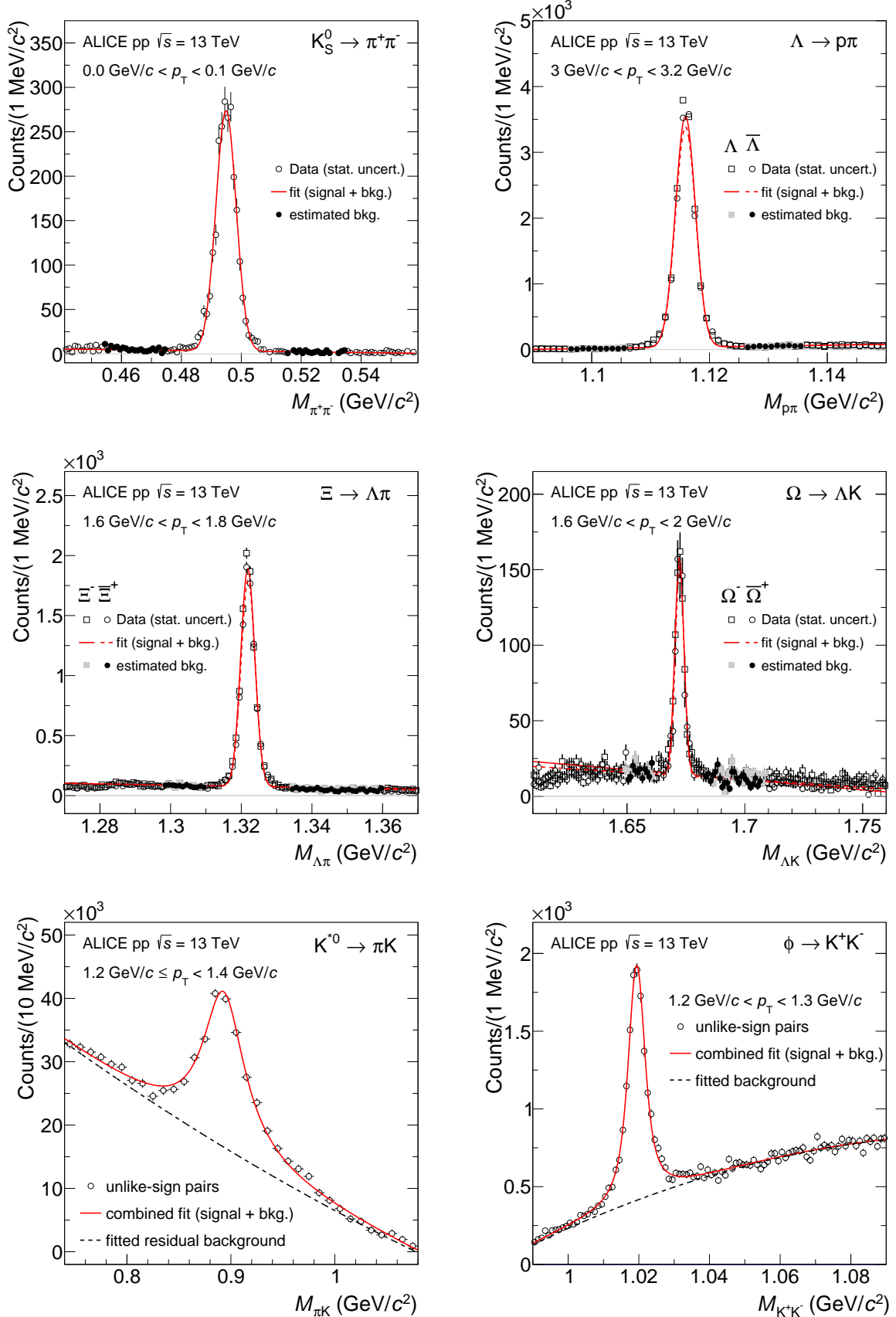


Figure 4: Invariant mass distributions of K_S^0 , Λ and $\bar{\Lambda}$, Ξ^- and Ξ^+ , and Ω^- and $\bar{\Omega}^+$, K^{*0} , and ϕ . See the text for details.

about 3% for $\Lambda + \bar{\Lambda}$ at high p_T . For Ξ^+ and Ξ^- at $\sqrt{s} = 13$ TeV, a p_T -dependent correction factor, taken from Ref. [26] is applied to remove the out-of-bunch pileup contribution; this correction is 0.5% at low p_T and rises to 2.1% at high p_T . Similar correction for Ω^- and $\bar{\Omega}^+$ is negligible, hence not applied. The out-of-bunch pileup contribution is found to be negligible for the measurement of K_S^0 , Λ , and $\bar{\Lambda}$ at $\sqrt{s} = 7$ TeV. A systematic uncertainty to account for any residual effect is 0.3 – 1.1% for the $\Xi^+ + \Xi^-$, 1.2 – 4.6% for $\Lambda + \bar{\Lambda}$, depending on p_T , while it is negligible for K_S^0 .

The V^0 (topological selection) and track selection criteria are varied around their default values, producing up to 9.5% (5.8%) uncertainties in the K_S^0 and Λ yields at $\sqrt{s} = 13$ TeV ($\sqrt{s} = 7$ TeV). The feed-down corrections for Λ and $\bar{\Lambda}$ carry uncertainties associated with the method and the uncertainty of the measured Ξ spectrum. The values are estimated to be around 2% (4 – 6%) for 13 (7) TeV, depending on p_T . The applied selection criteria for PID in the TPC, used for better discrimination between the combinatorial background and the signal for strange baryons, are varied in the range of 4 – $7\sigma_{\text{TPC}}$. For Λ and $\bar{\Lambda}$, this uncertainty is ~ 0.8 –6% at $\sqrt{s} = 7$ and 0.2–3.3% at $\sqrt{s} = 13$ TeV. For Ξ and Ω , it is at most 1% for both collision energies. For K_S^0 the difference was found to be negligible at 13 TeV and at most 2.6% at 7 TeV. The resulting total uncertainties from low to high p_T vary in the ranges 3.6–9.5% for K_S^0 , 6.1–7.8% for Λ , 6.6–3.7% for Ξ , and 6.0–6.7% for Ω .

In the invariant mass distribution (shown in Fig. 4), one could observe for V^0 s and cascades a not perfect fit of the tails close to the peak; the excess of candidates comes from misidentified daughters. The removal of this effect though application of further PID selection criteria would reduce significantly the candidate statistics not improving the signal extraction.

4.4 Reconstruction of resonances

Using analysis techniques similar to those described in Ref. [57], K^{*0} and \bar{K}^{*0} mesons are identified through reconstruction of their decays to charged pions and kaons, while ϕ mesons are identified via their decays to pairs of charged kaons. Primary charged tracks are selected using the standard criteria described in Sec. 3.2. Pion and kaon candidates are identified using their specific energy loss dE/dx measured in the TPC and their velocity β measured with the TOF. The specific energy loss for each pion (kaon) candidate with $p > 0.4$ GeV/c is required to be within $2\sigma_{\text{TPC}}$ of the expected mean value for pions (kaons); a less restrictive selection is applied for lower momenta. In addition, if the charged track is matched to a hit in the TOF, β must be within $3\sigma_{\text{TOF}}$ of the expected mean value. For the analysis of the $K^{*0} + \bar{K}^{*0}$ (ϕ), all kaon candidates are paired with all oppositely charged pion (kaon) candidates from the same event and the pair invariant mass is calculated. The resulting distributions are shown in Fig. 4. The combinatorial background is estimated by calculating the invariant mass distribution of like-charge πK or KK pairs from the same event, by parameterizing the combinatorial background with a simple function (for ϕ only), or by pairing tracks from two different events (the “mixed-event” technique). In order to ensure that the mixed events have similar characteristics, the z positions of their primary vertices are required to be separated by less than 1 cm and their charged particle multiplicities are required to differ by no more than 5 reconstructed tracks. The background-subtracted invariant mass distributions are then fitted with a peak function added to a function that parameterizes the residual background contribution from correlated pairs. The ϕ peak is described with a Voigtian function, the convolution of a Breit–Wigner function and a Gaussian. The mass resolution for the K^{*0} is much smaller than the width of that resonance and a Breit–Wigner function is used to describe the K^{*0} peak. The yield of the $K^{*0} + \bar{K}^{*0}$ (ϕ) is then calculated by integrating the invariant mass distribution within $0.8 < m_{\pi K} < 1.0$ GeV/c² ($1.01 < m_{KK} < 1.03$ GeV/c²), subtracting the integral of the residual background in the same region, and adding the yield from outside the peak region obtained from the peak fit function. The variations in the $K^{*0} + \bar{K}^{*0}$ and ϕ yields due to alternate treatments of the combinatorial background, residual background parameterizations, and peak fitting functions are incorporated into the systematic uncertainties.

Table 5: Summary of the main sources and values of the relative systematic uncertainties (expressed in %) for the K_S^0 and $\Lambda + \bar{\Lambda}$, p_T -differential yields. A single value between two or three columns indicates that no p_T dependence is observed. The values are reported for low, intermediate and high p_T . The abbreviation “negl.” indicates a negligible value.

Hadron species	K_S^0			$\Lambda + \bar{\Lambda}$		
	Collision energy: $\sqrt{s} = 13$ TeV					
p_T (GeV/c)	0.05	4.4	14.25	0.55	4.2	9.0
Feed-down correction	not applicable			1.7	1.8	1.5
Hadronic interaction	negligible			1.7	negl.	negl.
Material budget	4.7	0.5	0.5	6.7	0.8	0.8
Signal-Loss Correction	1.9	0.2	0.4	2.0	0.2	0.2
Track selection	negl.	3.5	9.5	1.0	2.2	2.1
Signal extraction	0.7	0.2	negl.	0.3	1.7	3.8
Proper lifetime	negligible			0.7	1.3	negl.
Competing V^0 rejection	negl.	0.2	negl.	negl.	1.1	2.9
TPC dE/dx	negligible			0.6	0.2	3.3
Topological selection	3.9	0.5	negl.	1.5	1.3	4.0
Out-of-bunch pileup rejection	negligible			1.2	4.6	negl.
Total	6.4	3.6	9.5	7.8	6.1	7.6
Collision energy: $\sqrt{s} = 7$ TeV						
p_T (GeV/c)	0.05	4.4	14.25	0.45	4.2	9.0
Feed-down correction	not applicable			4.0		6.0
Hadronic interaction	negligible				1.0	
Material budget	4.0				4.0	
Signal-Loss Correction	negligible			negligible		
Track selection	1.3	5.8	4.0	1.0	5.6	2.9
Signal extraction	1.8	1.8	5.0	1.4	1.1	6.8
Proper lifetime	0.5	negl.	0.5	2.0	0.8	0.1
Competing V^0 rejection	negl.	0.5	3.2	negl.	2.0	4.8
TPC dE/dx	negl.	2.3	2.6	4.9	0.8	6.0
Topological selection	1.9	1.1	5	1.3	1.2	4.8
Out-of-bunch pileup rejection	negligible			negligible		
Total	5.4	7.7	11.0	8.0	7.6	14.9

Table 6: Summary of the main sources and values of the relative systematic uncertainties (expressed in %) for the $\Xi^- + \bar{\Xi}^+$ and $\Omega^- + \bar{\Omega}^+$ p_T -differential yields. A single value between two or three columns indicates that no p_T dependence is observed. The values are reported for low, intermediate and high p_T . The abbreviation “negl.” indicates a negligible value.

Hadron species	$\Xi^- + \bar{\Xi}^+$			$\Omega^- + \bar{\Omega}^+$		
p_T (GeV/c)	0.7	1.9	6	1.2	2.56	4.3
Feed-down correction	not applicable			not applicable		
Hadronic interaction	1.4	0.1	negl.	0.8	negl.	1.0
Material budget	5.7	1.9	0.6	3.5	1.5	
Signal-Loss correction	0.7	0.2	0.2	0.2	0.1	0.1
Track selection	negl.	0.3	2.9	negl.		
Signal extraction	2.2	0.9	1.2	0.8	1.7	2.4
Competing V^0 rejection	negligible			negl.	3.1	
TPC dE/dx	0.9	negl.	negl.	negligible		
Topological selection	1.7	0.8	1.8	2.5	2.1	3.0
$ y $ cut at low p_T	negligible			3.9	negl.	
Out-of-bunch pileup rejection	0.3	0.5	1.1	not applicable		
Total	6.6	2.4	3.7	6.0	3.1	6.7

Table 7: Summary of the main sources and values of the relative systematic uncertainties (expressed in %) for $K^{*0} + \bar{K}^{*0}$ and ϕ . A single value between two or three columns indicates the mean for all p_T bins, with little p_T dependence. The values are reported for low, intermediate and high p_T . The abbreviation “negl.” indicates a negligible value.

Hadron species	$K^{*0} + \bar{K}^{*0}$			ϕ		
p_T (GeV/c)	0.05	3.0	13.5	0.5	3.0	8.0
Material Budget	3.4	0.5	negl.	2.2	0.7	negl.
Hadronic Interaction	2.8	1.2	negl.	0.5	1.7	negl.
Signal-Loss Correction	1.8	0.3	0.2	1.7	0.5	0.5
Track Selection	8.2	2.2	6.8	4.3	1.6	4.1
Tracking	2.0			2.0		
Signal Extraction	10.6	5.4	10.3	6.0	2.5	4.9
Branching Ratio	negligible			1.0		
Total	17.7	9.9	17.0	8.2	4.2	6.5

The systematic uncertainties in the $K^{*0} + \bar{K}^{*0}$ and ϕ yields include the contributions listed in Tab. 7. The contribution due to variations in the PID, track, and event selection criteria (“Track Selection” in the table) is 2–8% for $K^{*0} + \bar{K}^{*0}$ and 1–5% for ϕ . Variations in the combinatorial background construction, residual background parameterization, peak parameterization, and fit range (“Signal Extraction” in the table) combine to give an uncertainty of 5–11% for $K^{*0} + \bar{K}^{*0}$ and 2–6% for ϕ , depending on p_T . The ITS-TPC matching uncertainty for single particles (pions and kaons) is 2% for all p_T intervals. The uncertainty in the branching ratio is 1% for ϕ and negligible for $K^{*0} + \bar{K}^{*0}$. The total systematic uncertainty for $K^{*0} + \bar{K}^{*0}$ and ϕ is estimated to be about 10 – 18% and 8 – 13%, depending on p_T .

5 Results

For the light-flavor hadrons discussed in this paper, the ratios of yields for particles and antiparticles are around one within the uncertainties, as expected at these collision energies in the midrapidity region. Therefore, all the p_T spectra shown in the following are reported after summing particles and antiparticles, when a distinct antiparticle state exists. Unless explicitly stated, the sums of particles and antiparticles, $\pi^+ + \pi^-$, $K^+ + K^-$, $K^{*0} + \bar{K}^{*0}$, $p + \bar{p}$, $\Lambda + \bar{\Lambda}$, $\Xi^+ + \Xi^-$, and $\Omega^+ + \Omega^-$ are denoted as π^\pm , K^\pm , $K^{*0}(\bar{K}^{*0})$, $p(\bar{p})$, $\Lambda(\bar{\Lambda})$, $\Xi^-(\bar{\Xi}^+)$, $\Omega^-(\bar{\Omega}^+)$ or simply as π , K , K^{*0} , p , Λ , Ξ , and Ω , respectively, unless explicitly written.

The uncertainty related to the overall normalization to inelastic (INEL) events is fully correlated between particle species and is not shown explicitly when plotting the results.

5.1 Transverse momentum distributions, integrated yields, and average transverse momenta

The p_T spectra of light-flavor hadrons measured at midrapidity in inelastic pp collisions at $\sqrt{s} = 7$ and 13 TeV are given in Fig. 5. The p_T spectra of K_S^0 and Λ measured in this paper at $\sqrt{s} = 7$ TeV are shown together with other particle species from previous ALICE measurements at the same center-of-mass energy [25, 23, 58]. For $\sqrt{s} = 7$ TeV INEL pp collisions, the reported p_T distributions of π , K , p [25, 23], K^{*0} , and ϕ [58] are from the updated measurements of ALICE, with extended p_T reach, and, for resonances, additionally with an improved estimate of the systematic uncertainties. For clarity, some of the spectra have been scaled with the factors indicated in the legends.

The p_T distributions are fitted with Lévy–Tsallis functions [59, 60] in order to extrapolate the spectra to the unmeasured p_T regions, i.e. down to zero and up to high p_T , similar to what was done in previous measurements [22, 56, 25, 24, 61]. This procedure allows the p_T -integrated yields dN/dy and the average transverse momenta $\langle p_T \rangle$ to be extracted; these values are given in Tab. 8. The fit function describes well both the low- p_T exponential and high- p_T power-law nature of the p_T distribution, with χ^2/ndf values in the range 0.2 – 2.3. No extrapolation is needed for K_S^0 and K^{*0} , as their yields are measured down to $p_T = 0 \text{ GeV}/c$. The fractions of extrapolated particle yields outside the measured p_T range at low p_T are given in the last column of Tab. 8.

Other fit ranges and other parameterizations (m_T exponential, Boltzmann distribution, Bose–Einstein distribution, Boltzmann–Gibbs blast-wave function [62]) are also used and the resulting variations in the dN/dy and $\langle p_T \rangle$ values are incorporated into the systematic uncertainties. The systematic uncertainties are 4–10% for dN/dy and 1–3% for $\langle p_T \rangle$, similar to those estimated for measurements during Run 1. For the present measurements, systematic uncertainties are dominant. The average yields for all particles species increase with collision energy. Compared to pp collisions at $\sqrt{s} = 7$ TeV [22, 25], the average increase of the $\langle p_T \rangle$ and the yield per inelastic collision for all measured particle species is about 8% and 11%, respectively. This is in agreement with the $\approx 15\%$ increase of the average pseudorapidity density of charged particles produced in $|\eta| < 0.5$ as the collision energy increases from $\sqrt{s} = 7$ TeV to $\sqrt{s} = 13$ TeV [52].

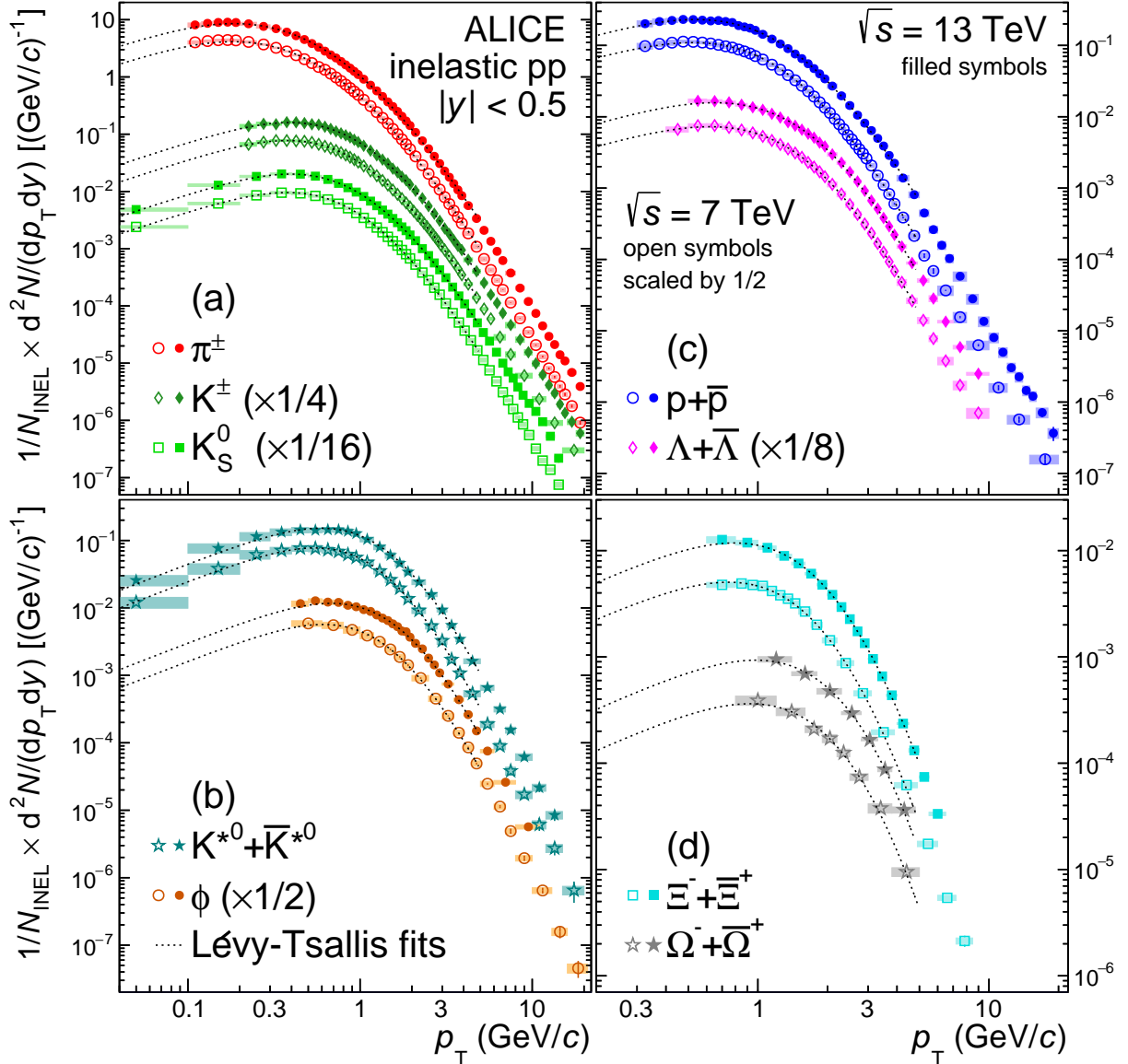


Figure 5: Transverse momentum spectra of light-flavor hadrons measured at midrapidity ($|y| < 0.5$) in inelastic pp collisions at $\sqrt{s} = 13$ TeV (filled symbols) and $\sqrt{s} = 7$ TeV (open symbols, scaled by a factor of 1/2) [23, 25, 58]. Statistical and systematic uncertainties are shown as vertical error bars and boxes, respectively. The data points are fitted using a Lévy–Tsallis function. The normalization uncertainty of $+7.3\% \ (\pm 2.6\%)$ for pp collisions at $\sqrt{s} = 7$ (13) TeV is common to all particle species and is excluded from the plotted uncertainties.

Table 8: Average transverse momentum $\langle p_T \rangle$ and p_T -integrated yield dN/dy values are summarized for the light-flavor hadrons measured in this paper in pp collisions at $\sqrt{s} = 13$ TeV and 7 TeV. The first uncertainty is statistical and the second is systematic (including the low- and high- p_T extrapolation). The uncertainties due to the normalization to the number of inelastic events, which are $^{+7.3\%}_{-3.5\%}$ and $\pm 2.6\%$ for pp collisions at $\sqrt{s} = 7$ and 13 TeV, are not included. The last column represents the fraction of extrapolated yield at low transverse momenta.

Hadron species	dN/dy	$\langle p_T \rangle$ (GeV/c)	Extrapolated fraction (%)
Collision energy: $\sqrt{s} = 13$ TeV			
$\pi^+ + \pi^-$	$4.775 \pm 0.001 \pm 0.243$	$(4.915 \pm 0.001 \pm 0.099) \times 10^{-1}$	8 ± 1
$K^+ + K^-$	$(6.205 \pm 0.004 \pm 0.303) \times 10^{-1}$	$(8.099 \pm 0.007 \pm 0.099) \times 10^{-1}$	9 ± 0.1
K_S^0	$(3.192 \pm 0.004 \pm 0.111) \times 10^{-1}$	$(8.207 \pm 0.008 \pm 0.087) \times 10^{-1}$	negl.
$K^{*0} + \bar{K}^{*0}$	$(2.098 \pm 0.016 \pm 0.200) \times 10^{-1}$	$1.121 \pm 0.005 \pm 0.030$	negl.
$p + \bar{p}$	$(2.750 \pm 0.002 \pm 0.188) \times 10^{-1}$	$(9.659 \pm 0.008 \pm 0.144) \times 10^{-1}$	11 ± 0.5
ϕ	$(3.734 \pm 0.040 \pm 0.213) \times 10^{-2}$	$1.236 \pm 0.009 \pm 0.027$	13 ± 1
$\Lambda + \bar{\Lambda}$	$(1.807 \pm 0.005 \pm 0.102) \times 10^{-1}$	$1.078 \pm 0.002 \pm 0.030$	22 ± 12
$\Xi^- + \bar{\Xi}^+$	$(1.980 \pm 0.012 \pm 0.082) \times 10^{-2}$	$1.296 \pm 0.004 \pm 0.015$	20 ± 4
$\Omega^- + \bar{\Omega}^+$	$(1.846 \pm 0.046 \pm 0.122) \times 10^{-3}$	$1.527 \pm 0.023 \pm 0.027$	34 ± 7
Collision energy: $\sqrt{s} = 7$ TeV			
K_S^0	$(2.802 \pm 0.002 \pm 0.149) \times 10^{-1}$	$(7.731 \pm 0.006 \pm 0.100) \times 10^{-1}$	negl.
$\Lambda + \bar{\Lambda}$	$(1.523 \pm 0.002 \pm 0.110) \times 10^{-1}$	$1.028 \pm 0.001 \pm 0.019$	16 ± 1

6 Discussion

The transverse-momentum spectra reported in Fig. 5 indicate a progressive and significant evolution of the spectral shapes at high p_T with increasing collision energy, which is similar for all particle species under study. This behavior is better visualized in Fig. 6 which shows the corresponding ratios of p_T -spectra at $\sqrt{s} = 13$ TeV to those at $\sqrt{s} = 7$ TeV [23, 25, 58]. The systematic uncertainties at both collision energies are largely uncorrelated and therefore their sum in quadrature is taken as the systematic uncertainty on the ratios. The uncertainty on the ratio due to normalization is $^{+10.8\%}_{-6.3\%}$.

The ratios for all hadron species are above unity, which is consistent with the observed increase in the pseudorapidity density of inclusive charged particles with increasing collision energy [52]. Furthermore, all the ratios exhibit a clear increase as a function of p_T , indicating that hard processes become dominant in the production of high- p_T particles. The p_T dependence demonstrates that the spectral shapes are significantly harder at $\sqrt{s} = 13$ TeV than at $\sqrt{s} = 7$ TeV, and a universal shape — independent of p_T within uncertainties — can be observed for most species (excluding Ξ and Ω) in the soft regime, $p_T \lesssim 1 \text{ GeV}/c$. There is a hint that the ratio for $p(\bar{p})$ may be enhanced above the one for π^\pm in the p_T region $\sim 3 - 6 \text{ GeV}/c$, although the enhancement is barely significant given the uncertainties. Such an enhancement would be consistent with the appearance of the baryon anomaly, an increased baryon-to-meson production ratio at intermediate transverse momenta ($2 \text{ GeV}/c \lesssim p_T \lesssim 10 \text{ GeV}/c$), observed in previous ALICE measurements of light-flavor hadron production [7, 63, 51, 23, 64]. It is worth noting that the hardening of the p_T spectra with increasing collision energy has been reported in our earlier work for inclusive charged particles [52], although with different event selection criteria. There, a requirement of at least one charged particle with $p_T > 0 \text{ GeV}/c$ in $|\eta| < 1$ was imposed, selecting events corresponding to 75% of the total inelastic cross section. In Ref. [52], the observed trend was found to be well captured by the PYTHIA and EPOS-LHC MC generators. In Sec. 6.5 the ratios of p_T -spectra of light-flavor hadrons at $\sqrt{s} = 13$ TeV to those at $\sqrt{s} = 7$ TeV are compared to results from these common event generators.

6.1 Scaling properties of hadron production

Two kinds of universal scaling of identified particle production have been observed in high energy pp collisions: transverse mass (m_T) scaling, which was originally seen in the lower p_T region of hadron spectra, and x_T scaling [65, 66, 67, 16, 68], observed in the higher p_T region. New studies of the m_T and x_T scaling properties of light-flavor hadrons in pp collisions at $\sqrt{s} = 7$ and 13 TeV are discussed below.

6.1.1 Transverse mass (m_T) scaling

At ISR energies [69, 70] it has been observed that hadron m_T spectra in pp collisions seem to follow an approximately universal curve after scaling with arbitrary normalization factors, an effect known as m_T scaling. The STAR and PHENIX collaborations observed the breaking of m_T -scaling in pp collisions at $\sqrt{s} = 200 \text{ GeV}$ [19, 71], where a clear separation between baryon and meson spectra was observed for $m_T \geq 2 \text{ GeV}/c^2$. In pp collisions at $\sqrt{s} = 200 \text{ GeV}$, the separation between the baryon and meson spectra seems to increase over the measured m_T range. We, the ALICE collaboration, recently reported a similar breaking in pp collisions at $\sqrt{s} = 8 \text{ TeV}$ [10]. The measurements in this paper allow this study to be extended to higher m_T and to the highest LHC energies.

The charged kaon and (anti)proton m_T spectra are fitted separately with a modified Hagedorn function of the form $A \times (e^{-am_T} + m_T/b)^{-n}$ [20]. The meson m_T spectra are then scaled by multiplicative factors so that their integrals over the measured m_T ranges (or $m_T > 2 \text{ GeV}/c^2$ for the pions) match the integral of the kaon fit function. Similarly, the baryon m_T spectra are scaled so that their integrals match the integral of the proton fit function over their measured m_T ranges. The baryon spectra are further scaled so that all of the m_T spectra have the same value at $m_T = 1 \text{ GeV}/c^2$. Figure 7 shows the result of this study for pp

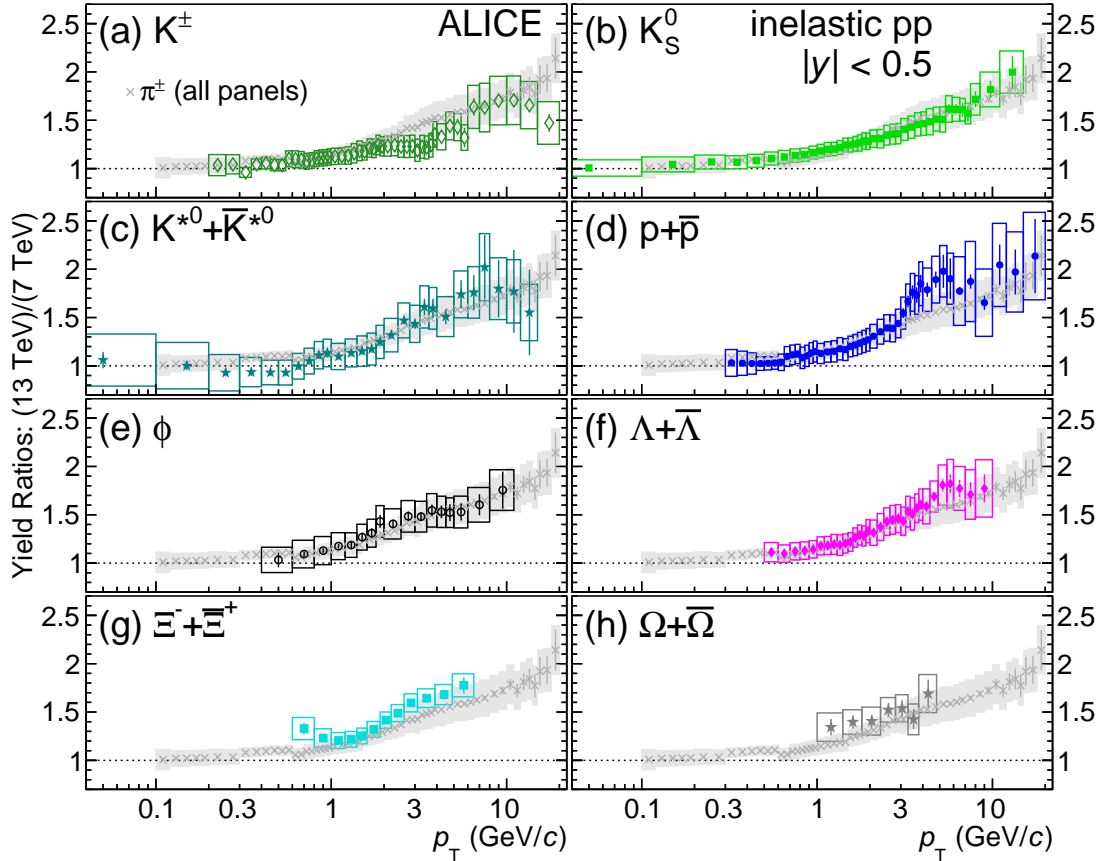


Figure 6: Ratios of the transverse-momentum spectra of light-flavor hadrons in inelastic pp collisions at $\sqrt{s} = 13$ TeV to those for $\sqrt{s} = 7$ TeV [23, 25, 58]. The ratio for π^\pm is shown in each panel with grey crosses and boxes. Statistical and systematic uncertainties are shown as vertical bars and boxes, respectively. The normalization uncertainty ($^{+10.8\%}_{-6.3\%}$) is excluded from the plotted uncertainties.

collisions at $\sqrt{s} = 7$ TeV [23, 25, 58] and 13 TeV, with the lower panels showing the ratios of the various scaled m_T spectra to the K^\pm fit function.

The pion m_T spectra deviate from the trend followed by the other mesons for $m_T \lesssim 2 \text{ GeV}/c^2$, which is likely due to feed-down from resonance decays [72]. The measured primary π^\pm yield contains significant contribution mostly from ρ and ω decays, which, according to a recent study [21], affects the low- p_T ($\lesssim 1 \text{ GeV}/c$) part of the spectrum with increasing importance towards higher collision energies. This is the reason why the K^\pm m_T spectrum is used as the reference for the other mesons. A clear difference in the slope is observed between the baryon and meson spectra for $m_T \gtrsim 2 \text{ GeV}/c^2$. The separation between the meson and baryon m_T spectra may be a reflection of the fact that, according to the Lund model of hadronization, meson formation via the fragmentation of strings requires the break up only a (quark, anti-quark) pair, while baryon(-antibaryon) can be formed by the (diquark, anti-diquark) break up of the string [73, 74]. The separation between the (anti)proton and meson m_T spectra becomes approximately constant for $m_T > 10 \text{ GeV}/c^2$.

The breaking of m_T scaling for pions at low m_T as shown in Fig. 7 serves a motivation to quantify the effect for different mesons. Following Refs. [21, 75], instead of using the m_T spectra, the scaling law can be better studied practically as a function of p_T , (note that the invariant yields are equal in terms of these variables). This requires changing the functional form of the invariant yield parameterization through the substitution $p_T \rightarrow \sqrt{m_T^2 - m^2}$, where m is the particle mass. In doing so, the p_T -differential invariant yield $Y_{s'}$ of a particle species s' can be obtained by scaling the parameterization of the yield Y_s^{ref} of

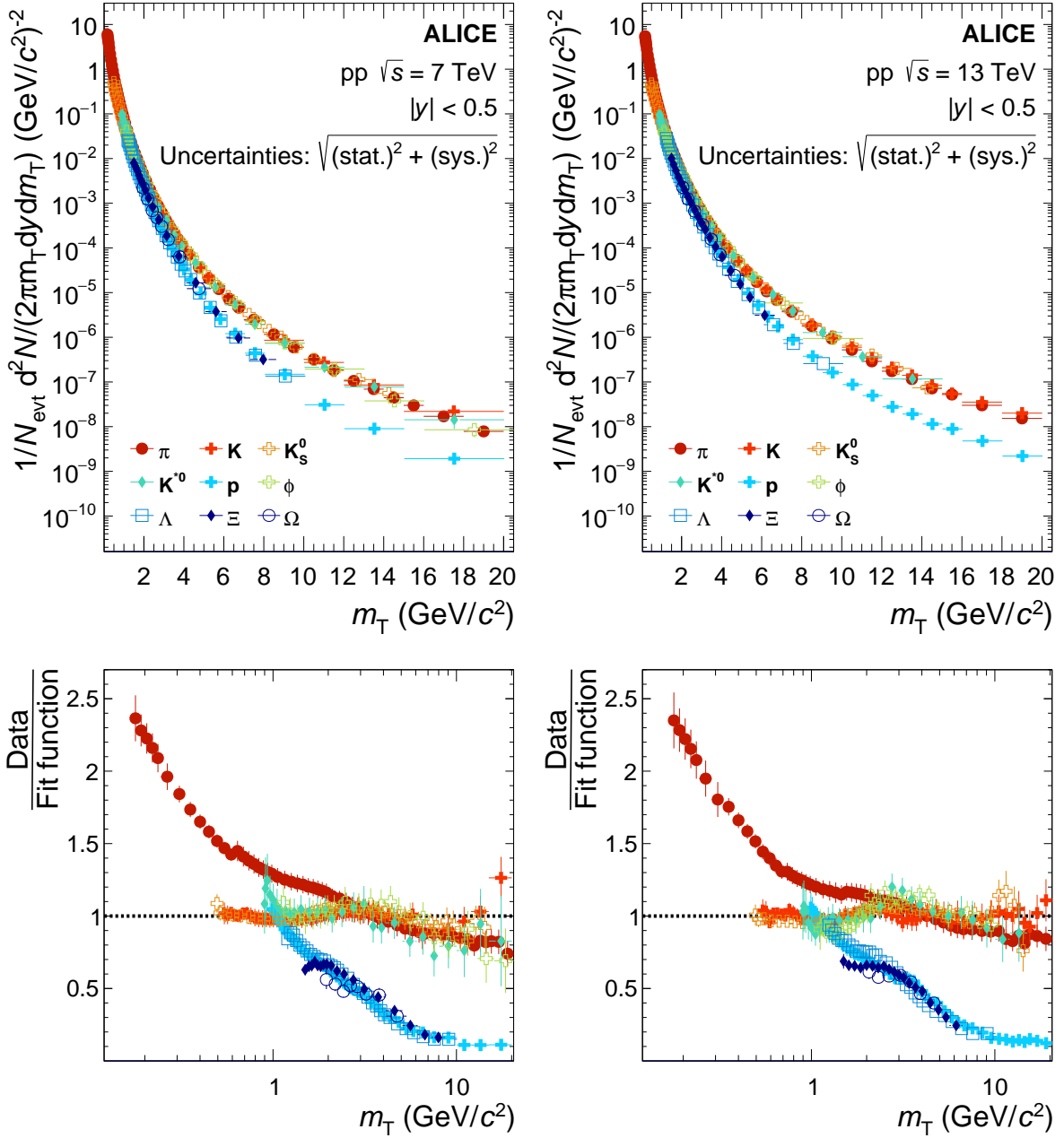


Figure 7: Upper panels: Scaled m_T spectra for identified particles in pp collisions at $\sqrt{s} = 7$ TeV (left) and 13 TeV (right). Lower panels: Ratios of the scaled m_T spectra to the K^\pm fit functions. The reference data for pp at $\sqrt{s} = 7$ TeV are from Refs. [23, 25, 58]

reference particle species s . When both spectra are evaluated at the same transverse mass, $(p_{T,s}^2 + m_s^2) = (p_{T,s'}^2 + m_{s'}^2)$, the yield for species s' is $Y_{s'}(p_{T,s'}) = c \times Y_s^{\text{ref}}(\sqrt{p_{T,s'}^2 + m_{s'}^2 - m_s^2})$. Here, c is a constant offset between the yields for species s and s' , determined in the p_T region where the spectral shapes for the two species are the same (i.e. at high p_T).

Charged pions are used as the reference species to test the m_T scaling of the K^\pm/π^\pm , K_S^0/π^\pm , K^{*0}/π^\pm and ϕ/π^\pm particle ratios. The reference p_T spectrum of π^\pm is parameterized with a Lévy–Tsallis function, which is also used for the extraction of the p_T -integrated yields and is found to describe the data within 15% over its entire p_T range. The m_T scaling relation is then applied to the parametrized pion yield. The appropriate offset parameter c is determined by fitting the measured particle ratios separately in the high- p_T region where they saturate. The measured K^\pm , K_S^0 , and K^{*0} (ϕ) yield in pp collisions at $\sqrt{s} = 13$ (7) TeV are fitted with a constant linear function in the range $p_T > 6 \text{ GeV}/c$ ($p_T > 4 \text{ GeV}/c$) with statistical and systematic uncertainties summed in quadrature. The resulting c values for the various particle ratios are given in the legends of Fig. 8 and are shown as shaded bands in the p_T region from which they are extracted. The reported widths of the bands correspond to the statistical uncertainties on c obtained from the fits.

Along with the measured particle yield ratios, Fig. 8 shows the ratios of the m_T -scaled parameterizations to the reference parametrization (solid blue lines) for the particle species in question. A significant deviation between the parameterized curves and the measured data is observed in the low-to-mid p_T region ($p_T \lesssim 5 – 6 \text{ GeV}/c$) for the K^\pm/π^\pm and K_S^0/π^\pm ratios, which indicates the breaking of empirical m_T scaling. In contrast, the m_T -scaling predictions for the K^{*0}/π^\pm and ϕ/π^\pm ratios are notably closer to the measurements. In order to quantify the level of the scale breaking, the double ratios between the measured yield ratios and those based on the m_T -scaling relation are evaluated. The double ratio values for p_T below the threshold of $6 \text{ GeV}/c$ (i.e., below the region used for the determination of the offset parameter c) decrease towards lower p_T , deviating beyond 16% for $p_T \lesssim 2 \text{ GeV}/c$. The significance of the deviation from the m_T scaling hypothesis is 4.7σ at $p_T = 1 \text{ GeV}/c$, far from the threshold (note that adjacent p_T bins have fully uncorrelated uncertainties). This further confirms the breaking of the empirical m_T scaling relation for the quoted p_T region.

6.1.2 x_T scaling

The validity of empirical x_T scaling is tested using the $\sqrt{s} = 13$ TeV pp measurements reported here and those obtained at $\sqrt{s} = 2.76$ TeV [7, 61] and $\sqrt{s} = 7$ TeV [23, 58]. Due to the lack of a complete set of measurements of hadron yields at high p_T at these three collision energies, only π^\pm , K^\pm , K^{*0} , and $p(\bar{p})$ are used.

The invariant cross sections are determined from the measured invariant yields as $E d^3\sigma/d^3p = \sigma_{\text{inel}} \times E d^3N/d^3p$, where σ_{inel} is the inelastic cross section in pp collisions at $\sqrt{s} = 13$ TeV [46]. The logarithm of the ratio of the invariant cross sections at two different collision energies, scaled by the logarithm of the ratio of the two collision energy is calculated. This quantity, denoted as n in the following, depends on x_T and \sqrt{s} [76]. It increases with x_T in the low x_T region, where particle production is dominated by soft processes, and appears to saturate in the high x_T region. Each $n(x_T, \sqrt{s})$ distribution is fitted with a constant in the range $2 \times 10^{-3} \leq x_T \leq 6 \times 10^{-3}$ to obtain the respective n values for different energy combinations; these are then averaged to obtain the mean value $\langle n \rangle$ for each particle species. The x_T spectra for different particle species are scaled by $(\sqrt{s}/\text{GeV})^{\langle n \rangle}$. Within the quoted x_T range, the best scaling is achieved with the exponents $\langle n \rangle = 5.04 \pm 0.02$ for π^\pm , $\langle n \rangle = 5.02^{+0.21}_{-0.25}$ for K^\pm , $\langle n \rangle = 5.83^{+0.13}_{-0.21}$ for $p(\bar{p})$, and $\langle n \rangle = 5.23 \pm 0.15$ for K^{*0} . The uncertainties on the $\langle n \rangle$ values are the maximum observed deviations from the mean. The scaling exponents for the meson spectra are found to be consistent within systematic uncertainties, indicating that ratios of meson spectra at high p_T are constant and attain similar values for all beam energies. Figure 9 shows the x_T -scaled spectra for π^\pm , K^\pm , $p(\bar{p})$, and K^{*0} at collision energies of $\sqrt{s} = 2.76$ TeV [7, 61], 7 TeV [23, 58] and 13 TeV.

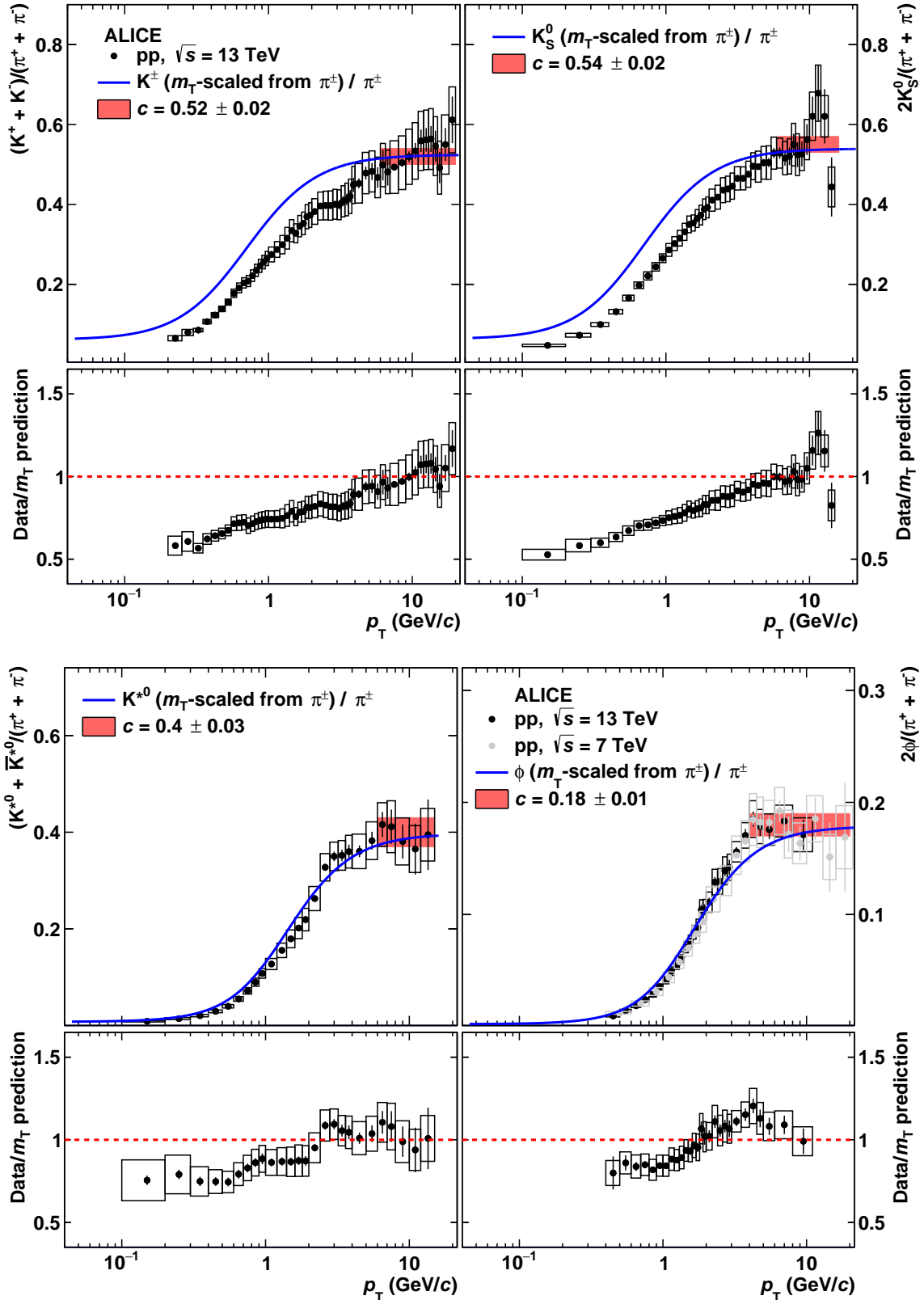


Figure 8: Particle ratios K^\pm/π^\pm , K_S^0/π^\pm (top) and K^{*0}/π^\pm , ϕ/π^\pm (bottom) as a function of p_T measured in pp collisions at $\sqrt{s} = 13$ TeV. The measured ratio is reported together with that obtained from transverse mass (m_T) scaling of charged pions shown as a solid line. The shaded red band indicates the constant fit, in the p_T region where it was performed, which is used to determine the constant offset parameter c . See the text for details. The ϕ spectrum in pp at $\sqrt{s} = 7$ TeV is from Ref. [58]

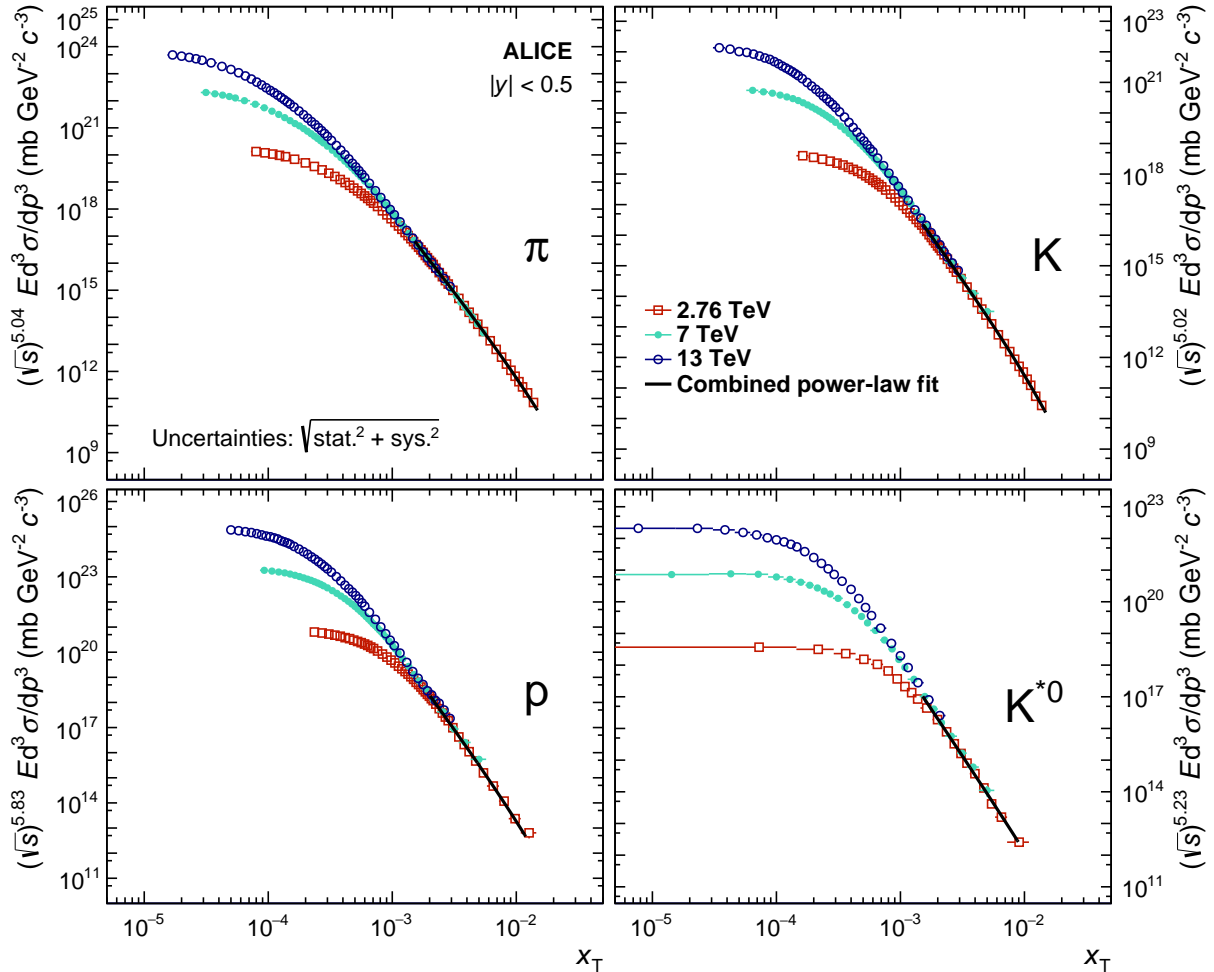


Figure 9: Scaled invariant yields of π^\pm , K^\pm , $p(\bar{p})$, and K^{*0} as a function of $x_T = 2p_T/\sqrt{s}$ at different collision energies of $\sqrt{s} = 2.76$ TeV [7, 61], $\sqrt{s} = 7$ TeV [23, 58], and $\sqrt{s} = 13$ TeV. The solid line represents a combined power-law fit in the high- x_T region where the distributions show a scaling behavior.

These results suggest that identified particle yields at LHC energies follow x_T scaling above $x_T \sim 10^{-3}$. The value of the parameter n is found to be lower at LHC energies compared to RHIC energies [14], which is attributed to the increasing importance of hard scattering processes at higher \sqrt{s} , as suggested by Fig. 6. It is also interesting to note that the exponent n takes on larger values for baryons than for mesons in the investigated x_T range. On the one hand, this is connected to the decrease of the p/π ratio with increasing p_T (see Fig. 13), as opposed to the constant behavior of the K/π and K^{*0}/π ratios (see Fig. 8), which suggests that meson spectra are harder than baryon spectra in the corresponding p_T range. On the other hand, as discussed in Ref. [16], the NLO pQCD predictions including higher-twist processes, i.e. in which the detected hadron can be exclusively produced in the hard subprocess reaction, there is evidence for the larger value of the exponent for baryons than for mesons. This is in contrast to the observations based on the leading-twist processes, where the exponent n has only a weak dependence on hadron species.

The quality of the scaling behavior is verified by combined fitting the differential cross sections with a power-law function of the form $a \times x_T^b \times (1 + x_T)^c$. Here, a , b , and c are free parameters and the region below $x_T = 1.5 \times 10^{-3}$ ($x_T = 2 \times 10^{-3}$ for protons) is excluded to avoid the dominant contribution from soft particle production, which does not follow x_T scaling. The fits are of good quality with χ^2/ndf values in the range 0.4 – 1.5. In spite of the naive assumption of a power law function and the expected non-scaling behaviors discussed in Ref. [77], the measurements agree with the global power law fits

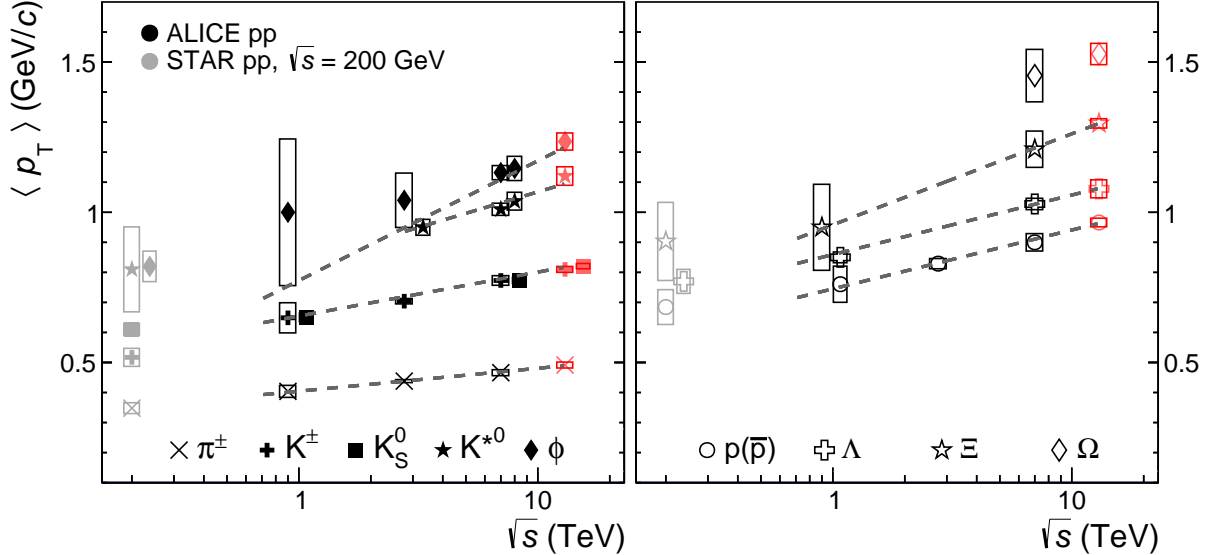


Figure 10: Average transverse momentum $\langle p_T \rangle$ as a function of the center-of-mass energy. Open boxes indicate the statistical and systematic uncertainties (when available) summed in quadrature. Results from ALICE [49, 7, 22, 56, 61, 25, 24, 78] are compared with those from STAR measured at $\sqrt{s} = 200$ GeV [79]. Some data points are slightly offset from their true energy for better visibility. Dashed curves show linear fits in $\ln s$. Note that the data points of K_S^0 are not fitted due to their very similar values of $\langle p_T \rangle$ to those of charged kaons.

within the region of overlap ($2 \times 10^{-3} \lesssim x_T \lesssim 6 \times 10^{-3}$) within roughly 40%, depending on particle species. The measurements from ALICE performed at $\sqrt{s} = 13$ TeV are consistent over the accessible x_T range ($2 \times 10^{-3} \leq x_T \leq 6 \times 10^{-3}$) with empirical x_T scaling and with measurements from pp collisions at $\sqrt{s} = 2.76$ and 7 TeV.

6.2 Excitation functions

Figure 10 compiles the excitation functions of the average transverse momenta $\langle p_T \rangle$ for light-flavor hadrons in inelastic pp collisions; the focus is on the LHC energy regime, but some RHIC results are also shown. As discussed in Ref. [80], the measurement of $\langle p_T \rangle$ as a function of the collision energy is particularly useful in probing the saturation scale of the gluons inside the proton.

Results at midrapidity are presented from $\sqrt{s} = 200$ GeV up to the top LHC energy $\sqrt{s} = 13$ TeV, spanning nearly two orders of magnitude in center-of-mass energy. The average p_T increases with \sqrt{s} ; it rises steeply for heavier particles, as seen in our earlier measurements at lower collision energies [22, 25, 24, 78]. The moderate increase of $\langle p_T \rangle$ with increasing \sqrt{s} is attributed to the increasing importance of hard processes for higher collision energies. For single- and multi-strange hadrons, this observation is equivalent to the hardening of $\langle p_T \rangle$ as the collision energy increases from $\sqrt{s} = 7$ to 13 TeV for event classes with a similar $\langle dN_{\text{ch}}/d\eta \rangle$, as reported in Ref. [26].

It is worth noting that the proton and Λ have different $\langle p_T \rangle$ values than the K^{*0} and ϕ , despite the similar masses of these particles. In particular, regardless of the considered \sqrt{s} , the average transverse momenta are greater for those resonances than for protons or Λ , with the ϕ having the largest value. This clearly indicates a violation of mass ordering among these particles. It is noteworthy that in our measurements at $\sqrt{s} = 7$ TeV as a function of charged-particle multiplicity, the difference in $\langle p_T \rangle$ between $p(\bar{p})$ and K^{*0} (and ϕ) increases with multiplicity [51].

It is of particular importance to study the p_T -integrated particle ratios as a function of collision energy, which might provide more information on hadron production mechanisms and their dependence on the

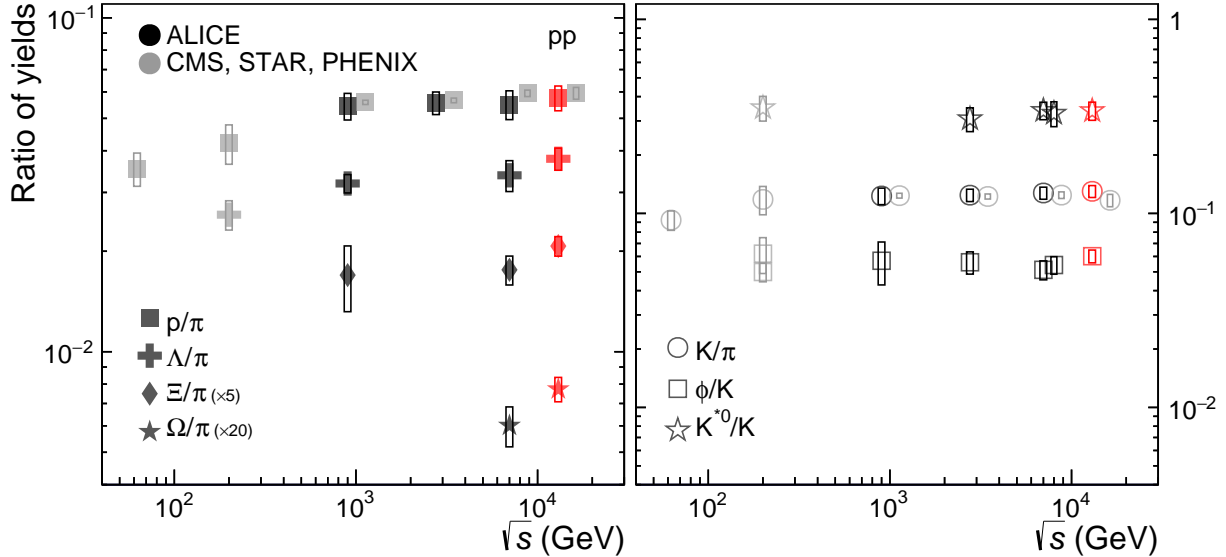


Figure 11: Ratio of particle yields to π^\pm and K^\pm as a function of the collision energy \sqrt{s} (GeV). Results from ALICE [49, 7, 22, 56, 61, 25, 24, 78] are compared with those from CMS [81] at the same energies, and with those from STAR [79, 82, 83] at $\sqrt{s} = 200$ GeV and PHENIX [84, 71] at $\sqrt{s} = 62.4$ GeV obtained at BNL RHIC. The CMS data points are slightly shifted horizontally for clarity. Open boxes represent statistical and systematic uncertainties summed in quadrature.

collision energy or charged particle multiplicity. Given the observation of an increase in (multi-)strange hadron production as a function of multiplicity in pp collisions at $\sqrt{s} = 7$ TeV [85], an increase in these yields with collision energy would also be expected. Figure 11 shows the ratios of particle yields to the yields of pions and kaons as a function of the collision energy; results from ALICE are compared with those from CMS [81] and with STAR [79, 82, 83] and PHENIX [84, 71] results from RHIC measured at $\sqrt{s} = 200$ and 62.4 GeV. All the ratios except Ω/π and Ξ/π appear to saturate in the LHC energy regime. For the Ω/π and Ξ/π ratios, the relative increases are $\sim 29\%$ and $\sim 18\%$, respectively; these are larger than the $\sim 12\%$ increase of the Λ/π ratio, indicating that the strangeness content may control the magnitude of the increase in the yield ratios as the energy changes from $\sqrt{s} = 7$ to 13 TeV. This might also suggest the onset of strangeness enhancement in the new reported energy regime. This enhancement would be more pronounced for Ω/π since Ω has a higher strangeness content. The evolution of this ratio from $\sqrt{s} = 7$ to 13 TeV fits into the trend seen for the absolute yield of Ω baryons as a function of charged-particle multiplicity for similar multiplicity values, in the vicinity respectively of $\sqrt{s} = 7$ TeV and $\sqrt{s} = 13$ TeV with $\langle dN_{ch}/d\eta \rangle = 4.60^{+0.34}_{-0.17}$ [86] and $\langle dN_{ch}/d\eta \rangle = 5.31 \pm 0.18$, as reported in Ref. [26].

The ratios of the ϕ and K^{*0} yields to those of charged kaons (ϕ/K and K^{*0}/K) do not exhibit any dependence on the collision energy. It is worth noting that there may be a decrease in the K^{*0}/K ratio in high-multiplicity pp collisions at $\sqrt{s} = 7$ TeV [51]. In nuclear collisions, such a modification of resonance yields is often described as a consequence of scattering processes during the hadron gas phase of the collision system evolution.

6.3 Mass and baryon number effects on $\langle p_T \rangle$

The average transverse momenta $\langle p_T \rangle$ as a function of the particle mass are reported in the left panel of Fig. 12 for all light-flavor hadrons under study. The $\sqrt{s} = 13$ TeV pp results are compared to our earlier measurements reported at lower collision energies [49, 22, 61, 56, 25], and to those measured at $\sqrt{s} = 200$ GeV by the PHENIX Collaboration at RHIC [71]. At $\sqrt{s} = 13$ TeV, two different linear trends can be observed for mesons and baryons separately, reflecting the violation of mass ordering in $\langle p_T \rangle$.

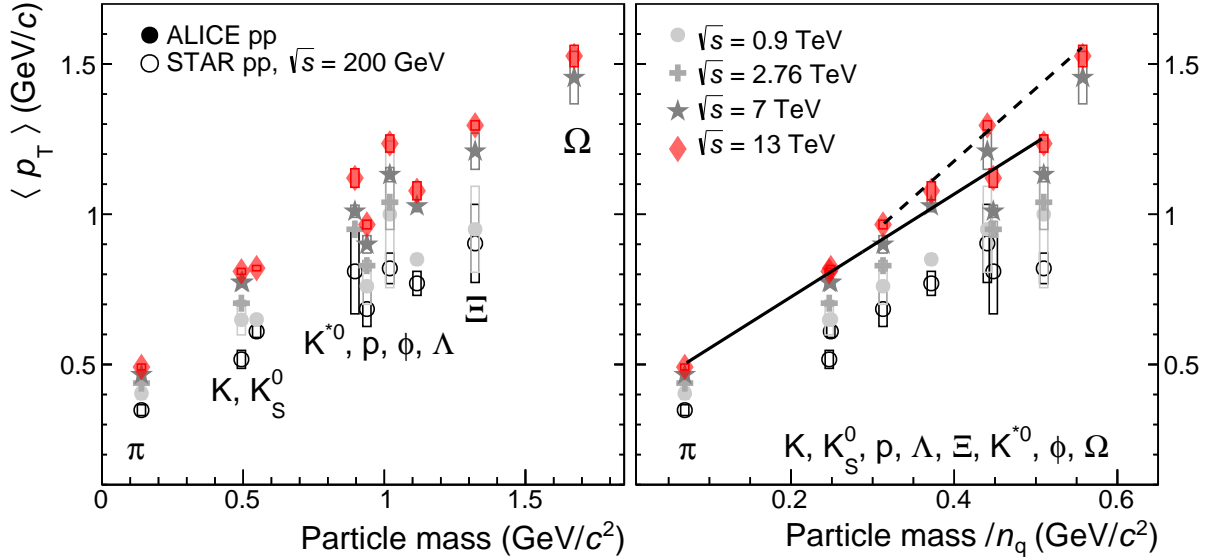


Figure 12: Average transverse momenta of light-flavor hadrons as a function of hadron mass (left) and as a function of hadron mass normalized to the number of constituent quarks (right) for different collision energies (\sqrt{s}). Results reported from ALICE [49, 7, 22, 56, 61, 25, 24] are compared with those measured by STAR at RHIC at $\sqrt{s} = 200$ GeV [79, 82, 83]. Uncertainties that are not visible are smaller than the size of the symbol. Solid and dashed lines are drawn as visual aids and represent separate linear fits to meson and baryon data at $\sqrt{s} = 13$ TeV. The data points for K_S^0 are slightly shifted horizontally for clarity.

The observation of scale breaking between mesons and baryons as a function of the transverse mass, as discussed in Sec. 6.1.1, might lead to a violation of mass ordering in the average transverse momenta of the produced particles. For particles with similar masses (like K^{*0} , p , ϕ , and Λ), the meson spectra will be harder and the $\langle p_T \rangle$ values greater in comparison to the baryons. Furthermore, the softer pion m_T spectra could lead to a deviation of the pion $\langle p_T \rangle$ values from the trend observed for the other mesons.

For $\sqrt{s} < 1$ TeV all the considered hadrons appear to exhibit scaling of $\langle p_T \rangle$ with the reduced hadron mass m/n_q , i.e. the mass normalized by the number of constituent quarks n_q . This is observed in pp collisions at $\sqrt{s} = 900$ GeV at ALICE and is shown in the right panel of Fig. 12. Reference [87] suggests that such scaling holds even for multi-strange baryons (Ξ , Ω) when the average pseudorapidity density of charged particles measured at mid-pseudorapidity is small ($\langle dN_{\text{ch}}/d\eta \rangle = 3.81 \pm 0.01$ (stat.) ± 0.07 (syst.) [88]). At higher collision energies, the scaling behavior is obviously broken. Two separate trends are observed at $\sqrt{s} = 13$ TeV: one for mesons (slope 1.71 ± 0.06) and one for baryons (slope 2.42 ± 0.15).

6.4 Yield ratios

The ratios of hadron yields are investigated as a function of transverse momentum. This allows the p_T spectra of different particle species, characterized by their unique mass and quark content, to be compared. Additionally, measurements at different \sqrt{s} are included, which helps to quantify any change in spectral shapes with \sqrt{s} . The uncertainties related to normalization cancel in these ratios. Figure 13 shows the p/π , Λ/K_S^0 (left panel), Ξ/ϕ , and Ω/ϕ (right panel) baryon-to-meson ratios as a function of p_T at $\sqrt{s} = 7$ [23, 64, 25] (open symbols) and $\sqrt{s} = 13$ TeV (full symbols). The left panel includes particle ratios with baryons containing zero (p/π) and one (Λ/K_S^0) strange valence quark, whereas the right panel collects ratios for hadrons with two (Ξ/ϕ) and three (Ω/ϕ) strange quarks. The Ω/ϕ ratio compares hadrons that consist entirely of strange valence (anti)quarks: three for Ω in and two for ϕ .

At low p_T , all of the ratios increase with p_T as expected from the higher $\langle p_T \rangle$ observed for higher mass particles. In this p_T regime, all of the ratios at $\sqrt{s} = 13$ TeV show good agreement with those at

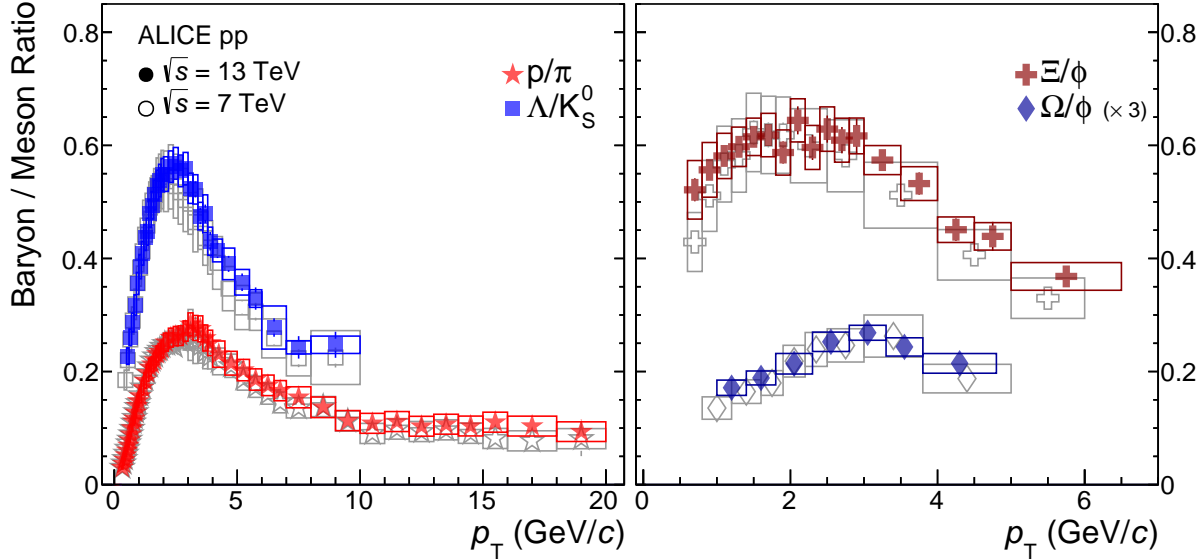


Figure 13: Baryon-to-meson ratios as a function of transverse momentum (p_T) measured in pp collisions at $\sqrt{s} = 13$ (full symbols) and 7 TeV [23, 25] (open symbols). Note the different scale of the horizontal axis in the right panel.

$\sqrt{s} = 7$ TeV within their systematic uncertainties, suggesting that the collision energy has no observable effect on the magnitude or shape of these yield ratios. This observation remains valid in the higher p_T region. Within the systematic uncertainties the p/π , Λ/K_S^0 , Ξ/ϕ , and Ω/ϕ ratios are consistent for the two collision energies. It is noteworthy that the p/π ratio at $\sqrt{s} = 13$ TeV has a hint of enhancement at intermediate p_T with respect to that at $\sqrt{s} = 7$ TeV, however this is barely significant given the quoted uncertainties. From $p_T > 10$ GeV/c onward, the p/π ratio becomes fairly constant for both collision energies.

6.5 Comparison to theoretical models

The high-precision measurements of the p_T spectra reported in this paper are crucial inputs for the further tuning of Monte Carlo event generators and to improve the understanding of particle production mechanisms at the investigated collision energies. The measurements of the light-flavor hadron species presented above are compared with Monte Carlo model predictions based on general-purpose event generators: PYTHIA 6, PYTHIA 8, and EPOS-LHC.

The PYTHIA MC model contains a rigorous description of hard scatterings through pQCD, combined with phenomenological models for semi-hard/soft processes. The Perugia-2011 tune [89] for PYTHIA 6 and the Monash 2013 tune [90] for PYTHIA 8, which have different sets of parameters, are used. The PYTHIA 8 model uses an updated parameter set for Lund hadronization for light (and heavy) quarks. The widely-used Monash 2013 tune has an improved description of diffractive processes with respect to PYTHIA 6. Both sets of parameters have been obtained from recent (2011 and 2013) analyses of minimum bias, underlying event, and/or Drell–Yan measurements in pp collisions at $\sqrt{s} = 7$ TeV; the Monash 2013 tune was optimized to describe early data collected by the LHC experiments as well as lower energy data. Moreover, both versions of the model have strong final-state parton interactions implemented through different color reconnection models [91, 92]. As a consequence of the different energy evolution of the cutoff for multiple parton interactions, the Monash tune has larger multiple parton interaction activity at a given collision energy than the Perugia tune.

Conversely, the EPOS-LHC event generator (used with the CRMC package, version 1.5.4) invokes the Gribov’s Reggeon Field Theory [93] for multiple scatterings; this formalism features collective hadronization with the core-corona mechanism [94]. After multiple scattering, the final-state partonic

system consists mainly of longitudinal flux tubes that fragment into string segments. If the energy density from string segments is high enough, they fuse into the so-called “core” region, which then evolves hydrodynamically and eventually hadronizes to form the bulk part of the system. On the other hand, in the low-density region the strings expand and eventually break via the production of quark-antiquark pairs, which hadronize using the unmodified string fragmentation and form the “corona” region. The EPOS-LHC model uses recent data available from LHC, which helps in reproducing minimum bias results with transverse momenta up to a few GeV/c .

Figure 14 shows the ratios of p_T spectra extracted from the PYTHIA 8, PYTHIA 6, and EPOS-LHC models to the spectra measured at $\sqrt{s} = 7$ and 13 TeV; the models give similar descriptions of the data at both energies. For the comparison of the measured data to the MC generators, the total fractional uncertainties of the data are shown, i.e. the statistical and systematic uncertainties of the measurement have been summed in quadrature. Both PYTHIA versions can generally describe the shapes of particle p_T spectra with reasonable accuracy at intermediate p_T ($2 \text{ GeV}/c \lesssim p_T \lesssim 10 \text{ GeV}/c$), but generally give softer p_T spectra than observed at low p_T ($\lesssim 2 \text{ GeV}/c$), although pions show the opposite trend, with a harder spectrum. This low- p_T behavior is due to the fact that the MC generators are known to have difficulties at describing diffractive processes that play a role at very low p_T [44]. In contrast, at high p_T PYTHIA predicts harder spectra.

For the most abundant pions and charged kaons, the spectral shapes above $\sim 1 \text{ GeV}/c$ are described significantly better by PYTHIA 8 than PYTHIA 6. For both K^\pm and K_S^0 , the model-to-measured ratios for both PYTHIA versions are qualitatively similar, although PYTHIA 8 provides a better agreement with the data at mid-to-high p_T than PYTHIA 6. These PYTHIA tunes describe the (anti)proton p_T spectra best for $0.8 < p_T < 4 \text{ GeV}/c$. For single-strange (Λ) and multi-strange (Ξ, Ω) baryons, both of the PYTHIA models underestimate the amount of produced particles in almost the entire p_T range. A similar discrepancy is observed for the case of PYTHIA 6 with the Perugia 2011 tune at $\sqrt{s} = 7 \text{ TeV}$ [25] and with older tunes (D6T, ATLAS-CSC, Perugia 0) for the Ξ as reported for $\sqrt{s} = 900 \text{ GeV}$ in Ref. [56]. It is worth noting that a discrepancy is also observed when the yields of Λ, Ξ , and Ω measured as a function of the charged-particle multiplicity [26] are compared to results from PYTHIA and EPOS-LHC. In all cases, the observed deviation becomes larger for hadrons with higher strange valence quark content. In Fig. 14, the model underestimates the measured Ξ (Ω) yields by a factor of two (four), although the discrepancy weakens for the Ξ towards higher p_T values. For the ϕ meson (with zero net strangeness content), PYTHIA predicts yields within $10 - 20\%$ for $p_T \sim 8 \text{ GeV}/c$, while at higher p_T the measured yields and the PYTHIA values agree within uncertainties.

For π^\pm, K^\pm , and $p(\bar{p})$, the EPOS-LHC model predicts the spectral shape and normalization better than both of the PYTHIA tunes in the entire p_T range. For the resonances and multi-strange baryons, EPOS-LHC gives harder p_T spectra than the measured ones and performs better than PYTHIA at describing the yields of the multi-strange baryons. The EPOS-LHC model gives an accurate description for the Ξ baryon at $p_T \lesssim 2 \text{ GeV}/c$ both in shape and normalization, but deviates at higher p_T . The model also describes the shape of the p_T spectrum of Ω baryons, which have higher strangeness content, but does not reproduce the yield. For the K_S^0 and Λ (reported here for the first time at both $\sqrt{s} = 7$ and 13 TeV), as well as K^{*0} and ϕ , the models give similar descriptions at both collision energies. However, at $\sqrt{s} = 7 \text{ TeV}$ the agreement in normalization worsens for K_S^0 at intermediate p_T , while EPOS-LHC predicts harder spectra at higher p_T . For the ϕ meson, the EPOS-LHC model shows a marginal agreement with the data at low p_T , and monotonically deviates from the measured spectrum as the p_T increases.

Generally, the deviations of these models from the ALICE measurements are similar to those observed at lower \sqrt{s} , which were reported in Refs. [61, 24] for K^{*0} and ϕ and in Ref. [22] for π^\pm, K^\pm , and $p(\bar{p})$, although with a restricted p_T reach for the latter three particle species. To study how the models follow the changes in spectral shapes and normalization as a function of p_T as the energy increases from $\sqrt{s} = 7$ to 13 TeV, Fig. 15 shows the double ratios: the ratios of the measured p_T spectra at $\sqrt{s} = 13 \text{ TeV}$ to

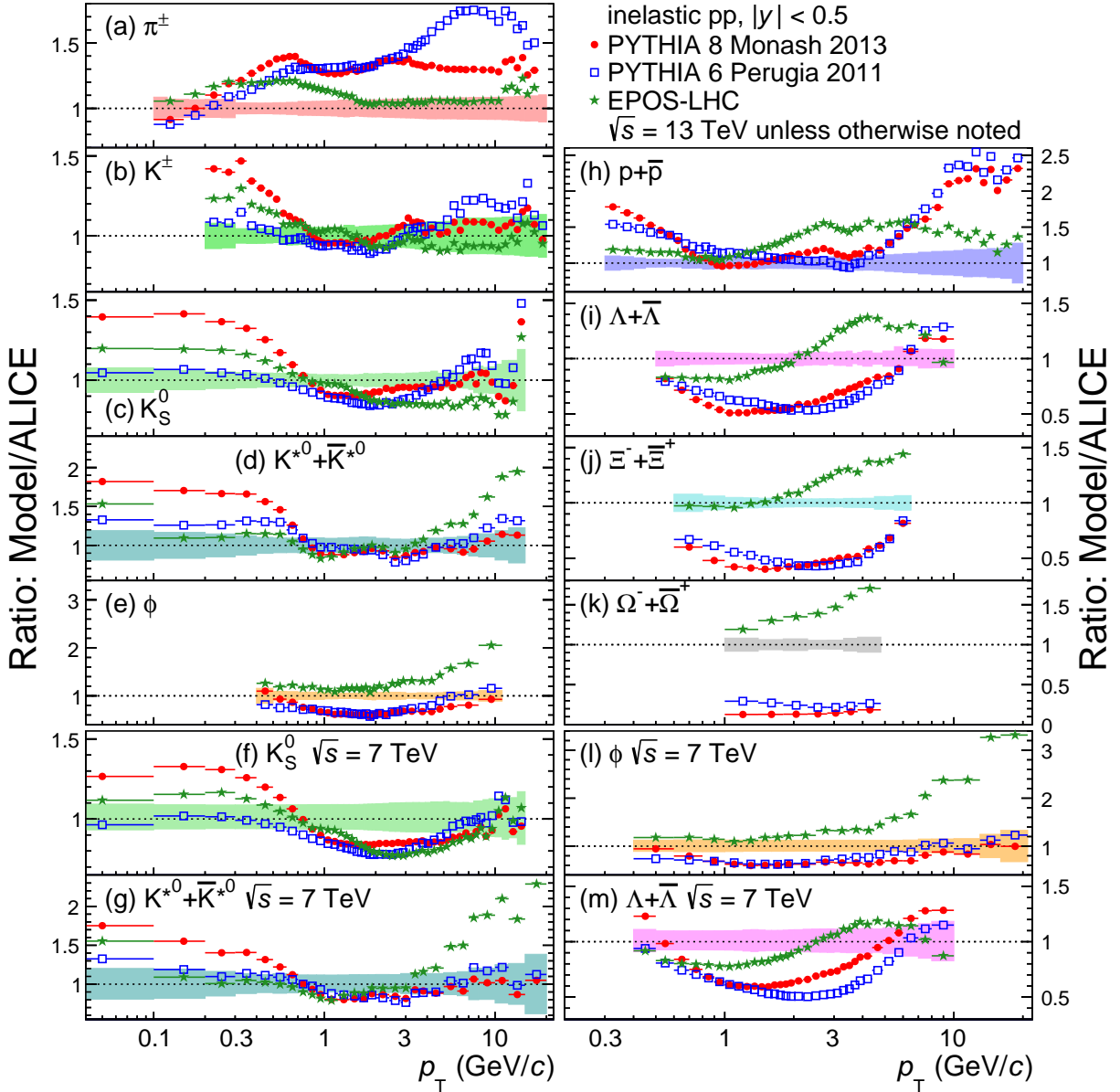


Figure 14: Ratios of p_T spectra from model calculations to the p_T spectra measured by ALICE in pp collisions at $\sqrt{s} = 13$ and 7 TeV. The total fractional uncertainties of the ALICE data are shown as shaded boxes. The measured p_T spectra of K^{*0} and ϕ in pp collisions at $\sqrt{s} = 7$ TeV are from Ref. [58]

$\sqrt{s} = 7$ TeV (see Fig. 6) are divided by the same ratios obtained from MC models. The comparisons indicate that the models capture well the increase of the yields with \sqrt{s} for the mesons shown in panels (a)–(e); for π^\pm , K^\pm , and K_S^0 , such an observation between two distinct collision energies in this p_T regime is reported here for the first time. For charged kaons, the models predict a more pronounced hardening with collision energy at high p_T . The tension seen in the range $2 \lesssim p_T \lesssim 6$ GeV/ c originates from the different analysis techniques which were used to obtain the combined spectra for $\sqrt{s} = 7$ TeV and at $\sqrt{s} = 13$ TeV. Note that the normalization uncertainties at both energies are not included in the reported fractional uncertainties in the figure. For both K^{*0} and ϕ mesons, the similarity of the deviations of the PYTHIA model (though with a different tune) from ALICE measurements was seen in our earlier measurements at $\sqrt{s} = 2.76$ TeV and $\sqrt{s} = 7$ TeV, as reported in Ref. [61]. Panels (f) and (g) demonstrate that the PYTHIA 6 and EPOS-LHC models agree with the measurements of $p(\bar{p})$ and Λ , in contrast, PYTHIA 8 systematically underestimates the measured data for $p_T \lesssim 8$ GeV/ c . For the multi-strange baryons (panels (h) and (i)), EPOS-LHC predicts the \sqrt{s} evolution of the p_T spectra above $p_T = 1$ GeV/ c the best, however the PYTHIA models also agree with the measured data for the Ω baryons above $p_T \sim 3$ GeV/ c . For baryons, the model description for PYTHIA 8 improves as the strangeness content increases.

The relative impact of the hardening observed in the p_T spectra in Fig. 6 for the various light-flavor hadrons is better seen in terms of the p_T -dependent yield ratios of different particle species. The comparison of these ratios to MC models allows the different hadronization mechanisms implemented in the event generators to be tested. In Fig. 16 the p_T -dependent baryon-to-meson ratios measured in pp collisions at $\sqrt{s} = 13$ TeV and discussed in the previous section are shown as a function of p_T and compared with the same MC models discussed above. The ratios for multi-strange baryons are better approximated by PYTHIA 6 than PYTHIA 8. As discussed for multi-strange baryon measurements performed by ALICE in pp collisions at $\sqrt{s} = 7$ TeV [25], this is a consequence of the removal of the “popcorn” mechanism [95] in the Perugia 2011 tune which in turn suppresses baryon production by favoring soft quark-antiquark pairing.

Although the Perugia 2011 tune reproduces the shape of the Ω baryon p_T spectrum within roughly 10% (as seen in Fig. 14), the Ω/ϕ ratio given by this model has large deviations from the data for $p_T \lesssim 4$ GeV/ c , the same p_T region where the model ϕ meson spectrum has its largest disagreement with the measured data (about 40%). The Perugia 2011 tune better characterizes the p_T evolution of the Ξ/ϕ ratio than the Monash 2013 tune of PYTHIA 8 for $p_T > 2$ GeV/ c . The EPOS-LHC model gives a good description of the shapes of the multi-strange baryon-to-meson ratios in the entire p_T range of the measurements. The model predicts quantitatively the magnitude of the Ξ/ϕ (Ω/ϕ) ratio with reasonable accuracy above (below) $p_T = 2$ GeV/ c . All three models approximate the p_T evolution of the Λ/K_S^0 ratio qualitatively, but systematically over-predict its magnitude for the full p_T range. The PYTHIA 8 and EPOS-LHC models predict the maximum of the ratio at higher p_T values than measured. EPOS-LHC fails to reproduce the magnitude of the Λ/K_S^0 ratio, deviating from the measured ratio by about a factor of three at the maximum of the peak. The p/π ratio is well described by the models in the low- p_T region ($\lesssim 2$ GeV/ c), however they fail to follow the enhancement and depletion behavior seen in the p_T region between 2 GeV/ c and 6 GeV/ c . All three models indicate a flattening behavior above ~ 10 GeV/ c , similar to what is seen in the measured data.

6.6 Comparison to pQCD calculations

The measured invariant cross sections are compared to next-to-leading order (NLO) perturbative QCD calculations using CT10NLO proton PDFs [96] with the DSS (de Florian, Sassot, and Stratmann) FF set [97, 3]. For charged pions a new version of the DSS FFs is available: the DSS14 FF [5] set. The NLO calculations are based on Ref. [98] which applies the same factorization scale value, $\mu = p_T$ for the factorization, renormalization and fragmentation scales. The variation of the scales to $\mu = p_T/2$ and $\mu = 2 p_T$ gives an estimate of the theoretical uncertainty; the PDF uncertainties are negligible in

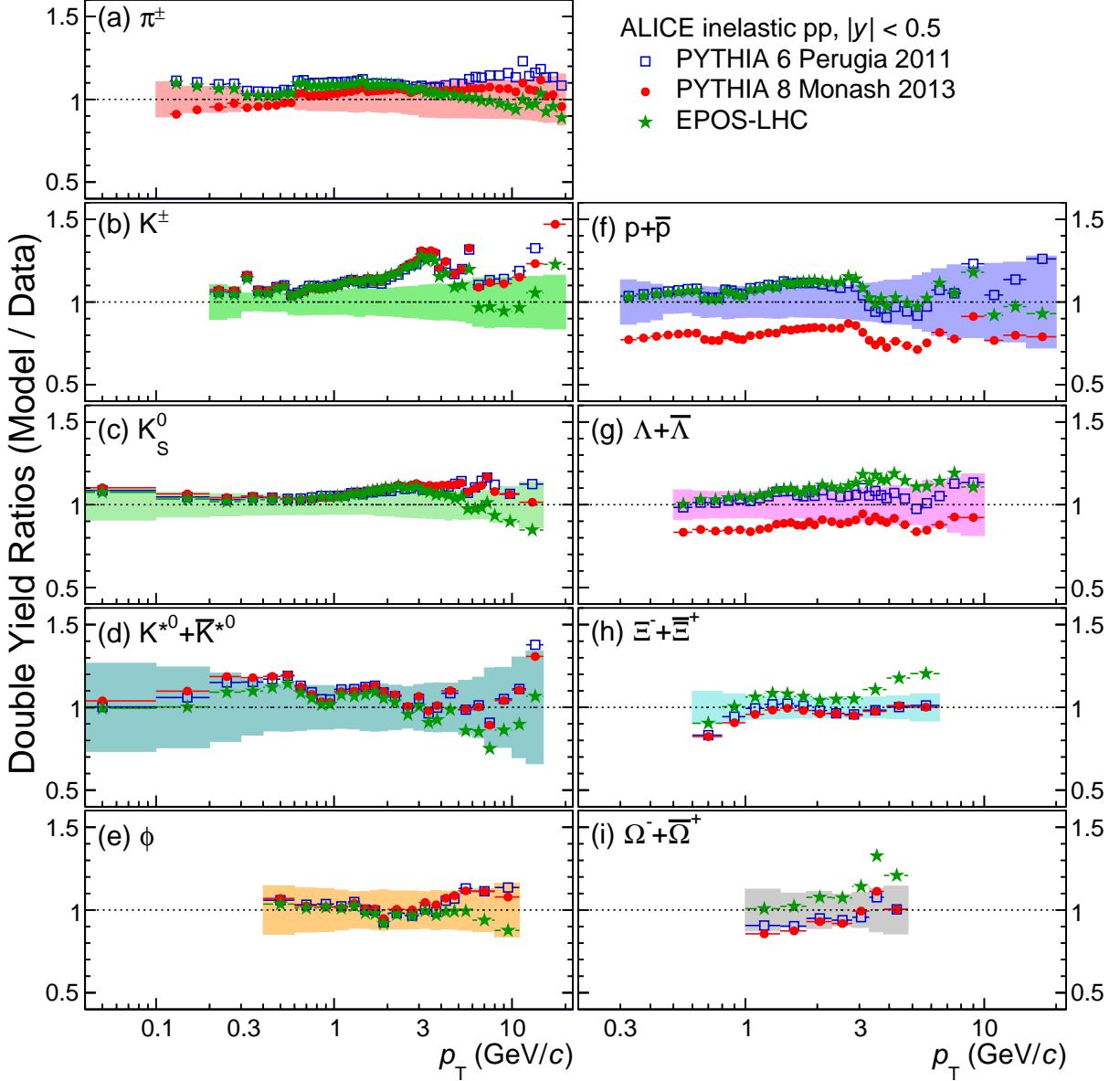


Figure 15: The measured 13-to-7 TeV ratios of hadron p_T spectra are compared with model calculations: where Y is the particle yield, the plotted double ratio is $(Y_{\text{model}}^{13 \text{ TeV}}/Y_{\text{model}}^{7 \text{ TeV}})/(Y_{\text{measured}}^{13 \text{ TeV}}/Y_{\text{measured}}^{7 \text{ TeV}})$. The measured p_T spectra at $\sqrt{s} = 7$ TeV are from Refs. [23, 25, 58]. The total fractional uncertainties of the measured yield ratios are shown as shaded boxes.

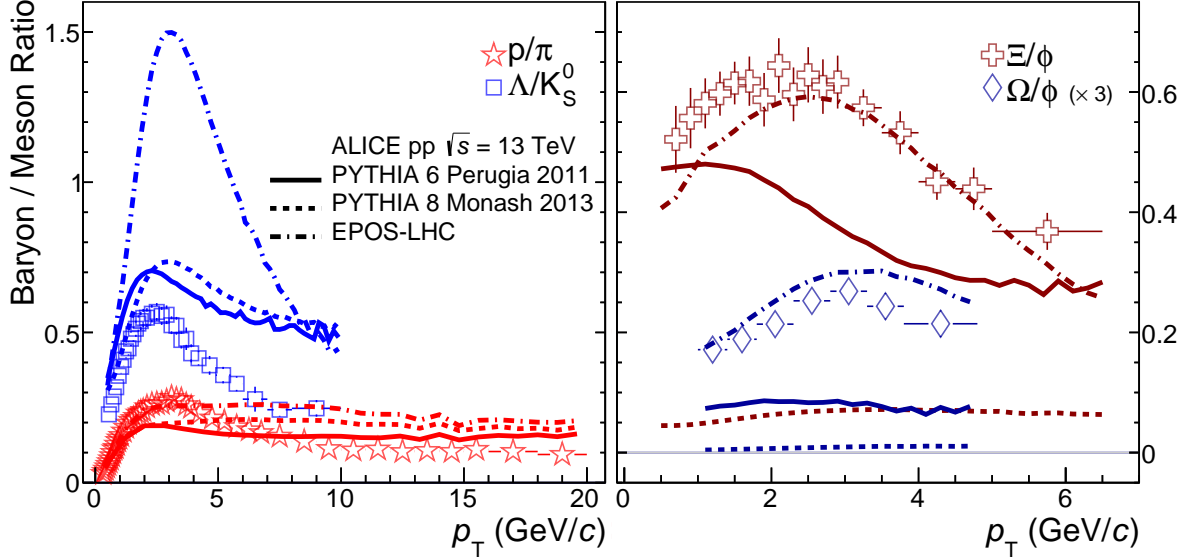


Figure 16: Baryon-to-meson particle ratios as a function of transverse momentum measured in pp collisions at $\sqrt{s} = 13$ TeV. Data are compared with several general-purpose Monte Carlo models. Statistical and systematic uncertainties are summed in quadrature, and are shown as vertical error bars.

comparison to the scale uncertainty. The rather large scale uncertainty observed at lower p_T ($2 < p_T < 10$ GeV/c) stabilizes at $\pm 20 - 30\%$ for $p_T \simeq 10$ GeV/c which is the region where the NLO calculations are trustworthy and free from non-perturbative effects.

The production of π^\pm , K^\pm , and $p(\bar{p})$ from hard scattering becomes dominated by gluon fragmentation with increasing collision energy in the p_T range of the measurement [3]. The presented identified charged-hadron spectra can therefore help to constrain the gluon-to-charged-hadron fragmentation function [4] which is of crucial importance to a better description of the LHC charged-hadron data with NLO pQCD (see e.g. Ref. [99]). The invariant differential cross sections for π^\pm , K^\pm , and $p(\bar{p})$ are shown in the left panel of Fig. 17 in comparison to NLO pQCD calculations. Since, to date, no calculation exists for the scale uncertainties of the DSS14, only the DSS FFs with the corresponding scale uncertainties are reported in the figure. In the right panel of Fig. 17 the ratios of the measured data and the NLO pQCD calculations to the Lévy–Tsallis fits of the π^\pm , K^\pm , and $p(\bar{p})$ cross sections are shown. For $p_T > 10$ GeV/c the NLO pQCD calculations, employing the DSS14 FFs and using the DSS scale uncertainties, over-predict the measured pion cross section by up to a factor of approximately two, but describe the shape of the p_T spectrum rather well. Similar discrepancies between NLO pQCD calculations and the measured cross sections have also been reported for the measurements of neutral pions (π^0) at $\sqrt{s} = 7$ and 8 TeV [100, 10] from ALICE, leaving room for future improvements in the calculations. It is worth noting that the published π^0 measurement at $\sqrt{s} = 7$ TeV [100] adds important constraints for gluon FFs, which would help reduce the FF uncertainties. The NLO calculations describe charged kaons better than pions, which is reflected in the better agreement between the calculated cross section and with the measured data-to-fit ratio within the quoted uncertainties. The deviations between the NLO calculations and the data generally increase with p_T , which is significantly stronger for protons; they deviate the most from the measured values for all μ scale choices. The NLO calculations significantly overestimate the measured data at high p_T .

At lower p_T (< 10 GeV/c) the discrepancy between the NLO calculations and the measured data is reduced for all particle species but at the cost of the increase of the scale uncertainties. In this p_T regime, soft parton interactions and resonance decays dominate particle production, which cannot be described within the framework of pQCD. This is also reflected on the shape of the distributions, which is not described by the calculation. The presented results show that independent fragmentation works rather

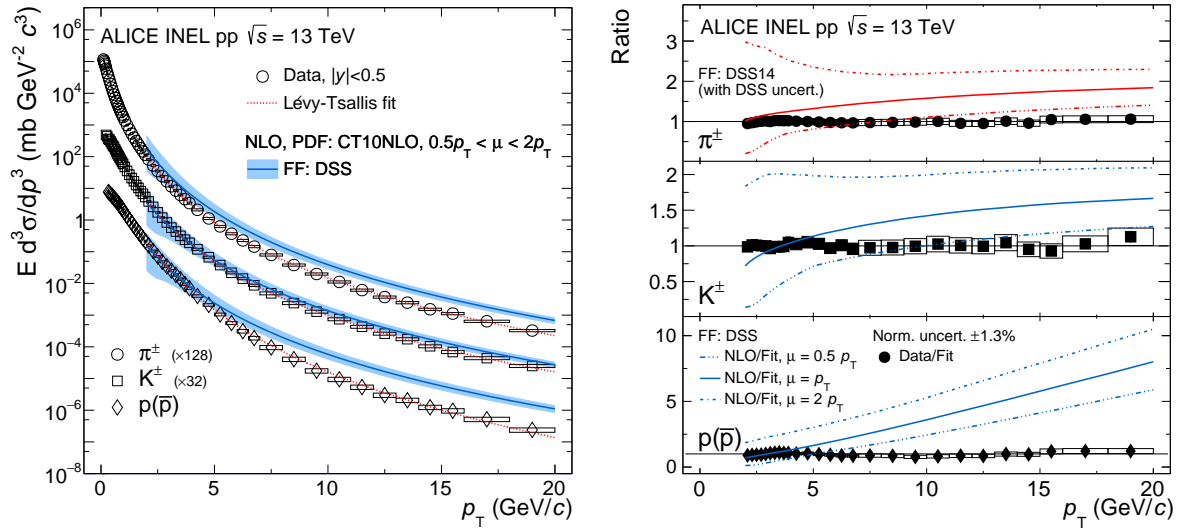


Figure 17: (Left) Invariant differential cross sections for π^\pm , K^\pm , and $p(\bar{p})$ production, compared with NLO pQCD calculations using CT10NLO PDFs [96] with DSS14 FFs [5] for π^\pm and DSS FFs [97, 3] for K^\pm and $p(\bar{p})$. The shaded band around the NLO calculations corresponds to the scale uncertainty. (Right) Ratio of measured data (points) or NLO calculations (lines) to a Lévy–Tsallis function that is fitted to the data. The NLO-to-fit ratio is shown for the scale $\mu = p_T$ and the variations $\mu = p_T/2$ and $\mu = 2 p_T$. The fully correlated normalization uncertainty is indicated in the legend.

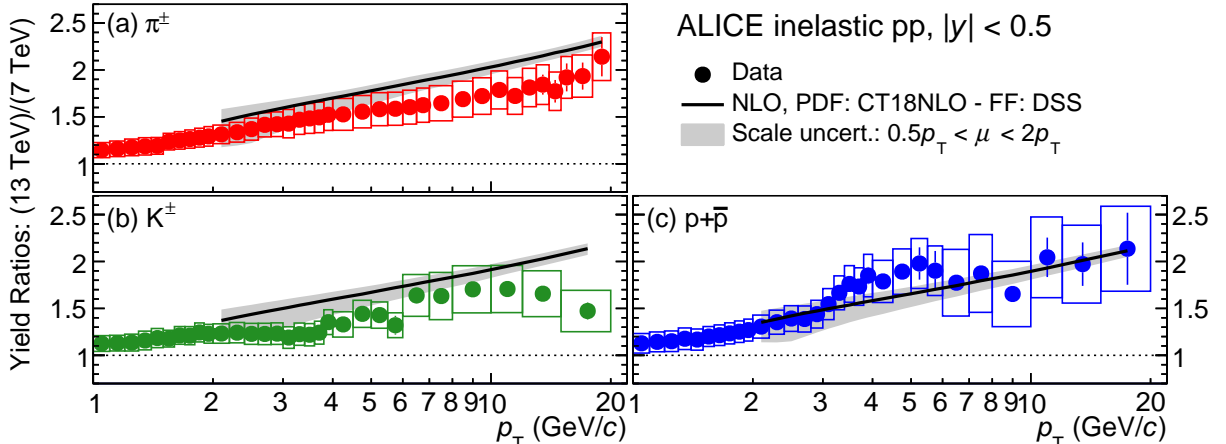


Figure 18: Ratios of transverse-momentum spectra of π^\pm , K^\pm , and $p(\bar{p})$ in minimum bias inelastic pp collisions at $\sqrt{s} = 13$ TeV to those at $\sqrt{s} = 7$ TeV [23]. Solid lines show predictions from next-to-leading order (NLO) pQCD calculation using DSS fragmentation functions [98]. Statistical and systematic uncertainties are shown as vertical error bars and boxes, respectively.

well for mesons, in particular for $p_T > 6$ GeV/c, however for (anti)protons the spectral shape deviates towards the high- p_T region.

Though the p_T dependence of the cross sections at a given collision energy is not described well by the NLO calculations, the p_T dependence of the ratios of the p_T spectra at $\sqrt{s} = 7$ [23] and 13 TeV is described better. Such a comparison is shown in Fig. 18, where the ratio of invariant yields in inelastic pp collisions at $\sqrt{s} = 13$ TeV to those at 7 TeV is compared to the same ratio calculated using NLO pQCD. The agreement between the data and NLO calculations is notably improved compared to the NLO results for spectra themselves. Taking a double ratio, where the ratios of the measured spectra at $\sqrt{s} = 13$ and

7 TeV are divided by the ratios from the NLO pQCD calculations, the observed difference is below 10% (20%) for pions (kaons and protons).

7 Summary

The production of light-flavor hadrons at midrapidity was measured in inelastic pp collisions at $\sqrt{s} = 13$ TeV. Additionally, single-particle p_T distributions of K_S^0 , Λ , and $\bar{\Lambda}$ were also measured in inelastic pp collisions at $\sqrt{s} = 7$ TeV. The presented measurements complement the existing ones at lower collision energies, allowing particle production to be studied over a wide range of \sqrt{s} . All p_T distributions are observed to become harder for $p_T > 2 \text{ GeV}/c$ with increasing collision energy.

The p_T -integrated hadron yields normalized to the pion yields saturate as a function of \sqrt{s} at LHC energies for the studied non-strange and single-strange hadrons. In contrast, a hint of an increase in the multi-strange hadron yields is apparent as \sqrt{s} increases from $\sqrt{s} = 7$ to 13 TeV, the increase being more pronounced for Ω baryons, which have the largest strange quark content among the studied hadrons. This observation is similar to our recent measurements performed as a function of charged-particle multiplicity in pp collisions at $\sqrt{s} = 7$ and 13 TeV [51, 26].

A significant deviation from the empirical transverse mass scaling relation of the production cross sections between π^\pm and K^\pm and K_S^0 is observed for $p_T < 2 \text{ GeV}/c$. Empirical x_T scaling for π^\pm , K^\pm , K^{*0} , and $p(\bar{p})$ is well satisfied (within roughly 20–40%) in the hard scattering region of particle production.

Next-to-leading order pQCD calculations performed at $\sqrt{s} = 13$ TeV, using the DSS14 FFs for π^\pm and the DSS FFs for K^\pm and $p(\bar{p})$, over-predict the measured p_T spectra both for charged pions and (anti)protons, suggesting that the fragmentation functions are not well tuned in the accessible kinematic domain of the presented measurement.

The measured hadron p_T spectra are compared with results of Monte Carlo calculations. The results of PYTHIA calculations only partially describe the measured data, while the EPOS-LHC model describes several aspects of the data, notably strangeness production. However, further tuning of the models is warranted in order to improve their descriptions of the measured trends.

Acknowledgements

The ALICE Collaboration would like to thank all its engineers and technicians for their invaluable contributions to the construction of the experiment and the CERN accelerator teams for the outstanding performance of the LHC complex. The ALICE Collaboration gratefully acknowledges the resources and support provided by all Grid centres and the Worldwide LHC Computing Grid (WLCG) collaboration. The ALICE Collaboration acknowledges the following funding agencies for their support in building and running the ALICE detector: A. I. Alikhanyan National Science Laboratory (Yerevan Physics Institute) Foundation (ANSL), State Committee of Science and World Federation of Scientists (WFS), Armenia; Austrian Academy of Sciences, Austrian Science Fund (FWF): [M 2467-N36] and Nationalstiftung für Forschung, Technologie und Entwicklung, Austria; Ministry of Communications and High Technologies, National Nuclear Research Center, Azerbaijan; Conselho Nacional de Desenvolvimento Científico e Tecnológico (CNPq), Financiadora de Estudos e Projetos (Finep), Fundação de Amparo à Pesquisa do Estado de São Paulo (FAPESP) and Universidade Federal do Rio Grande do Sul (UFRGS), Brazil; Ministry of Education of China (MOEC) , Ministry of Science & Technology of China (MSTC) and National Natural Science Foundation of China (NSFC), China; Ministry of Science and Education and Croatian Science Foundation, Croatia; Centro de Aplicaciones Tecnológicas y Desarrollo Nuclear (CEADEN), Cubaenergía, Cuba; Ministry of Education, Youth and Sports of the Czech Republic, Czech Republic; The Danish Council for Independent Research | Natural Sciences, the VILLUM FONDEN and Danish National Research Foundation (DNRF), Denmark; Helsinki Institute of Physics (HIP), Finland;

Commissariat à l’Energie Atomique (CEA) and Institut National de Physique Nucléaire et de Physique des Particules (IN2P3) and Centre National de la Recherche Scientifique (CNRS), France; Bundesministerium für Bildung und Forschung (BMBF) and GSI Helmholtzzentrum für Schwerionenforschung GmbH, Germany; General Secretariat for Research and Technology, Ministry of Education, Research and Religions, Greece; National Research, Development and Innovation Office, Hungary; Department of Atomic Energy Government of India (DAE), Department of Science and Technology, Government of India (DST), University Grants Commission, Government of India (UGC) and Council of Scientific and Industrial Research (CSIR), India; Indonesian Institute of Science, Indonesia; Centro Fermi - Museo Storico della Fisica e Centro Studi e Ricerche Enrico Fermi and Istituto Nazionale di Fisica Nucleare (INFN), Italy; Institute for Innovative Science and Technology , Nagasaki Institute of Applied Science (IIIST), Japanese Ministry of Education, Culture, Sports, Science and Technology (MEXT) and Japan Society for the Promotion of Science (JSPS) KAKENHI, Japan; Consejo Nacional de Ciencia (CONACYT) y Tecnología, through Fondo de Cooperación Internacional en Ciencia y Tecnología (FONCICYT) and Dirección General de Asuntos del Personal Académico (DGAPA), Mexico; Nederlandse Organisatie voor Wetenschappelijk Onderzoek (NWO), Netherlands; The Research Council of Norway, Norway; Commission on Science and Technology for Sustainable Development in the South (COMSATS), Pakistan; Pontificia Universidad Católica del Perú, Peru; Ministry of Science and Higher Education, National Science Centre and WUT ID-UB, Poland; Korea Institute of Science and Technology Information and National Research Foundation of Korea (NRF), Republic of Korea; Ministry of Education and Scientific Research, Institute of Atomic Physics and Ministry of Research and Innovation and Institute of Atomic Physics, Romania; Joint Institute for Nuclear Research (JINR), Ministry of Education and Science of the Russian Federation, National Research Centre Kurchatov Institute, Russian Science Foundation and Russian Foundation for Basic Research, Russia; Ministry of Education, Science, Research and Sport of the Slovak Republic, Slovakia; National Research Foundation of South Africa, South Africa; Swedish Research Council (VR) and Knut & Alice Wallenberg Foundation (KAW), Sweden; European Organization for Nuclear Research, Switzerland; Suranaree University of Technology (SUT), National Science and Technology Development Agency (NSDTA) and Office of the Higher Education Commission under NRU project of Thailand, Thailand; Turkish Atomic Energy Agency (TAEK), Turkey; National Academy of Sciences of Ukraine, Ukraine; Science and Technology Facilities Council (STFC), United Kingdom; National Science Foundation of the United States of America (NSF) and United States Department of Energy, Office of Nuclear Physics (DOE NP), United States of America.

References

- [1] D. d’Enterria, R. Engel, T. Pierog, S. Ostapchenko, and K. Werner, “Constraints from the first LHC data on hadronic event generators for ultra-high energy cosmic-ray physics”, *Astropart. Phys.* **35** (2011) 98–113, arXiv:1101.5596 [astro-ph.HE].
- [2] J. C. Collins, D. E. Soper, and G. F. Sterman, “Factorization of Hard Processes in QCD”, *Adv. Ser. Direct. High Energy Phys.* **5** (1989) 1–91, arXiv:hep-ph/0409313 [hep-ph].
- [3] D. de Florian, R. Sassot, and M. Stratmann, “Global analysis of fragmentation functions for protons and charged hadrons”, *Phys. Rev.* **D76** (2007) 074033, arXiv:0707.1506 [hep-ph].
- [4] D. d’Enterria, K. J. Eskola, I. Helenius, and H. Paukkunen, “Confronting current NLO parton fragmentation functions with inclusive charged-particle spectra at hadron colliders”, *Nucl. Phys.* **B883** (2014) 615–628, arXiv:1311.1415 [hep-ph].
- [5] D. de Florian, R. Sassot, M. Epele, R. J. Hernández-Pinto, and M. Stratmann, “Parton-to-Pion Fragmentation Reloaded”, *Phys. Rev.* **D91** no. 1, (2015) 014035, arXiv:1410.6027 [hep-ph].
- [6] D. de Florian, M. Epele, R. J. Hernandez-Pinto, R. Sassot, and M. Stratmann, “Parton-to-Kaon Fragmentation Revisited”, *Phys. Rev.* **D95** no. 9, (2017) 094019, arXiv:1702.06353 [hep-ph].

- [7] **ALICE** Collaboration, B. Abelev *et al.*, “Production of charged pions, kaons and protons at large transverse momenta in pp and Pb–Pb collisions at $\sqrt{s_{\text{NN}}} = 2.76$ TeV”, *Phys. Lett.* **B736** (2014) 196–207, arXiv:1401.1250 [nucl-ex].
- [8] **ALICE** Collaboration, S. Acharya *et al.*, “Production of π^0 and η mesons up to high transverse momentum in pp collisions at 2.76 TeV”, *Eur. Phys. J.* **C77** no. 5, (2017) 339, arXiv:1702.00917 [hep-ex]. [Eur. Phys. J.C77,no.9,586(2017)].
- [9] **ALICE** Collaboration, K. Koch, “ π^0 and η measurement with photon conversions in ALICE in proton-proton collisions at $\sqrt{s} = 7$ TeV”, *Nucl. Phys.* **A855** (2011) 281–284, arXiv:1103.2217 [hep-ex].
- [10] **ALICE** Collaboration, S. Acharya *et al.*, “ π^0 and η meson production in proton-proton collisions at $\sqrt{s} = 8$ TeV”, *Eur. Phys. J.* **C78** no. 3, (2018) 263, arXiv:1708.08745 [hep-ex].
- [11] **CDF** Collaboration, T. Aaltonen *et al.*, “Measurement of Particle Production and Inclusive Differential Cross Sections in $p\bar{p}$ Collisions at $\sqrt{s} = 1.96$ TeV”, *Phys. Rev.* **D79** (2009) 112005, arXiv:0904.1098 [hep-ex]. [Erratum: Phys. Rev.D82,119903(2010)].
- [12] **CDF** Collaboration, F. Abe *et al.*, “Transverse Momentum Distributions of Charged Particles Produced in $p\bar{p}$ Interactions at $\sqrt{s} = 630$ GeV and 1800 GeV”, *Phys. Rev. Lett.* **61** (1988) 1819.
- [13] **UA1** Collaboration, C. Albajar *et al.*, “A Study of the General Characteristics of $p\bar{p}$ Collisions at $\sqrt{s} = 0.2$ TeV to 0.9 TeV”, *Nucl. Phys.* **B335** (1990) 261–287.
- [14] **STAR** Collaboration, J. Adams *et al.*, “Identified hadron spectra at large transverse momentum in p+p and d+Au collisions at $\sqrt{s_{\text{NN}}} = 200$ GeV”, *Phys. Lett.* **B637** (2006) 161–169, arXiv:nucl-ex/0601033 [nucl-ex].
- [15] **CMS** Collaboration, S. Chatrchyan *et al.*, “Charged particle transverse momentum spectra in pp collisions at $\sqrt{s} = 0.9$ and 7 TeV”, *JHEP* **08** (2011) 086, arXiv:1104.3547 [hep-ex].
- [16] F. Arleo, S. J. Brodsky, D. S. Hwang, and A. M. Sickles, “Higher-Twist Dynamics in Large Transverse Momentum Hadron Production”, *Phys. Rev. Lett.* **105** (2010) 062002, arXiv:0911.4604 [hep-ph].
- [17] R. Hagedorn, “Statistical thermodynamics of strong interactions at high energies”, *Nuovo Cimento, Suppl.* **3** no. CERN-TH-520, (1965) 147–186.
<http://cds.cern.ch/record/346206>.
- [18] G. Gatoff and C. Y. Wong, “Origin of the soft p_T spectra”, *Phys. Rev.* **D46** (1992) 997–1006.
- [19] **STAR** Collaboration, B. I. Abelev *et al.*, “Strange particle production in p+p collisions at $\sqrt{s} = 200$ GeV”, *Phys. Rev.* **C75** (2007) 064901, arXiv:nucl-ex/0607033 [nucl-ex].
- [20] P. K. Khandai, P. Sett, P. Shukla, and V. Singh, “Transverse Mass Spectra and Scaling of Hadrons at RHIC and LHC Energies”, arXiv:1205.0648 [hep-ph].
- [21] L. AltenkÃd'mper, F. Bock, C. Loizides, and N. Schmidt, “Applicability of transverse mass scaling in hadronic collisions at energies available at the CERN Large Hadron Collider”, *Phys. Rev.* **C96** no. 6, (2017) 064907, arXiv:1710.01933 [hep-ph].
- [22] **ALICE** Collaboration, J. Adam *et al.*, “Measurement of pion, kaon and proton production in proton-proton collisions at $\sqrt{s} = 7$ TeV”, *Eur. Phys. J.* **C75** no. 5, (2015) 226, arXiv:1504.00024 [nucl-ex].
- [23] **ALICE** Collaboration, J. Adam *et al.*, “Multiplicity dependence of charged pion, kaon, and (anti)proton production at large transverse momentum in p-Pb collisions at $\sqrt{s_{\text{NN}}} = 5.02$ TeV”, *Phys. Lett.* **B760** (2016) 720–735, arXiv:1601.03658 [nucl-ex].
- [24] **ALICE** Collaboration, B. Abelev *et al.*, “Production of $K^*(892)^0$ and $\phi(1020)$ in pp collisions at $\sqrt{s} = 7$ TeV”, *Eur. Phys. J.* **C72** (2012) 2183, arXiv:1208.5717 [hep-ex].
- [25] **ALICE** Collaboration, B. Abelev *et al.*, “Multi-strange baryon production in pp collisions at $\sqrt{s} = 7$ TeV with ALICE”, *Phys. Lett.* **B712** (2012) 309–318, arXiv:1204.0282 [nucl-ex].

- [26] **ALICE** Collaboration, S. Acharya *et al.*, “Multiplicity dependence of (multi-)strange hadron production in proton-proton collisions at $\sqrt{s} = 13$ TeV”, arXiv:1908.01861 [nucl-ex].
- [27] **ALICE** Collaboration, S. Acharya *et al.*, “Charged-particle production as a function of multiplicity and transverse spherocity in pp collisions at $\sqrt{s} = 5.02$ and 13 TeV”, *Eur. Phys. J.* **C79** no. 10, (2019) 857, arXiv:1905.07208 [nucl-ex].
- [28] P. Z. Skands, “Tuning Monte Carlo generators: The Perugia tunes”, *Phys. Rev.* **D82** (2010) 074018, arXiv:1005.3457 [hep-ph].
- [29] P. Z. Skands, S. Carrazza, and J. Rojo, “Tuning PYTHIA 8.1: the Monash 2013 tune”, *Eur. Phys. J.* **C74** (2014) 3024, arXiv:1404.5630 [hep-ph].
- [30] T. Pierog, I. Karpenko, J. M. Katzy, E. Yatsenko, and K. Werner, “EPOS LHC: Test of collective hadronization with data measured at the CERN Large Hadron Collider”, *Phys. Rev.* **C92** no. 3, (2015) 034906, arXiv:1306.0121 [hep-ph].
- [31] **ALICE** Collaboration, K. Aamodt *et al.*, “The ALICE experiment at the CERN LHC”, *J. Instrum.* **3** (2008) S08002.
- [32] **ALICE** Collaboration, B. Abelev *et al.*, “Performance of the ALICE Experiment at the CERN LHC”, *Int. J. Mod. Phys.* **A29** (2014) 1430044, arXiv:1402.4476 [nucl-ex].
- [33] **ALICE** Collaboration, E. Abbas *et al.*, “Performance of the ALICE VZERO system”, *J. Instrum.* **8** (2013) P10016.
- [34] **ALICE** Collaboration, “The ALICE definition of primary particles”, <https://cds.cern.ch/record/2270008>.
- [35] **ALICE** Collaboration, K. Aamodt *et al.*, “Alignment of the ALICE Inner Tracking System with cosmic-ray tracks”, *J. Inst.* **5** (2010) P03003, arXiv:1001.0502 [physics.ins-det].
- [36] J. Alme *et al.*, “The ALICE TPC, a large 3-dimensional tracking device with fast readout for ultra-high multiplicity events”, *Nucl. Instrum. Methods Phys. Res. A* **622** (2010) 316–67.
- [37] A. N. Akindinov *et al.*, “Particle identification with the ALICE TOF detector at very high particle multiplicity”, *Eur. Phys. J. C* **32** (2004) s165–77.
- [38] A. Akindinov *et al.*, “The ALICE Time-Of-Flight system: Construction, assembly and quality tests”, *Nuovo Cimento B* **124** (2009) 235.
- [39] A. Akindinov *et al.*, “Results of the ALICE time-of-flight detector from the 2009 cosmic-ray data taking”, *Eur. Phys. J. C* **68** (2010) 601.
- [40] **ALICE** Collaboration, J. Adam *et al.*, “Pseudorapidity and transverse-momentum distributions of charged particles in proton- $\bar{\Lambda}$ proton collisions at $\sqrt{s} = 13$ TeV”, *Phys. Lett.* **B753** (2016) 319–329, arXiv:1509.08734 [nucl-ex].
- [41] R. Brun, F. Carminati, and S. Giani, *GEANT – Detector Description and Simulation Tool, CERN Program Library Long Writeup W5013*. CERN, Geneva, 1994.
- [42] **Particle Data Group** Collaboration, M. Tanabashi *et al.*, “Review of particle physics”, *Phys. Rev. D* **98** (Aug, 2018) 030001.
- [43] G. Battistoni, S. Muraro, P. R. Sala, F. Cerutti, A. Ferrari, S. Roesler, A. Fasso, and J. Ranft, “The FLUKA code: Description and benchmarking”, *AIP Conf. Proc.* **896** (2007) 31–49. [,31(2007)].
- [44] **ALICE** Collaboration, B. Abelev *et al.*, “Measurement of inelastic, single- and double-diffraction cross sections in proton–proton collisions at the LHC with ALICE”, *Eur. Phys. J. C* **73** no. 6, (2013) 2456, arXiv:1208.4968 [hep-ex].
- [45] **ALICE** Collaboration, J. Adam *et al.*, “ALICE luminosity determination for pp collisions at $\sqrt{s} = 13$ TeV”, *ALICE-PUBLIC-2016-002* (2016) 1.
- [46] C. Loizides, J. Kamin, and D. d’Enterria, “Improved Monte Carlo Glauber predictions at present and future nuclear colliders”, *Phys. Rev.* **C97** no. 5, (2018) 054910, arXiv:1710.07098 [nucl-ex]. [erratum: *Phys. Rev.C99,no.1,019901(2019)*].

- [47] **ALICE** Collaboration, B. Abelev *et al.*, “Centrality dependence of π , K, p production in Pb-Pb collisions at $\sqrt{s_{NN}} = 2.76$ TeV”, *Phys. Rev.* **C88** (2013) 044910, arXiv:1303.0737 [hep-ex].
- [48] **ALICE** Collaboration, J. Adam *et al.*, “Production of $K^*(892)^0$ and $\phi(1020)$ in p-Pb collisions at $\sqrt{s_{NN}} = 5.02$ TeV”, *Eur. Phys. J.* **C76** (2016) 245, arXiv:1601.07868 [nucl-ex].
- [49] **ALICE** Collaboration, K. Aamodt *et al.*, “Production of pions, kaons and protons in pp collisions at $\sqrt{s} = 900$ GeV with ALICE at the LHC”, *Eur. Phys. J.* **C71** (2011) 1655, arXiv:1101.4110 [hep-ex].
- [50] **ALICE** Collaboration, J. Adam *et al.*, “Centrality dependence of the nuclear modification factor of charged pions, kaons, and protons in Pb-Pb collisions at $\sqrt{s_{NN}} = 2.76$ TeV”, *Phys. Rev.* **C93** no. 3, (2016) 034913, arXiv:1506.07287 [nucl-ex].
- [51] **ALICE** Collaboration, S. Acharya *et al.*, “Multiplicity dependence of light-flavor hadron production in pp collisions at $\sqrt{s} = 7$ TeV”, *Phys. Rev.* **C99** no. 2, (2019) 024906, arXiv:1807.11321 [nucl-ex].
- [52] **ALICE** Collaboration, J. Adam *et al.*, “Pseudorapidity and transverse-momentum distributions of charged particles in proton-proton collisions at $\sqrt{s} = 13$ TeV”, *Phys. Lett.* **B753** (2016) 319–329, arXiv:1509.08734 [nucl-ex].
- [53] **ALICE** Collaboration, J. Adam *et al.*, “Particle identification in ALICE: a Bayesian approach”, *Eur. Phys. J. Plus* **131** no. 5, (2016) 168, arXiv:1602.01392 [physics.data-an].
- [54] A. Akindinov *et al.*, “Performance of the ALICE Time-Of-Flight detector at the LHC”, *Eur. Phys. J. Plus* **128** (2013) 44.
- [55] **ALICE** Collaboration, D. Di Bari, “The pattern recognition method for the CsI-RICH detector in ALICE”, *Nucl. Instrum. Meth.* **A502** (2003) 300–304.
- [56] **ALICE** Collaboration, K. Aamodt *et al.*, “Strange particle production in proton-proton collisions at $\sqrt{s} = 0.9$ TeV with ALICE at the LHC”, *Eur. Phys. J.* **C71** (2011) 1594, arXiv:1012.3257 [hep-ex].
- [57] **ALICE** Collaboration, B. Abelev *et al.*, “ $K^*(892)^0$ and $\phi(1020)$ production in Pb-Pb collisions at $\sqrt{s_{NN}} = 2.76$ TeV”, *Phys. Rev. C* **91** (2015) 024609, arXiv:1404.0495 [nucl-ex].
- [58] **ALICE** Collaboration, S. Acharya *et al.*, “ $K^*(892)^0$ and $\phi(1020)$ production at midrapidity in pp collisions at $\sqrt{s} = 8$ TeV”, arXiv:1910.14410 [nucl-ex].
- [59] C. Tsallis, “Possible generalization of Boltzmann-Gibbs statistics”, *J. Stat. Phys.* **52** (1988) 479.
- [60] **STAR** Collaboration, B. I. Abelev *et al.*, “Strange particle production in p+p collisions at $\sqrt{s} = 200$ GeV”, *Phys. Rev. C* **75** (2007) 064901.
- [61] **ALICE** Collaboration, J. Adam *et al.*, “ $K^*(892)^0$ and $\phi(1020)$ meson production at high transverse momentum in pp and Pb-Pb collisions at $\sqrt{s_{NN}} = 2.76$ TeV”, *Phys. Rev. C* **95** no. 6, (2017) 064606, arXiv:1702.00555 [nucl-ex].
- [62] E. Schnedermann, J. Sollfrank, and U. Heinz, “Thermal phenomenology of hadrons from 200A GeV S+S collisions”, *Phys. Rev. C* **48** (1993) 2462–75.
- [63] **ALICE** Collaboration, S. Acharya *et al.*, “Production of charged pions, kaons and (anti-)protons in Pb-Pb and inelastic pp collisions at $\sqrt{s_{NN}} = 5.02$ TeV”, arXiv:1910.07678 [nucl-ex].
- [64] **ALICE** Collaboration, B. Abelev *et al.*, “ K_S^0 and Λ production in Pb-Pb collisions at $\sqrt{s_{NN}} = 2.76$ TeV”, *Phys. Rev. Lett.* **111** (2013) 222301, arXiv:1307.5530 [nucl-ex].
- [65] S. J. Brodsky and G. R. Farrar, “Scaling Laws at Large Transverse Momentum”, *Phys. Rev. Lett.* **31** (1973) 1153–1156.
- [66] D. Sivers, S. J. Brodsky, and R. Blankenbecler, “Large transverse momentum processes”, *Physics Reports* **23** no. 1, (1976) 1 – 121.
<http://www.sciencedirect.com/science/article/pii/0370157376900156>.
- [67] R. Blankenbecler, S. J. Brodsky, and J. F. Gunion, “Magnitude of large-transverse-momentum

- cross sections”, *Phys. Rev. D* **18** (Aug, 1978) 900–926.
<https://link.aps.org/doi/10.1103/PhysRevD.18.900>.
- [68] F. Arleo, D. d’Enterria, and A. S. Yoon, “Single-inclusive production of large-pT charged particles in hadronic collisions at TeV energies and perturbative QCD predictions”, *JHEP* **06** (2010) 035, arXiv:1003.2963 [hep-ph].
- [69] **British-Scandinavian** Collaboration, B. Alper *et al.*, “The Production of Charged Particles with High Transverse Momentum in Proton-Proton Collisions at the CERN ISR”, *Nucl. Phys.* **B87** (1975) 19.
- [70] **UA5** Collaboration, K. Alpgard *et al.*, “First Results on Complete Events from p anti-p Collisions at the Center-of-Mass Energy of 540-GeV”, *Phys. Lett.* **107B** (1981) 310–314.
- [71] **PHENIX** Collaboration, A. Adare *et al.*, “Measurement of neutral mesons in p+p collisions at $\sqrt{s} = 200$ GeV and scaling properties of hadron production”, *Phys. Rev.* **D83** (2011) 052004, arXiv:1005.3674 [hep-ex].
- [72] K. Jiang, Y. Zhu, W. Liu, H. Chen, C. Li, L. Ruan, Z. Tang, Z. Xu, and Z. Xu, “Onset of radial flow in p+p collisions”, *Phys. Rev.* **C91** no. 2, (2015) 024910, arXiv:1312.4230 [nucl-ex].
- [73] B. Andersson, G. Gustafson, and T. Sjöstrand, “A model for baryon production in quark and gluon jets”, *Nuclear Physics B* **197** no. 1, (1982) 45 – 54.
<http://www.sciencedirect.com/science/article/pii/0550321382901535>.
- [74] B. Andersson, G. Gustafson, and T. Sjostrand, “Baryon Production in Jet Fragmentation and Υ Decay”, *Phys. Scripta* **32** (1985) 574.
- [75] J. Schaffner-Bielich, D. Kharzeev, L. D. McLerran, and R. Venugopalan, “Generalized scaling of the transverse mass spectrum at the relativistic heavy ion collider”, *Nucl. Phys.* **A705** (2002) 494–507, arXiv:nucl-th/0108048 [nucl-th].
- [76] R. F. Cahalan, K. A. Geer, J. Kogut, and L. Susskind, “Asymptotic freedom and the absence of vector-gluon exchange in wide-angle hadronic collisions”, *Phys. Rev. D* **11** (Mar, 1975) 1199–1212. <https://link.aps.org/doi/10.1103/PhysRevD.11.1199>.
- [77] R. Sassot, P. Zurita, and M. Stratmann, “Inclusive Hadron Production in the CERN-LHC Era”, *Phys. Rev.* **D82** (2010) 074011, arXiv:1008.0540 [hep-ph].
- [78] **ALICE** Collaboration, S. Acharya *et al.*, “ $K^*(892)^0$ and $\phi(1020)$ production at midrapidity in pp collisions at $\sqrt{s} = 8$ TeV”, arXiv:1910.14410 [nucl-ex].
- [79] **STAR** Collaboration, B. I. Abelev *et al.*, “Systematic Measurements of Identified Particle Spectra in $pp, d^+ \text{Au}$ and Au+Au Collisions from STAR”, *Phys. Rev.* **C79** (2009) 034909, arXiv:0808.2041 [nucl-ex].
- [80] D. d’Enterria and T. Pierog, “Global properties of proton-proton collisions at $\sqrt{s} = 100$ TeV”, *JHEP* **08** (2016) 170, arXiv:1604.08536 [hep-ph].
- [81] **CMS** Collaboration, A. M. Sirunyan *et al.*, “Measurement of charged pion, kaon, and proton production in proton-proton collisions at $\sqrt{s} = 13$ TeV”, *Phys. Rev. D* **96** (Dec, 2017) 112003. <https://link.aps.org/doi/10.1103/PhysRevD.96.112003>.
- [82] **STAR** Collaboration, J. Adams *et al.*, “phi meson production in Au + Au and p+p collisions at $s(\text{NN})^{**}(1/2) = 200\text{-GeV}$ ”, *Phys. Lett.* **B612** (2005) 181–189, arXiv:nucl-ex/0406003 [nucl-ex].
- [83] **STAR** Collaboration, J. Adams *et al.*, “Identified particle distributions in pp and Au+Au collisions at $s(\text{NN})^{**}(1/2) = 200$ GeV”, *Phys. Rev. Lett.* **92** (2004) 112301, arXiv:nucl-ex/0310004 [nucl-ex].
- [84] **PHENIX** Collaboration, A. Adare *et al.*, “Identified charged hadron production in $p + p$ collisions at $\sqrt{s} = 200$ and 62.4 GeV”, *Phys. Rev.* **C83** (2011) 064903, arXiv:1102.0753 [nucl-ex].

- [85] **ALICE** Collaboration, J. Adam *et al.*, “Enhanced production of multi-strange hadrons in high-multiplicity proton-proton collisions”, *Nature Phys.* **13** (2017) 535–539, arXiv:1606.07424 [nucl-ex].
- [86] **ALICE** Collaboration, J. Adam *et al.*, “Charged-particle multiplicities in proton-proton collisions at $\sqrt{s} = 0.9$ to 8 TeV”, *Eur. Phys. J.* **C77** no. 1, (2017) 33, arXiv:1509.07541 [nucl-ex].
- [87] A. Ortiz, “Mean p_T scaling with m/n_q at the LHC: Absence of (hydro) flow in small systems?”, *Nucl. Phys.* **A943** (2015) 9–17, arXiv:1506.00584 [hep-ph].
- [88] **ALICE** Collaboration, K. Aamodt *et al.*, “Charged-particle multiplicity measurement in proton-proton collisions at $\sqrt{s} = 7$ TeV with ALICE at LHC”, *Eur. Phys. J.* **C68** (2010) 345–354, arXiv:1004.3514 [hep-ex].
- [89] P. Z. Skands, “Tuning Monte Carlo Generators: The Perugia Tunes”, *Phys. Rev.* **D82** (2010) 074018, arXiv:1005.3457 [hep-ph].
- [90] P. Skands, S. Carrazza, and J. Rojo, “Tuning PYTHIA 8.1: the Monash 2013 Tune”, *Eur. Phys. J.* **C74** no. 8, (2014) 3024, arXiv:1404.5630 [hep-ph].
- [91] P. Z. Skands and D. Wicke, “Non-perturbative QCD effects and the top mass at the Tevatron”, *Eur. Phys. J.* **C52** (2007) 133–140, arXiv:hep-ph/0703081 [HEP-PH].
- [92] T. Sjöstrand, S. Ask, J. R. Christiansen, R. Corke, N. Desai, P. Ilten, S. Mrenna, S. Prestel, C. O. Rasmussen, and P. Z. Skands, “An Introduction to PYTHIA 8.2”, *Comput. Phys. Commun.* **191** (2015) 159–177, arXiv:1410.3012 [hep-ph].
- [93] G. A. Schuler and T. Sjöstrand, “Hadronic diffractive cross-sections and the rise of the total cross-section”, *Phys. Rev.* **D49** (1994) 2257–2267.
- [94] K. Werner, “Core-corona separation in ultra-relativistic heavy ion collisions”, *Phys. Rev. Lett.* **98** (2007) 152301, arXiv:0704.1270 [nucl-th].
- [95] P. Eden and G. Gustafson, “Baryon production in the string fragmentation picture”, *Z. Phys.* **C75** (1997) 41–49, arXiv:hep-ph/9606454 [hep-ph].
- [96] H.-L. Lai, M. Guzzi, J. Huston, Z. Li, P. M. Nadolsky, J. Pumplin, and C. P. Yuan, “New parton distributions for collider physics”, *Phys. Rev.* **D82** (2010) 074024, arXiv:1007.2241 [hep-ph].
- [97] D. de Florian, R. Sassot, and M. Stratmann, “Global analysis of fragmentation functions for pions and kaons and their uncertainties”, *Phys. Rev.* **D75** (2007) 114010, arXiv:hep-ph/0703242 [HEP-PH].
- [98] I. Helenius, K. J. Eskola, H. Honkanen, and C. A. Salgado, “Impact-Parameter Dependent Nuclear Parton Distribution Functions: EPS09s and EKS98s and Their Applications in Nuclear Hard Processes”, *JHEP* **07** (2012) 073, arXiv:1205.5359 [hep-ph].
- [99] **ALICE** Collaboration, B. Abelev *et al.*, “Energy Dependence of the Transverse Momentum Distributions of Charged Particles in pp Collisions Measured by ALICE”, *Eur. Phys. J.* **C73** no. 12, (2013) 2662, arXiv:1307.1093 [nucl-ex].
- [100] **ALICE** Collaboration, B. Abelev *et al.*, “Neutral pion and η meson production in proton-proton collisions at $\sqrt{s} = 0.9$ TeV and $\sqrt{s} = 7$ TeV”, *Phys. Lett.* **B717** (2012) 162–172, arXiv:1205.5724 [hep-ex].

A The ALICE Collaboration

S. Acharya¹⁴¹, D. Adamová⁹⁴, A. Adler⁷³, J. Adolfsson⁸⁰, M.M. Aggarwal⁹⁹, G. Aglieri Rinella³³, M. Agnello³⁰, N. Agrawal^{10,53}, Z. Ahammed¹⁴¹, S. Ahmad¹⁶, S.U. Ahn⁷⁵, A. Akindinov⁹¹, M. Al-Turany¹⁰⁶, S.N. Alam¹⁴¹, D.S.D. Albuquerque¹²², D. Aleksandrov⁸⁷, B. Alessandro⁵⁸, H.M. Alfanda⁶, R. Alfaro Molina⁷⁰, B. Ali¹⁶, Y. Ali¹⁴, A. Alici^{10,26,53}, A. Alkin², J. Alme²¹, T. Alt⁶⁷, L. Altenkamper²¹, I. Altsybeev¹¹², M.N. Anaam⁶, C. Andrei⁴⁷, D. Andreou³³, H.A. Andrews¹¹⁰, A. Andronic¹⁴⁴, M. Angeletti³³, V. Anguelov¹⁰³, C. Anson¹⁵, T. Antićic¹⁰⁷, F. Antinori⁵⁶, P. Antonioli⁵³, N. Apadula⁷⁹, L. Aphecetche¹¹⁴, H. Appelshäuser⁶⁷, S. Arcelli²⁶, R. Arnaldi⁵⁸, M. Arratia⁷⁹, I.C. Arsene²⁰, M. Arslanbekci¹⁰³, A. Augustinus³³, R. Averbeck¹⁰⁶, S. Aziz⁷⁷, M.D. Azmi¹⁶, A. Badalà⁵⁵, Y.W. Baek⁴⁰, S. Bagnasco⁵⁸, X. Bai¹⁰⁶, R. Bailhache⁶⁷, R. Bala¹⁰⁰, A. Balbino³⁰, A. Baldissari¹³⁷, M. Ball⁴², S. Balouza¹⁰⁴, D. Banerjee³, R. Barbera²⁷, L. Barioglio²⁵, G.G. Barnaföldi¹⁴⁵, L.S. Barnby⁹³, V. Barret¹³⁴, P. Bartalini⁶, K. Barth³³, E. Bartsch⁶⁷, F. Baruffaldi²⁸, N. Bastid¹³⁴, S. Basu¹⁴³, G. Batigne¹¹⁴, B. Batyunya⁷⁴, D. Bauri⁴⁸, J.L. Bazo Alba¹¹¹, I.G. Bearden⁸⁸, C. Beattie¹⁴⁶, C. Bedda⁶², N.K. Behera⁶⁰, I. Belikov¹³⁶, A.D.C. Bell Hechavarria¹⁴⁴, F. Bellini³³, R. Bellwied¹²⁵, V. Belyaev⁹², G. Bencedi¹⁴⁵, S. Beole²⁵, A. Bercuci⁴⁷, Y. Berdnikov⁹⁷, D. Berenyi¹⁴⁵, R.A. Bertens¹³⁰, D. Berzana⁵⁸, M.G. Besoiu⁶⁶, L. Betev³³, A. Bhasin¹⁰⁰, I.R. Bhat¹⁰⁰, M.A. Bhat³, H. Bhatt⁴⁸, B. Bhattacharjee⁴¹, A. Bianchi²⁵, L. Bianchi²⁵, N. Bianchi⁵¹, J. Bielčík³⁶, J. Bielčíková⁹⁴, A. Bilandžić^{104,117}, G. Biro¹⁴⁵, R. Biswas³, S. Biswas³, J.T. Blair¹¹⁹, D. Blau⁸⁷, C. Blume⁶⁷, G. Boca¹³⁹, F. Bock^{33,95}, A. Bogdanov⁹², S. Boi²³, L. Boldizsár¹⁴⁵, A. Bolozdynya⁹², M. Bombara³⁷, G. Bonomi¹⁴⁰, H. Borel¹³⁷, A. Borissov⁹², H. Bossi¹⁴⁶, E. Botta²⁵, L. Bratruš⁶⁷, P. Braun-Munzinger¹⁰⁶, M. Bregant¹²¹, M. Broz³⁶, E. Bruna⁵⁸, G.E. Bruno¹⁰⁵, M.D. Buckland¹²⁷, D. Budnikov¹⁰⁸, H. Buesching⁶⁷, S. Bufalino³⁰, O. Bugnon¹¹⁴, P. Buhler¹¹³, P. Buncic³³, Z. Buthelezi^{71,131}, J.B. Butt¹⁴, J.T. Buxton⁹⁶, S.A. Bysiak¹¹⁸, D. Caffarri⁸⁹, A. Caliva¹⁰⁶, E. Calvo Villar¹¹¹, R.S. Camacho⁴⁴, P. Camerini²⁴, A.A. Capon¹¹³, F. Carnesecchi^{10,26}, R. Caron¹³⁷, J. Castillo Castellanos¹³⁷, A.J. Castro¹³⁰, E.A.R. Casula⁵⁴, F. Catalano³⁰, C. Ceballos Sanchez⁵², P. Chakraborty⁴⁸, S. Chandra¹⁴¹, W. Chang⁶, S. Chapelain³³, M. Chartier¹²⁷, S. Chattopadhyay¹⁴¹, S. Chattopadhyay¹⁰⁹, A. Chauvin²³, C. Cheshkov¹³⁵, B. Cheynis¹³⁵, V. Chibante Barroso³³, D.D. Chinellato¹²², S. Cho⁶⁰, P. Chochula³³, T. Chowdhury¹³⁴, P. Christakoglou⁸⁹, C.H. Christensen⁸⁸, P. Christiansen⁸⁰, T. Chujo¹³³, C. Cicalo⁵⁴, L. Cifarelli^{10,26}, F. Cindolo⁵³, G. Clai^{53,i}, J. Cleymans¹²⁴, F. Colamaria⁵², D. Colella⁵², A. Collu⁷⁹, M. Colocci²⁶, M. Concas^{58,ii}, G. Conesa Balbastre⁷⁸, Z. Conesa del Valle⁷⁷, G. Contin^{24,59}, J.G. Contreras³⁶, T.M. Cormier⁹⁵, Y. Corrales Morales²⁵, P. Cortese³¹, M.R. Cosentino¹²³, F. Costa³³, S. Costanza¹³⁹, P. Crochet¹³⁴, E. Cuautle⁶⁸, P. Cui⁶, L. Cunqueiro⁹⁵, D. Dabrowski¹⁴², T. Dahms^{104,117}, A. Dainese⁵⁶, F.P.A. Damas^{114,137}, M.C. Danisch¹⁰³, A. Danu⁶⁶, D. Das¹⁰⁹, I. Das¹⁰⁹, P. Das⁸⁵, P. Das³, S. Das³, A. Dash⁸⁵, S. Dash⁴⁸, S. De⁸⁵, A. De Caro²⁹, G. de Cataldo⁵², J. de Cuveland³⁸, A. De Falco²³, D. De Gruttola¹⁰, N. De Marco⁵⁸, S. De Pasquale²⁹, S. Deb⁴⁹, H.F. Degenhardt¹²¹, K.R. Deja¹⁴², A. Deloff⁸⁴, S. Delsanto^{25,131}, W. Deng⁶, D. Devetak¹⁰⁶, P. Dhankher⁴⁸, D. Di Bari³², A. Di Mauro³³, R.A. Diaz⁸, T. Dietel¹²⁴, P. Dillenseger⁶⁷, Y. Ding⁶, R. Divià³³, D.U. Dixit¹⁹, Ø. Djupsland²¹, U. Dmitrieva⁶¹, A. Dobrin⁶⁶, B. Dönigus⁶⁷, O. Dordic²⁰, A.K. Dubey¹⁴¹, A. Dubla¹⁰⁶, S. Dudi⁹⁹, M. Dukhishyam⁸⁵, P. Dupieux¹³⁴, R.J. Ehlers^{95,146}, V.N. Eikeland²¹, D. Elia⁵², E. Epple¹⁴⁶, B. Erazmus¹¹⁴, F. Erhardt⁹⁸, A. Erokhin¹¹², M.R. Ersdal²¹, B. Espagnon⁷⁷, G. Eulisse³³, D. Evans¹¹⁰, S. Evdokimov⁹⁰, L. Fabbietti^{104,117}, M. Faggin²⁸, J. Faivre⁷⁸, F. Fan⁶, A. Fantoni⁵¹, M. Fasel⁹⁵, P. Fecchio³⁰, A. Feliciello⁵⁸, G. Feofilov¹¹², A. Fernández Téllez⁴⁴, A. Ferrero¹³⁷, A. Ferretti²⁵, A. Festanti³³, V.J.G. Feuillard¹⁰³, J. Figiel¹¹⁸, S. Filchagin¹⁰⁸, D. Finogeev⁶¹, F.M. Fionda²¹, G. Fiorenza⁵², F. Flor¹²⁵, S. Foertsch⁷¹, P. Foka¹⁰⁶, S. Fokin⁸⁷, E. Fragiocomo⁵⁹, U. Frankenfeld¹⁰⁶, U. Fuchs³³, C. Furget⁷⁸, A. Furs⁶¹, M. Fusco Girard²⁹, J.J. Gaardhøje⁸⁸, M. Gagliardi²⁵, A.M. Gago¹¹¹, A. Gal¹³⁶, C.D. Galvan¹²⁰, P. Ganotti⁸³, C. Garabatos¹⁰⁶, E. Garcia-Solis¹¹, K. Garg¹¹⁴, C. Gargiulo³³, A. Garibaldi⁸⁶, K. Garner¹⁴⁴, P. Gasik^{104,117}, E.F. Gauger¹¹⁹, M.B. Gay Ducati⁶⁹, M. Germain¹¹⁴, J. Ghosh¹⁰⁹, P. Ghosh¹⁴¹, S.K. Ghosh³, M. Giacalone²⁶, P. Gianotti⁵¹, P. Giubellino^{58,106}, P. Giubilato²⁸, P. Glässel¹⁰³, A. Gomez Ramirez⁷³, V. Gonzalez^{106,143}, L.H. González-Trueba⁷⁰, S. Gorbunov³⁸, L. Görlich¹¹⁸, A. Goswami⁴⁸, S. Gotovac³⁴, V. Grabski⁷⁰, L.K. Graczykowski¹⁴², K.L. Graham¹¹⁰, L. Greiner⁷⁹, A. Grelli⁶², C. Grigoras³³, V. Grigoriev⁹², A. Grigoryan¹, S. Grigoryan⁷⁴, O.S. Groettvik²¹, F. Grossa³⁰, J.F. Grosse-Oetringhaus³³, R. Grossi¹⁰⁶, R. Guernane⁷⁸, M. Guittiere¹¹⁴, K. Gulbrandsen⁸⁸, T. Gunji¹³², A. Gupta¹⁰⁰, R. Gupta¹⁰⁰, I.B. Guzman⁴⁴, R. Haake¹⁴⁶, M.K. Habib¹⁰⁶, C. Hadjidakis⁷⁷, H. Hamagaki⁸¹, G. Hamar¹⁴⁵, M. Hamid⁶, R. Hannigan¹¹⁹, M.R. Haque^{62,85}, A. Harlenderova¹⁰⁶, J.W. Harris¹⁴⁶, A. Harton¹¹, J.A. Hasenbichler³³, H. Hassan⁹⁵, D. Hatzifotiadou^{10,53}, P. Hauer⁴², S. Hayashi¹³², S.T. Heckel^{67,104}, E. Hellbär⁶⁷, H. Helstrup³⁵, A. Herghelegiu⁴⁷, T. Herman³⁶, E.G. Hernandez⁴⁴, G. Herrera Corral⁹, F. Herrmann¹⁴⁴, K.F. Hetland³⁵, H. Hillemanns³³, C. Hills¹²⁷, B. Hippolyte¹³⁶, B. Hohlweber¹⁰⁴, J. Honermann¹⁴⁴, D. Horak³⁶, A. Hornung⁶⁷, S. Hornung¹⁰⁶, R. Hosokawa¹⁵, P. Hristov³³, C. Huang⁷⁷, C. Hughes¹³⁰, P. Huhn⁶⁷, T.J. Humanic⁹⁶,

H. Hushnud¹⁰⁹, L.A. Husova¹⁴⁴, N. Hussain⁴¹, S.A. Hussain¹⁴, D. Hutter³⁸, J.P. Iddon^{33,127}, R. Ilkaev¹⁰⁸, H. Ilyas¹⁴, M. Inaba¹³³, G.M. Innocenti³³, M. Ippolitov⁸⁷, A. Isakov⁹⁴, M.S. Islam¹⁰⁹, M. Ivanov¹⁰⁶, V. Ivanov⁹⁷, V. Izucheev⁹⁰, B. Jacak⁷⁹, N. Jacazio³³, P.M. Jacobs⁷⁹, S. Jadlovska¹¹⁶, J. Jadlovsky¹¹⁶, S. Jaelani⁶², C. Jahnke¹²¹, M.J. Jakubowska¹⁴², M.A. Janik¹⁴², T. Janson⁷³, M. Jercic⁹⁸, O. Jevons¹¹⁰, M. Jin¹²⁵, F. Jonas^{95,144}, P.G. Jones¹¹⁰, J. Jung⁶⁷, M. Jung⁶⁷, A. Jusko¹¹⁰, P. Kalinak⁶³, A. Kalweit³³, V. Kaplin⁹², S. Kar⁶, A. Karasu Uysal⁷⁶, O. Karavichev⁶¹, T. Karavicheva⁶¹, P. Karczmarczyk³³, E. Karpechev⁶¹, U. Kebschull⁷³, R. Keidel⁴⁶, M. Keil³³, B. Ketzer⁴², Z. Khabanova⁸⁹, A.M. Khan⁶, S. Khan¹⁶, S.A. Khan¹⁴¹, A. Khanzadeev⁹⁷, Y. Kharlov⁹⁰, A. Khatun¹⁶, A. Khuntia¹¹⁸, B. Kileng³⁵, B. Kim⁶⁰, B. Kim¹³³, D. Kim¹⁴⁷, D.J. Kim¹²⁶, E.J. Kim⁷², H. Kim^{17,147}, J. Kim¹⁴⁷, J.S. Kim⁴⁰, J. Kim¹⁰³, J. Kim¹⁴⁷, J. Kim⁷², M. Kim¹⁰³, S. Kim¹⁸, T. Kim¹⁴⁷, T. Kim¹⁴⁷, S. Kirsch⁶⁷, I. Kisel³⁸, S. Kiselev⁹¹, A. Kisiel¹⁴², J.L. Klay⁵, C. Klein⁶⁷, J. Klein^{33,58}, S. Klein⁷⁹, C. Klein-Bösing¹⁴⁴, M. Kleiner⁶⁷, A. Kluge³³, M.L. Knichel³³, A.G. Knospe¹²⁵, C. Kobdaj¹¹⁵, M.K. Köhler¹⁰³, T. Kollegger¹⁰⁶, A. Kondratyev⁷⁴, N. Kondratyeva⁹², E. Kondratyuk⁹⁰, J. Konig⁶⁷, P.J. Konopka³³, L. Koska¹¹⁶, O. Kovalenko⁸⁴, V. Kovalenko¹¹², M. Kowalski¹¹⁸, I. Králík⁶³, A. Kravčáková³⁷, L. Kreis¹⁰⁶, M. Krivda^{63,110}, F. Krizek⁹⁴, K. Krizkova Gajdosova³⁶, M. Krüger⁶⁷, E. Kryshen⁹⁷, M. Krzewicki³⁸, A.M. Kubera⁹⁶, V. Kučera^{33,60}, C. Kuhn¹³⁶, P.G. Kuijjer⁸⁹, L. Kumar⁹⁹, S. Kundu⁸⁵, P. Kurashvili⁸⁴, A. Kurepin⁶¹, A.B. Kurepin⁶¹, A. Kuryakin¹⁰⁸, S. Kushpil⁹⁴, J. Kvapil¹¹⁰, M.J. Kweon⁶⁰, J.Y. Kwon⁶⁰, Y. Kwon¹⁴⁷, S.L. La Pointe³⁸, P. La Rocca²⁷, Y.S. La⁷⁹, R. Langoy¹²⁹, K. Lapidus³³, A. Lardeux²⁰, P. Larionov⁵¹, E. Laudi³³, R. Lavicka³⁶, T. Lazareva¹¹², R. Lea²⁴, L. Leardini¹⁰³, J. Lee¹³³, S. Lee¹⁴⁷, F. Lehas⁸⁹, S. Lehner¹¹³, J. Lehrbach³⁸, R.C. Lemmon⁹³, I. León Monzón¹²⁰, E.D. Lesser¹⁹, M. Lettrich³³, P. Lévai¹⁴⁵, X. Li¹², X.L. Li⁶, J. Lien¹²⁹, R. Lietava¹¹⁰, B. Lim¹⁷, V. Lindenstruth³⁸, A. Lindner⁴⁷, S.W. Lindsay¹²⁷, C. Lippmann¹⁰⁶, M.A. Lisa⁹⁶, A. Liu¹⁹, J. Liu¹²⁷, S. Liu⁹⁶, W.J. Llope¹⁴³, I.M. Lofnæs²¹, V. Loginov⁹², C. Loizides⁹⁵, P. Loncar³⁴, J.A. Lopez¹⁰³, X. Lopez¹³⁴, E. López Torres⁸, J.R. Luhder¹⁴⁴, M. Lunardon²⁸, G. Luparello⁵⁹, Y.G. Ma³⁹, A. Maevskaia⁶¹, M. Mager³³, S.M. Mahmood²⁰, T. Mahmoud⁴², A. Maire¹³⁶, R.D. Majka¹⁴⁶, M. Malaev⁹⁷, Q.W. Malik²⁰, L. Malinina^{74,iii}, D. Mal'Kevich⁹¹, P. Malzacher¹⁰⁶, G. Mandaglio⁵⁵, V. Manko⁸⁷, F. Manso¹³⁴, V. Manzari⁵², Y. Mao⁶, M. Marchisone¹³⁵, J. Mareš⁶⁵, G.V. Margagliotti²⁴, A. Margotti⁵³, J. Margutti⁶², A. Marín¹⁰⁶, C. Markert¹¹⁹, M. Marquard⁶⁷, C.D. Martin²⁴, N.A. Martin¹⁰³, P. Martinengo³³, J.L. Martinez¹²⁵, M.I. Martínez⁴⁴, G. Martínez García¹¹⁴, S. Masciocchi¹⁰⁶, M. Masera²⁵, A. Masoni⁵⁴, L. Massacrier⁷⁷, E. Masson¹¹⁴, A. Mastroserio^{52,138}, A.M. Mathis^{104,117}, O. Matonoha⁸⁰, P.F.T. Matuoka¹²¹, A. Matyja¹¹⁸, C. Mayer¹¹⁸, F. Mazzaschi²⁵, M. Mazzilli⁵², M.A. Mazzoni⁵⁷, A.F. Mechler⁶⁷, F. Meddi²², Y. Melikyan^{61,92}, A. Menchaca-Rocha⁷⁰, C. Mengke⁶, E. Meninno^{29,113}, M. Meres¹³, S. Mhlanga¹²⁴, Y. Miake¹³³, L. Micheletti²⁵, D.L. Mihaylov¹⁰⁴, K. Mikhaylov^{74,91}, A.N. Mishra⁶⁸, D. Miśkowiec¹⁰⁶, A. Modak³, N. Mohammadi³³, A.P. Mohanty⁶², B. Mohanty⁸⁵, M. Mohisin Khan^{16,iv}, Z. Moravcová⁸⁸, C. Mordasini¹⁰⁴, D.A. Moreira De Godoy¹⁴⁴, L.A.P. Moreno⁴⁴, I. Morozov⁶¹, A. Morsch³³, T. Mrnjavac³³, V. Muccifora⁵¹, E. Mudnic³⁴, D. Mühlheim¹⁴⁴, S. Muhuri¹⁴¹, J.D. Mulligan⁷⁹, M.G. Munhoz¹²¹, R.H. Munzer⁶⁷, H. Murakami¹³², S. Murray¹²⁴, L. Musa³³, J. Musinsky⁶³, C.J. Myers¹²⁵, J.W. Myrcha¹⁴², B. Naik⁴⁸, R. Nair⁸⁴, B.K. Nandi⁴⁸, R. Nania^{10,53}, E. Nappi⁵², M.U. Naru¹⁴, A.F. Nassirpour⁸⁰, C. Nattrass¹³⁰, R. Nayak⁴⁸, T.K. Nayak⁸⁵, S. Nazarenko¹⁰⁸, A. Neagu²⁰, R.A. Negrao De Oliveira⁶⁷, L. Nellen⁶⁸, S.V. Nesbo³⁵, G. Neskovic³⁸, D. Nesterov¹¹², L.T. Neumann¹⁴², B.S. Nielsen⁸⁸, S. Nikolaev⁸⁷, S. Nikulin⁸⁷, V. Nikulin⁹⁷, F. Noferini^{10,53}, P. Nomokonov⁷⁴, J. Norman^{78,127}, N. Novitzky¹³³, P. Nowakowski¹⁴², A. Nyanin⁸⁷, J. Nystrand²¹, M. Ogino⁸¹, A. Ohlson^{80,103}, J. Oleniacz¹⁴², A.C. Oliveira Da Silva¹³⁰, M.H. Oliver¹⁴⁶, C. Oppedisano⁵⁸, A. Ortiz Velasquez⁶⁸, A. Oskarsson⁸⁰, J. Otwinowski¹¹⁸, K. Oyama⁸¹, Y. Pachmayer¹⁰³, V. Pacik⁸⁸, D. Pagano¹⁴⁰, G. Paić⁶⁸, J. Pan¹⁴³, S. Panebianco¹³⁷, P. Pareek^{49,141}, J. Park⁶⁰, J.E. Parkkila¹²⁶, S. Parmar⁹⁹, S.P. Pathak¹²⁵, B. Paul²³, H. Pei⁶, T. Peitzmann⁶², X. Peng⁶, L.G. Pereira⁶⁹, H. Pereira Da Costa¹³⁷, D. Peresunko⁸⁷, G.M. Perez⁸, Y. Pestov⁴, V. Petráček³⁶, M. Petrovici⁴⁷, R.P. Pezzi⁶⁹, S. Piano⁵⁹, M. Pikna¹³, P. Pillot¹¹⁴, O. Pinazza^{33,53}, L. Pinsky¹²⁵, C. Pinto²⁷, S. Pisano^{10,51}, D. Pistone⁵⁵, M. Płoskon⁷⁹, M. Planinic⁹⁸, F. Pliquet⁶⁷, M.G. Poghosyan⁹⁵, B. Polichtchouk⁹⁰, N. Poljak⁹⁸, A. Pop⁴⁷, S. Porteboeuf-Houssais¹³⁴, V. Pozdniakov⁷⁴, S.K. Prasad³, R. Preghenella⁵³, F. Prino⁵⁸, C.A. Pruneau¹⁴³, I. Pshenichnov⁶¹, M. Puccio³³, J. Putschke¹⁴³, L. Quaglia²⁵, R.E. Quishpe¹²⁵, S. Ragoni¹¹⁰, S. Raha³, S. Rajput¹⁰⁰, J. Rak¹²⁶, A. Rakotozafindrabe¹³⁷, L. Ramello³¹, F. Rami¹³⁶, S.A.R. Ramirez⁴⁴, R. Raniwala¹⁰¹, S. Raniwala¹⁰¹, S.S. Räsänen⁴³, R. Rath⁴⁹, V. Ratza⁴², I. Ravasenga⁸⁹, K.F. Read^{95,130}, A.R. Redelbach³⁸, K. Redlich^{84,v}, A. Rehman²¹, P. Reichelt⁶⁷, F. Reidt³³, X. Ren⁶, R. Renfordt⁶⁷, Z. Rescakova³⁷, K. Reygers¹⁰³, V. Riabov⁹⁷, T. Richert^{80,88}, M. Richter²⁰, P. Riedler³³, W. Riegler³³, F. Rigg²⁷, C. Ristea⁶⁶, S.P. Rode⁴⁹, M. Rodríguez Cahuantzi⁴⁴, K. Røed²⁰, R. Rogalev⁹⁰, E. Rogochaya⁷⁴, D. Rohr³³, D. Röhrich²¹, P.S. Rokita¹⁴², F. Ronchetti⁵¹, A. Rosano⁵⁵, E.D. Rosas⁶⁸, K. Roslon¹⁴², A. Rossi^{28,56}, A. Rotondi¹³⁹, A. Roy⁴⁹, P. Roy¹⁰⁹, O.V. Rueda⁸⁰, R. Rui²⁴, B. Rumyantsev⁷⁴, A. Rustamov⁸⁶, E. Ryabinkin⁸⁷, Y. Ryabov⁹⁷,

A. Rybicki¹¹⁸, H. Rytkonen¹²⁶, O.A.M. Saarimaki⁴³, S. Sadhu¹⁴¹, S. Sadovsky⁹⁰, K. Šafařík³⁶, S.K. Saha¹⁴¹, B. Sahoo⁴⁸, P. Sahoo⁴⁸, R. Sahoo⁴⁹, S. Sahoo⁶⁴, P.K. Sahu⁶⁴, J. Saini¹⁴¹, S. Sakai¹³³, S. Sambyal¹⁰⁰, V. Samsonov^{92, 97}, D. Sarkar¹⁴³, N. Sarkar¹⁴¹, P. Sarma⁴¹, V.M. Sarti¹⁰⁴, M.H.P. Sas⁶², E. Scapparone⁵³, J. Schambach¹¹⁹, H.S. Scheid⁶⁷, C. Schiaua⁴⁷, R. Schicker¹⁰³, A. Schmah¹⁰³, C. Schmidt¹⁰⁶, H.R. Schmidt¹⁰², M.O. Schmidt¹⁰³, M. Schmidt¹⁰², N.V. Schmidt^{67, 95}, A.R. Schmier¹³⁰, J. Schukraft⁸⁸, Y. Schutz^{33, 136}, K. Schwarz¹⁰⁶, K. Schweda¹⁰⁶, G. Scioli²⁶, E. Scomparin⁵⁸, M. Šefčík³⁷, J.E. Seger¹⁵, Y. Sekiguchi¹³², D. Sekihata¹³², I. Selyuzhenkov^{92, 106}, S. Senyukov¹³⁶, D. Serebryakov⁶¹, A. Sevcenco⁶⁶, A. Shabanov⁶¹, A. Shabetai¹¹⁴, R. Shahoyan³³, W. Shaikh¹⁰⁹, A. Shangaraev⁹⁰, A. Sharma⁹⁹, A. Sharma¹⁰⁰, H. Sharma¹¹⁸, M. Sharma¹⁰⁰, N. Sharma⁹⁹, S. Sharma¹⁰⁰, A.I. Sheikh¹⁴¹, K. Shigaki⁴⁵, M. Shimomura⁸², S. Shirinkin⁹¹, Q. Shou³⁹, Y. Sibiriak⁸⁷, S. Siddhanta⁵⁴, T. Siemiaczuk⁸⁴, D. Silvermyr⁸⁰, G. Simatovic⁸⁹, G. Simonetti³³, B. Singh¹⁰⁴, R. Singh⁸⁵, R. Singh¹⁰⁰, R. Singh⁴⁹, V.K. Singh¹⁴¹, V. Singhal¹⁴¹, T. Sinha¹⁰⁹, B. Sitar¹³, M. Sitta³¹, T.B. Skaali²⁰, M. Slupecki¹²⁶, N. Smirnov¹⁴⁶, R.J.M. Snellings⁶², C. Soncco¹¹¹, J. Song¹²⁵, A. Songmoolnak¹¹⁵, F. Soramel²⁸, S. Sorensen¹³⁰, I. Sputowska¹¹⁸, J. Stachel¹⁰³, I. Stan⁶⁶, P. Stankus⁹⁵, P.J. Steffanic¹³⁰, E. Stenlund⁸⁰, D. Stocco¹¹⁴, M.M. Storetvedt³⁵, L.D. Stritto²⁹, A.A.P. Suaide¹²¹, T. Sugitate⁴⁵, C. Suire⁷⁷, M. Suleymanov¹⁴, M. Suljic³³, R. Sultanov⁹¹, M. Šumbera⁹⁴, V. Sumberia¹⁰⁰, S. Sumowidagdo⁵⁰, S. Swain⁶⁴, A. Szabo¹³, I. Szarka¹³, U. Tabassam¹⁴, S.F. Taghavi¹⁰⁴, G. Taillepied¹³⁴, J. Takahashi¹²², G.J. Tambave²¹, S. Tang^{6, 134}, M. Tarhini¹¹⁴, M.G. Tarzila⁴⁷, A. Tauro³³, G. Tejeda Muñoz⁴⁴, A. Telesca³³, L. Terlizzi²⁵, C. Terrevoli¹²⁵, D. Thakur⁴⁹, S. Thakur¹⁴¹, D. Thomas¹¹⁹, F. Thoresen⁸⁸, R. Tieulent¹³⁵, A. Tikhonov⁶¹, A.R. Timmins¹²⁵, A. Toia⁶⁷, N. Topilskaya⁶¹, M. Toppi⁵¹, F. Torales-Acosta¹⁹, S.R. Torres^{36, 120}, A. Trifiro⁵⁵, S. Tripathy^{49, 68}, T. Tripathy⁴⁸, S. Trogolo²⁸, G. Trombetta³², L. Tropp³⁷, V. Trubnikov², W.H. Trzaska¹²⁶, T.P. Trzciński¹⁴², B.A. Trzeciak^{36, 62}, T. Tsuji¹³², A. Tumkin¹⁰⁸, R. Turrisi⁵⁶, T.S. Tveter²⁰, K. Ullaland²¹, E.N. Umaka¹²⁵, A. Uras¹³⁵, G.L. Usai²³, M. Vala³⁷, N. Valle¹³⁹, S. Vallero⁵⁸, N. van der Kolk⁶², L.V.R. van Doremalen⁶², M. van Leeuwen⁶², P. Vande Vyvre³³, D. Varga¹⁴⁵, Z. Varga¹⁴⁵, M. Varga-Kofarago¹⁴⁵, A. Vargas⁴⁴, M. Vasileiou⁸³, A. Vasiliev⁸⁷, O. Vázquez Doce^{104, 117}, V. Vechernin¹¹², E. Vercellin²⁵, S. Vergara Limón⁴⁴, L. Vermunt⁶², R. Vernet⁷, R. Vértesi¹⁴⁵, L. Vickovic³⁴, Z. Vilakazi¹³¹, O. Villalobos Baillie¹¹⁰, G. Vino⁵², A. Vinogradov⁸⁷, T. Virgili²⁹, V. Vislavicius⁸⁸, A. Vodopyanov⁷⁴, B. Volkel³³, M.A. Völkl¹⁰², K. Voloshin⁹¹, S.A. Voloshin¹⁴³, G. Volpe³², B. von Haller³³, I. Vorobyev¹⁰⁴, D. Voscek¹¹⁶, J. Vrláková³⁷, B. Wagner²¹, M. Weber¹¹³, A. Wegrzynek³³, S.C. Wenzel³³, J.P. Wessels¹⁴⁴, J. Wiechula⁶⁷, J. Wikne²⁰, G. Wilk⁸⁴, J. Wilkinson^{10, 53}, G.A. Willems¹⁴⁴, E. Willsher¹¹⁰, B. Windelband¹⁰³, M. Winn¹³⁷, W.E. Witt¹³⁰, Y. Wu¹²⁸, R. Xu⁶, S. Yalcin⁷⁶, Y. Yamaguchi⁴⁵, K. Yamakawa⁴⁵, S. Yang²¹, S. Yano¹³⁷, Z. Yin⁶, H. Yokoyama⁶², I.-K. Yoo¹⁷, J.H. Yoon⁶⁰, S. Yuan²¹, A. Yuncu¹⁰³, V. Yurchenko², V. Zaccolo²⁴, A. Zaman¹⁴, C. Zampolli³³, H.J.C. Zanolli⁶², N. Zardoshti³³, A. Zarochentsev¹¹², P. Závada⁶⁵, N. Zaviyalov¹⁰⁸, H. Zbroszczyk¹⁴², M. Zhalov⁹⁷, S. Zhang³⁹, X. Zhang⁶, Z. Zhang⁶, V. Zhrebchevskii¹¹², D. Zhou⁶, Y. Zhou⁸⁸, Z. Zhou²¹, J. Zhu^{6, 106}, Y. Zhu⁶, A. Zichichi^{10, 26}, G. Zinovjev², N. Zurlo¹⁴⁰,

Affiliation notes

ⁱ Italian National Agency for New Technologies, Energy and Sustainable Economic Development (ENEA), Bologna, Italy

ⁱⁱ Dipartimento DET del Politecnico di Torino, Turin, Italy

ⁱⁱⁱ M.V. Lomonosov Moscow State University, D.V. Skobeltsyn Institute of Nuclear, Physics, Moscow, Russia

^{iv} Department of Applied Physics, Aligarh Muslim University, Aligarh, India

^v Institute of Theoretical Physics, University of Wroclaw, Poland

Collaboration Institutes

¹ A.I. Alikhanyan National Science Laboratory (Yerevan Physics Institute) Foundation, Yerevan, Armenia

² Bogolyubov Institute for Theoretical Physics, National Academy of Sciences of Ukraine, Kiev, Ukraine

³ Bose Institute, Department of Physics and Centre for Astroparticle Physics and Space Science (CAPSS), Kolkata, India

⁴ Budker Institute for Nuclear Physics, Novosibirsk, Russia

⁵ California Polytechnic State University, San Luis Obispo, California, United States

⁶ Central China Normal University, Wuhan, China

⁷ Centre de Calcul de l'IN2P3, Villeurbanne, Lyon, France

⁸ Centro de Aplicaciones Tecnológicas y Desarrollo Nuclear (CEADEN), Havana, Cuba

⁹ Centro de Investigación y de Estudios Avanzados (CINVESTAV), Mexico City and Mérida, Mexico

¹⁰ Centro Fermi - Museo Storico della Fisica e Centro Studi e Ricerche "Enrico Fermi", Rome, Italy

- ¹¹ Chicago State University, Chicago, Illinois, United States
¹² China Institute of Atomic Energy, Beijing, China
¹³ Comenius University Bratislava, Faculty of Mathematics, Physics and Informatics, Bratislava, Slovakia
¹⁴ COMSATS University Islamabad, Islamabad, Pakistan
¹⁵ Creighton University, Omaha, Nebraska, United States
¹⁶ Department of Physics, Aligarh Muslim University, Aligarh, India
¹⁷ Department of Physics, Pusan National University, Pusan, Republic of Korea
¹⁸ Department of Physics, Sejong University, Seoul, Republic of Korea
¹⁹ Department of Physics, University of California, Berkeley, California, United States
²⁰ Department of Physics, University of Oslo, Oslo, Norway
²¹ Department of Physics and Technology, University of Bergen, Bergen, Norway
²² Dipartimento di Fisica dell'Università 'La Sapienza' and Sezione INFN, Rome, Italy
²³ Dipartimento di Fisica dell'Università and Sezione INFN, Cagliari, Italy
²⁴ Dipartimento di Fisica dell'Università and Sezione INFN, Trieste, Italy
²⁵ Dipartimento di Fisica dell'Università and Sezione INFN, Turin, Italy
²⁶ Dipartimento di Fisica e Astronomia dell'Università and Sezione INFN, Bologna, Italy
²⁷ Dipartimento di Fisica e Astronomia dell'Università and Sezione INFN, Catania, Italy
²⁸ Dipartimento di Fisica e Astronomia dell'Università and Sezione INFN, Padova, Italy
²⁹ Dipartimento di Fisica 'E.R. Caianiello' dell'Università and Gruppo Collegato INFN, Salerno, Italy
³⁰ Dipartimento DISAT del Politecnico and Sezione INFN, Turin, Italy
³¹ Dipartimento di Scienze e Innovazione Tecnologica dell'Università del Piemonte Orientale and INFN Sezione di Torino, Alessandria, Italy
³² Dipartimento Interateneo di Fisica 'M. Merlin' and Sezione INFN, Bari, Italy
³³ European Organization for Nuclear Research (CERN), Geneva, Switzerland
³⁴ Faculty of Electrical Engineering, Mechanical Engineering and Naval Architecture, University of Split, Split, Croatia
³⁵ Faculty of Engineering and Science, Western Norway University of Applied Sciences, Bergen, Norway
³⁶ Faculty of Nuclear Sciences and Physical Engineering, Czech Technical University in Prague, Prague, Czech Republic
³⁷ Faculty of Science, P.J. Šafárik University, Košice, Slovakia
³⁸ Frankfurt Institute for Advanced Studies, Johann Wolfgang Goethe-Universität Frankfurt, Frankfurt, Germany
³⁹ Fudan University, Shanghai, China
⁴⁰ Gangneung-Wonju National University, Gangneung, Republic of Korea
⁴¹ Gauhati University, Department of Physics, Guwahati, India
⁴² Helmholtz-Institut für Strahlen- und Kernphysik, Rheinische Friedrich-Wilhelms-Universität Bonn, Bonn, Germany
⁴³ Helsinki Institute of Physics (HIP), Helsinki, Finland
⁴⁴ High Energy Physics Group, Universidad Autónoma de Puebla, Puebla, Mexico
⁴⁵ Hiroshima University, Hiroshima, Japan
⁴⁶ Hochschule Worms, Zentrum für Technologietransfer und Telekommunikation (ZTT), Worms, Germany
⁴⁷ Horia Hulubei National Institute of Physics and Nuclear Engineering, Bucharest, Romania
⁴⁸ Indian Institute of Technology Bombay (IIT), Mumbai, India
⁴⁹ Indian Institute of Technology Indore, Indore, India
⁵⁰ Indonesian Institute of Sciences, Jakarta, Indonesia
⁵¹ INFN, Laboratori Nazionali di Frascati, Frascati, Italy
⁵² INFN, Sezione di Bari, Bari, Italy
⁵³ INFN, Sezione di Bologna, Bologna, Italy
⁵⁴ INFN, Sezione di Cagliari, Cagliari, Italy
⁵⁵ INFN, Sezione di Catania, Catania, Italy
⁵⁶ INFN, Sezione di Padova, Padova, Italy
⁵⁷ INFN, Sezione di Roma, Rome, Italy
⁵⁸ INFN, Sezione di Torino, Turin, Italy
⁵⁹ INFN, Sezione di Trieste, Trieste, Italy
⁶⁰ Inha University, Incheon, Republic of Korea
⁶¹ Institute for Nuclear Research, Academy of Sciences, Moscow, Russia

- ⁶² Institute for Subatomic Physics, Utrecht University/Nikhef, Utrecht, Netherlands
⁶³ Institute of Experimental Physics, Slovak Academy of Sciences, Košice, Slovakia
⁶⁴ Institute of Physics, Homi Bhabha National Institute, Bhubaneswar, India
⁶⁵ Institute of Physics of the Czech Academy of Sciences, Prague, Czech Republic
⁶⁶ Institute of Space Science (ISS), Bucharest, Romania
⁶⁷ Institut für Kernphysik, Johann Wolfgang Goethe-Universität Frankfurt, Frankfurt, Germany
⁶⁸ Instituto de Ciencias Nucleares, Universidad Nacional Autónoma de México, Mexico City, Mexico
⁶⁹ Instituto de Física, Universidade Federal do Rio Grande do Sul (UFRGS), Porto Alegre, Brazil
⁷⁰ Instituto de Física, Universidad Nacional Autónoma de México, Mexico City, Mexico
⁷¹ iThemba LABS, National Research Foundation, Somerset West, South Africa
⁷² Jeonbuk National University, Jeonju, Republic of Korea
⁷³ Johann-Wolfgang-Goethe Universität Frankfurt Institut für Informatik, Fachbereich Informatik und Mathematik, Frankfurt, Germany
⁷⁴ Joint Institute for Nuclear Research (JINR), Dubna, Russia
⁷⁵ Korea Institute of Science and Technology Information, Daejeon, Republic of Korea
⁷⁶ KTO Karatay University, Konya, Turkey
⁷⁷ Laboratoire de Physique des 2 Infinis, Irène Joliot-Curie, Orsay, France
⁷⁸ Laboratoire de Physique Subatomique et de Cosmologie, Université Grenoble-Alpes, CNRS-IN2P3, Grenoble, France
⁷⁹ Lawrence Berkeley National Laboratory, Berkeley, California, United States
⁸⁰ Lund University Department of Physics, Division of Particle Physics, Lund, Sweden
⁸¹ Nagasaki Institute of Applied Science, Nagasaki, Japan
⁸² Nara Women's University (NWU), Nara, Japan
⁸³ National and Kapodistrian University of Athens, School of Science, Department of Physics , Athens, Greece
⁸⁴ National Centre for Nuclear Research, Warsaw, Poland
⁸⁵ National Institute of Science Education and Research, Homi Bhabha National Institute, Jatni, India
⁸⁶ National Nuclear Research Center, Baku, Azerbaijan
⁸⁷ National Research Centre Kurchatov Institute, Moscow, Russia
⁸⁸ Niels Bohr Institute, University of Copenhagen, Copenhagen, Denmark
⁸⁹ Nikhef, National institute for subatomic physics, Amsterdam, Netherlands
⁹⁰ NRC Kurchatov Institute IHEP, Protvino, Russia
⁹¹ NRC «Kurchatov» Institute - ITEP, Moscow, Russia
⁹² NRNU Moscow Engineering Physics Institute, Moscow, Russia
⁹³ Nuclear Physics Group, STFC Daresbury Laboratory, Daresbury, United Kingdom
⁹⁴ Nuclear Physics Institute of the Czech Academy of Sciences, Řež u Prahy, Czech Republic
⁹⁵ Oak Ridge National Laboratory, Oak Ridge, Tennessee, United States
⁹⁶ Ohio State University, Columbus, Ohio, United States
⁹⁷ Petersburg Nuclear Physics Institute, Gatchina, Russia
⁹⁸ Physics department, Faculty of science, University of Zagreb, Zagreb, Croatia
⁹⁹ Physics Department, Panjab University, Chandigarh, India
¹⁰⁰ Physics Department, University of Jammu, Jammu, India
¹⁰¹ Physics Department, University of Rajasthan, Jaipur, India
¹⁰² Physikalisches Institut, Eberhard-Karls-Universität Tübingen, Tübingen, Germany
¹⁰³ Physikalisches Institut, Ruprecht-Karls-Universität Heidelberg, Heidelberg, Germany
¹⁰⁴ Physik Department, Technische Universität München, Munich, Germany
¹⁰⁵ Politecnico di Bari, Bari, Italy
¹⁰⁶ Research Division and ExtreMe Matter Institute EMMI, GSI Helmholtzzentrum für Schwerionenforschung GmbH, Darmstadt, Germany
¹⁰⁷ Rudjer Bošković Institute, Zagreb, Croatia
¹⁰⁸ Russian Federal Nuclear Center (VNIEF), Sarov, Russia
¹⁰⁹ Saha Institute of Nuclear Physics, Homi Bhabha National Institute, Kolkata, India
¹¹⁰ School of Physics and Astronomy, University of Birmingham, Birmingham, United Kingdom
¹¹¹ Sección Física, Departamento de Ciencias, Pontificia Universidad Católica del Perú, Lima, Peru
¹¹² St. Petersburg State University, St. Petersburg, Russia
¹¹³ Stefan Meyer Institut für Subatomare Physik (SMI), Vienna, Austria

- ¹¹⁴ SUBATECH, IMT Atlantique, Université de Nantes, CNRS-IN2P3, Nantes, France
¹¹⁵ Suranaree University of Technology, Nakhon Ratchasima, Thailand
¹¹⁶ Technical University of Košice, Košice, Slovakia
¹¹⁷ Technische Universität München, Excellence Cluster 'Universe', Munich, Germany
¹¹⁸ The Henryk Niewodniczanski Institute of Nuclear Physics, Polish Academy of Sciences, Cracow, Poland
¹¹⁹ The University of Texas at Austin, Austin, Texas, United States
¹²⁰ Universidad Autónoma de Sinaloa, Culiacán, Mexico
¹²¹ Universidade de São Paulo (USP), São Paulo, Brazil
¹²² Universidade Estadual de Campinas (UNICAMP), Campinas, Brazil
¹²³ Universidade Federal do ABC, Santo Andre, Brazil
¹²⁴ University of Cape Town, Cape Town, South Africa
¹²⁵ University of Houston, Houston, Texas, United States
¹²⁶ University of Jyväskylä, Jyväskylä, Finland
¹²⁷ University of Liverpool, Liverpool, United Kingdom
¹²⁸ University of Science and Technology of China, Hefei, China
¹²⁹ University of South-Eastern Norway, Tønsberg, Norway
¹³⁰ University of Tennessee, Knoxville, Tennessee, United States
¹³¹ University of the Witwatersrand, Johannesburg, South Africa
¹³² University of Tokyo, Tokyo, Japan
¹³³ University of Tsukuba, Tsukuba, Japan
¹³⁴ Université Clermont Auvergne, CNRS/IN2P3, LPC, Clermont-Ferrand, France
¹³⁵ Université de Lyon, Université Lyon 1, CNRS/IN2P3, IPN-Lyon, Villeurbanne, Lyon, France
¹³⁶ Université de Strasbourg, CNRS, IPHC UMR 7178, F-67000 Strasbourg, France, Strasbourg, France
¹³⁷ Université Paris-Saclay Centre d'Etudes de Saclay (CEA), IRFU, Département de Physique Nucléaire (DPhN), Saclay, France
¹³⁸ Università degli Studi di Foggia, Foggia, Italy
¹³⁹ Università degli Studi di Pavia, Pavia, Italy
¹⁴⁰ Università di Brescia, Brescia, Italy
¹⁴¹ Variable Energy Cyclotron Centre, Homi Bhabha National Institute, Kolkata, India
¹⁴² Warsaw University of Technology, Warsaw, Poland
¹⁴³ Wayne State University, Detroit, Michigan, United States
¹⁴⁴ Westfälische Wilhelms-Universität Münster, Institut für Kernphysik, Münster, Germany
¹⁴⁵ Wigner Research Centre for Physics, Budapest, Hungary
¹⁴⁶ Yale University, New Haven, Connecticut, United States
¹⁴⁷ Yonsei University, Seoul, Republic of Korea